Synthesis, Applications, and Optical Properties of Rare Earth Fluorides for Laser Refrigeration

Robert G. J. Felsted

A dissertation
submitted in partial fulfillment of the
requirements for the degree of

Doctor of Philosophy

University of Washington

2023

Reading Committee:

Peter J. Pauzauskie, Chair

David J. Masiello

Xiaosong Li

Program Authorized to Offer Degree:
Chemistry

University of Washington

Abstract

Synthesis, Applications, and Optical Properties of Rare Earth Fluorides for Laser Refrigeration

Robert G. J. Felsted

Chair of the Supervisory Committee:
Professor Peter J. Pauzauskie
Department of Materials Science and Engineering

One of the most powerful scientific tools available to studying natural phenomena is light. For spectroscopic analysis, Light has uses in nearly every branch of science, yet light has the often unintended side effect of causing photothermal heating. This heating will alter the system being measured, which can cause serious issues for sensitivity and accuracy of measurement readouts. It becomes necessary to offset this heating in many applications. While this can be done with traditional methods, mainly heat sinks, cryogenic fluids, and thermoelectric coolers, these also add constraints to the system by requiring cooling via conduction with a cooler medium. One solution is the use of laser refrigeration to remove the excess energy from the system via radiation through the emission of light. Chapter 1 focuses on understanding laser refrigeration, as well as understanding optical tweezers, which stand to gain much from the use of laser refrigeration.

This work focuses on understanding the current scientific body of knowledge surrounding rare earth fluoride microcrystals for laser refrigeration applications, including synthesis, characterization, and applications in complex experiments. These materials represent a non-contact method of cooling micro and nano scale materials through laser irradiation alone, including the cooling of payloads attached to the sur-

face of the crystals. In chapter 2, we discuss the synthesis of these materials. By controlling the synthesis, we can make microscale materials that cannot be grown in bulk with current methodologies. These novel crystals are predicted to have the highest possible cooling power of any material that can be reliably made. Not only can these materials be grown through these novel methods, but the morphology can be tuned easily to provide optical cavities with resonant properties, with respect to the cooling laser beam. By doing so, it becomes possible to make microcavity materials for optimized laser refrigeration through direct hydrothermal synthesis.

Understanding the synthesis of these materials is critical to successfully modeling and improving upon design. The nucleation of sodium yttrium fluoride, the main material of interest, was not well understood prior to these works. We study the nucleation and find it to be a multi-step crystallization mechanism that operates through spinodal decomposition of the principal reagents into ion-rich and ion-poor phases, causing the product to crash out as a gel. The gel then reacts with the water surrounding it to transform from an amorphous YF_3 phase to a crystalline NaYF phase by taking in sodium ions from the surrounding environment. This allows the gel to condense into nanocrystals of the stable, cubic alpha phase of NaYF.

When heated in aqueous conditions, the alpha phase can convert to the hexagonal beta phase of NaYF. This phase of NaYF has been predicted to be exceptionally good at laser refrigeration, but it cannot be grown in bulk at high temperatures due to fracturing of bulk crystals during the melt-growth process. The high temperatures needed for crystal melts are avoided by use of hydrothermal synthesis. While this cannot grow bulk sized crystals, we can reliably grow beta phase NaYF as nanowires. This was the only morphology shown to cool prior to my work. The crystals preferentially grow along the [0001] plane, leading the long, thin nanowires. By controlling the synthesis through ligands and relative ionic concentrations, the morphology can

be altered to produce hexagonal platelets up to 10 μm across while remaining less than 200 nm thick. The aspect ratio is tunable with relative reagent concentration, allowing for precise morphology control.

In addition to these crystals being morphologically controllable, they are capable of undergoing laser refrigeration. By doping with 10% Yb^{3+} during the synthesis, the crystals become capable of emitting higher energy light than they absorb with sufficient efficiency to create a net loss of energy in this system, resulting in cooling, which we explore in chapter 3. The crystals are placed onto cadmium sulfide nanoribbons for thermal isolation from a large substrate, and then they are irradiated with a 1020 nm laser to induce cooling. The luminescence is collected and used for ratiometric thermometry, where specific crystal field levels are integrated for comparing emission from the different crystal field levels. The ratio of the relative emission can be calibrated against temperature, confirming that the hexagonal platelet beta phase of NaYF is capable of cooling up to 12.5 K. Further cooling may be possible with synthetic and experimental refinement. Further experiments are done with nanodiamonds attached to the surface of rare earth fluorides to act as a payload. Since nanodiamonds do not cool under NIR light, we can use them as a thermometer to determine if the cooling power of the crystal is sufficient to overcome any photothermal heating of the nanodiamonds. Debye Waller factor thermometry and ODMR thermometry confirm the nanodiamonds to be cooling, with the diamonds on YLF crystals being cooled by more than 30 K and the diamonds on NaYF crystals confirmed to cool 12.5 K below room temperature. We also explore the possiblity of cooling diamond in chapter 3 through the conversion of NV^- centers into H3 centers, which can undergo anti-Stokes luminescence necessary for laser refrigeration. While the diamonds are not cooled below room temperature, we report progress in offsetting photothermal heating in NV-rich diamond samples.

While the process of laser refrigeration is novel on its own, it is enhanced by applying it to other optical systems. The system most poised to take advantage of laser refrigeration is optical tweezers. In chapter 4, we discuss the use of laser refrigeration to cool objects trapped in optical tweezers. Due to the spatial isolation provided by optical tweezers, it is easy for photothermal heat to build in the absence of a method to conduct the heat away. By using materials with laser refrigeration, we can offset this heat and measure particles without the threat of vaporization of the sample. We use alpha phase NaYF crystals in a set of optical tweezers to determine the minimum possible temperature for these crystals in vacuum tweezers, reaching temperatures as low as 241 K. We also investigate the use of dual-beam tweezers for trapping hexagonal beta phase NaYF. While no cooling was investigated during these experiments, we do demonstrate the stable trapping of the hexagonal platelets with wide aspect ratios. The provide a significant improvement in materials for levitated sensor disc applications due to the high laser irradiances they can withstand.

In chapter 5, we explore the other projects I have been able to participate in, including the laser refrigeration of YLF at extreme pressures through the use of a diamond anvil cell. The high pressures (more than 6 GPa) causes the YLF to undergo a phase change from a scheelite phase to a fergusonite phase, which alters the symmetry of the crystal lattice. This in turn affects crystal field splittings, which will affect the laser refrigeration. Even after the phase change has affected the crystal phase, laser refrigeration is still observed, though the magnitude is greatly diminished, going from more than 20 K below room temperature to only a few degrees. In this chapter, we also explore the generation of optical cavities through the deposition of chalcogenides via pulsed laser deposition. Quantum dots are coated on the deposited films to create cavities with quantum dots between the layers. We characterize and report the survival of the quantum dots through the pulsed laser deposition process.

Lastly, chapter 6 discusses significant conclusions from the experiments presented and discuss future work in the field of laser refrigeration.

TABLE OF CONTENTS

LIST OF FIGURES

GLOSSARY

NAYF: Sodium yttrium fluoride. Stoichiometry is kept vague due to the nonstoichiometric nature of the material.

EDTA: Ethylenediaminetetraacetic acid

XRD: X-ray diffraction

YLF: Yttrium lithium fluoride ($YLiF_4$)

CNT: Classical Nucleation Theory

DLP: Dense Liquid Phase

SD: Spinodal decomposition

TEM: Transmission electron microscopy

MD: Molecular Dynamics

MEEP: MIT Electromagnetic Equation Propagation

STEM: Scanning transmission electron microscopy

BET: Brunauer-Emmett-Teller

HRTEM: High resolution transmission electron microscopy

KYF: Potassium yttrium fluoride (KY_3F_{10})

NMR: nuclear magnetic resonance spectroscopy

SSNMR: Solid state nuclear magnetic resonance spectroscopy

MAS: Magic angle spinning

RMSD: Root-mean-square displacement

MEP: Minimum energy path

DFT: Density functional theory

NV^-: Negatively charged nitrogen vacancy center

ODMR: Optically detected magnetic resonance

ZPL: Zero Phonon Line

P1: Substitutional nitrogen center

NDS: Nanodiamonds

EPR: Electron paramagnetic resonance

IR-PHI: Infrared photothermal heterodyne imaging

DWF: Debye-Waller factor

CW: Continuous wave

PL: Photoluminescence

MW: Microwave

CVD: Chemical vapor deposition

HPHT: High pressure, high temperature

H3: Nitrogen-vacancy-nitrogen defect

NVN: Nitrogen-vacancy-nitrogen center

PSBS: Phonon side bands

NV^0: neutral nitrogen vacancy center

APD: Avalance photodiode

PLE: Photoluminescence excitation spectroscopy

COM: Center-of-mass

GWS: Gravitational waves

LSD: Levitated sensor detectors

PSD: Power spectral density

FEM: Finite element model

DAC: Diamond anvil cell

PLD: Pulsed laser deposition

APT: Atom probe tomography

QDS: Quantum dots

TDDFT: Time-dependent density functional theory

Some passages have been quoted verbatim from the following sources:

R. G. Felsted, A. Pant, A. B. Bard, X. Xia, D. R. Luntz-Martin, S. Dadras, S. Zhang, A. N. Vamivakas, P. J. Pauzauskie. "Chemically Tunable Aspect Ratio Control and Laser Refrigeration of Hexagonal Sodium Yttrium Fluoride Upconverting Materials." *Crystal Growth and Design* **2022**, *22* (6), 3605-3612.

R. G. Felsted*, A. B. Bard*, A. S. Ganas, A. Pant, C. Gupta, Y. Chen, E. Nakouzi, B. Jin, N. M. Washton, M. D. LaCount, C. J. Mundy, G. K. Schenter, J. Chun, S. R. Spurgeon, G. K. Lee, V. C. Holmberg, L. N. Brush, J. J. De Yoreo, P. J. Pauzauskie. "Multi-Step Crystallization and Chemical Evolution of Sodium Yttrium Fluoride." (In Preparation, 2023).

R. G. Felsted*, A. Pant*, A. B. Bard, X. Xia, S. Dadras, K. Shayan, D. R. Luntz-Martin, D. Mannikko, I. M. Pavlovetc, S. Stoll, M. Kuno, A. N. Vamivakas, P. J. Pauzauskie. "Solid-state laser refrigeration of nanodiamond quantum sensors." (In Preparation, 2023).

A. Pant, C. Gupta, K. Senkalla, **R. G. Felsted**, X. Xia, T. Spohn, S. T. Dunham, F. Jelezko, P. J. Pauzauskie. "Reduced photothermal heating in diamonds enriched with H3 point defects." *Journal of Applied Physics* **2022**, *131* (234401).

R. G. Felsted, J. Chun, G. K. Schenter, A. B. Bard, X. Xia, P. J. Pauzauskie. "The Role of Dynamics & Surface Roughness on Self-Assembly of Colloids by use of Optical Tweezers." (In Preparation, 2023).

** indicates equal contribution*

D. R. Luntz-Martin, **R. G. Felsted**, S. Dadras, P. J. Pauzauskie, A. N. Vamivakas. "Laser refrigeration of optically levitated sodium yttrium fluoride nanocrystals." *Optics Letters* **2021** *46* (15): 3797-3800.

R. G. Felsted*, G. Winstone*, Z. Wang*, S. Klomp*, A. Laeuger, C. Gupta, D. Grass, N. Aggarwal, J. Sprague, P. J. Pauzauskie, S. L. Larson, V. Kalogera, A. A. Geraci. "Optical Trapping of High-Aspect-Ratio NaYF Hexagonal Prisms for kHz-MHz Gravitational Wave Detectors." *Physical Review Letters* **2022**, *129* (053604).

A. S. Ganas, E. A. Dobretsova, A. Pant, B. Journaux, X. Xia, **R. G. Felsted**, P. J. Pauzauskie. "Solid-state laser refrigeration at GPa pressures." (In Preparation, 2023).

R. G. Felsted, A. Pant, A. B. Bard, C. Erickson, B. Bishop, L. Liu, R. Beck, D. Perea, S. R. Spurgeon, V. C. Holmberg, X. Li, D. R. Gamelin, P. J. Pauzauskie. "Colloidal Semiconductor Quantum Dots in Dichalcogenide Cavities Prepared through Pulsed Laser Deposition." (In Preparation, 2023).

** indicates equal contribution*

ACKNOWLEDGMENTS

Over the past five years, I have dedicated everything to developing myself as a scientist and as a person. At times, it seemed as though the end was forever distant, but with the constant support of everyone around me, I have finally come to end this long road. I would like to thank those who provided support along the way and made this all possible.

To my advisor, Professor Peter J. Pauzauskie: I cannot thank you enough for providing the structural framework and guidance that developed me as a scientist. Your constant support provided the means for me to focus on research and learning the necessary techniques and skills that I needed to succeed. Our long conversations about fundamental principles shaped the way I think about scientific problems, and your enthusiasm for science has left me eager for exploring questions and finding answers through careful experimentation and deep thought.

To my undergraduate advisor, Professor Steven R. Goates: You provided me the ideal introduction to chemistry as well as science as a whole. Your dedication to both a proper study of the natural world and the wellbeing of your students has always stayed with me, and I have aimed to shape both my scientific studies and my life as a man after the path you set for me. I can only hope that I live up to the example you have left for me.

To my internship mentor, Doctor Zheming Wang: Thank you for taking me under your wing during a turbulent and difficult time in my doctoral studies. You have shown a great deal of trust in me, and I am extremely grateful for that trust. I am excited to have worked under your guidance on so many interesting projects, and I

look forward to working together even more. Thank you for your trust and guidance.

To my senior graduate student fellows, Dr. Matthew Crane, Dr. Matthew Lim, Dr. Anupum Pant, Dr. Xiaojing Xia, Dr. Abbie Ganas, Dr. Elena Dobretsova, Stuart Frazier, and Alex Bard: I could not have made it to this point without your support. I stand on the ground that you all laid, and your kind willingness to teach me through long hours in the laboratory are allowed me to learn and grow. Our time together is what carried me along the way and kept me going through hard times.

To my junior graduate student fellows, Rachel Gariepy, Chaman Gupta, Lars Forberger, Sankhya Hirani, Alexey Soldatenko, Andy Feng, and Andrew Nuhaily: I am grateful for the opportunity to mentor and help you all. Your eagerness to learn kept me grounded and reinvigorated my desire to be a scientist. Your insights into my research helped push me along to this point, and I will always be grateful for the experiences we had together.

To my siblings, Rachel, Amy, Daniel, and Emily: I am the man I am today in large part to you all. I could not have made it this far without your love and support. You provided the example to me on how to properly live my life, and guided me through my mistakes and missteps along the way. Thank you for your constant support, and know that I love you, now and forever.

Finally, To my parents, Nick and Madeleine: I owe everything to you. I cannot write into words all that you have done for me. From my earliest days, you have been leading me and guiding me. Whether it be teaching me to read at home from letters we got in the mail or taking the time to make sure my education was everything that it could be, you are the reason that I am where I am. Everything I do is to make you proud, and I hope that I am succeeding in doing so. I love you.

DEDICATION

to my beloved family

Chapter 1
INTRODUCTION

Photothermal heating is a near-constant effect in systems involving lasers. Due to the conservation of energy, any excess energy during an energy transfer must go somewhere, which usually leads to the remaining energy being expressed as heat, and excited states may relax and generate heat as well. This photothermal heating can be problematic in experiments. When the heat cannot be easily dissipated or if the sample is particularly sensitive, the sample may be destroyed by burning or vaporization. Photothermal heating may also cause changes in material properties which can be difficult to precisely control. Many experiments require varied optical power, which will lead to varying temperatures by photothermal heating. This can cause erratic behavior in sensitive measurements, which needs to be offset or controlled through some means.

1.1 Motivation

Photothermal heat is normally managed through the use of heat sinks and heat exchangers. This may work for many bulk systems, but these methods of heat mitigation can introduce new problems through vibrations and additional mass in sensitive systems. Additionally, they cannot be easily applied to many nanoscale systems and are not typically responsive at fast time scales. This leads to the need for a method to cool materials and samples that can be applied evenly regardless of size scale or time scale.

There are also conditions where physical contact between the sample and a heat sink or exchanger is not physically possible, such as with levitated sensors. These

systems use optical tweezers to remove the sensor from any surrounding environment. If a vacuum is also pumped, then the sensor can theoretically be isolated from contact with any surrounding system, allowing for precision measurements. However, this isolation also comes with the drawback that heat cannot be dissipated through conduction or convection. It is not uncommon for these levitated sensors to be vaporized due to extreme temperatures achieved during the measurement. To overcome these issues, we need a non-contact method of cooling that can apply to both bulk systems and nano-scale systems at fast time scales, which can be solved with laser refrigeration.

1.2 Laser Refrigeration

There is a long history regarding the science of laser refrigeration (often also called laser cooling or optical refrigeration, all of which are synonymous). Laser refrigeration was first proposed as a possible experiment in 1929 by Peter Pringsheim[1], who suggested that it may be possible to cool sodium vapor atoms by exciting them with lower energy wavelength and forcing them to emit a higher energy wavelength. This idea led to the process of Doppler cooling, formally conceived in 1975. While this kind of cooling is possible, it only applies to atoms in the vapor phase at low pressures. By exciting just below the electronic transition, the transition can coupled with another transition to make the transition possible. While the viability of the process was debated early on, this was deemed thermodynamically possible by Landau in 1946 due to the increase in entropy from a low-entropy excitation light source to the high-entropy emitted light from the cooled sample.

While Doppler cooling is only possible in the vapor phase, a form of solid state cooling was proposed by Kastler in 1950 by using rare earth ions in crystalline material due to their sharp emission lines and extremely high quantum efficiency. However, it was difficult to experimentally test this due to fact that the laser had not been invented yet. After the invention of the laser, many people tried to observe laser

cooling through anti-stokes luminescence, but it was not observed experimentally for several decades, not until 1995 by Epstein.[2] Epstein used a heavy metal fluoride glass doped with ytterbium ions called ZBLAN:Yb^{3+} that was able to demonstrate a net cooling of 0.3 K. While this may not seem like a great deal of cooling, this was the very first demonstration of laser cooling for a solid state object at room temperature, and further developments have been made since then.

Improvements in material synthesis and engineering design has further increased the capabilities of solid state refrigeration to the point where it is possible to cool bulk materials to temperatures below 100 K from room temperature without the of any heat sinks, thermoelectric coolers, or cryogenic fluids.[3] Even materials that were not traditionally considered good prospects for laser refrigeration have been shown to be able cool significantly, such as silica. Recent work from the Sheik-Bahae group has shown that Yb doped silica fibers can be cooled by 18 K below room temperature, which could have large implications for radiation-balanced lasers and for telecommunication applications.[4]

While bulk materials have had major progress, there has also been development using laser refrigeration on nano and micro materials. While bulk materials are typically grown from melt, microcrystals and nanocrystals are typically grown hydrothermally or solvothermally. This often requires the use of ligands to control the size and morphology, which will lead to heating at the surface of the crystals. Combined with the fact that microcrystals have comparably high surface areas, this poses a serious challenge to laser cooling microcrystals. Additionally, it is possible that there are surface states and surface reconstructions that further inhibit any cooling by providing non-radiative decay pathways that lead to heating. Despite these challenges, laser cooling has been shown in these materials, including the report of cooling in 5 μm $YLiF_4$ (YLF) crystals in physiological conditions by more than 10 K.[5] However, this area of laser refrigeration is considerably less explored than with bulk crystals, and much work remains to be done with cooling nano and microscale materials.

1.2.1 Laser Refrigeration Mechanism

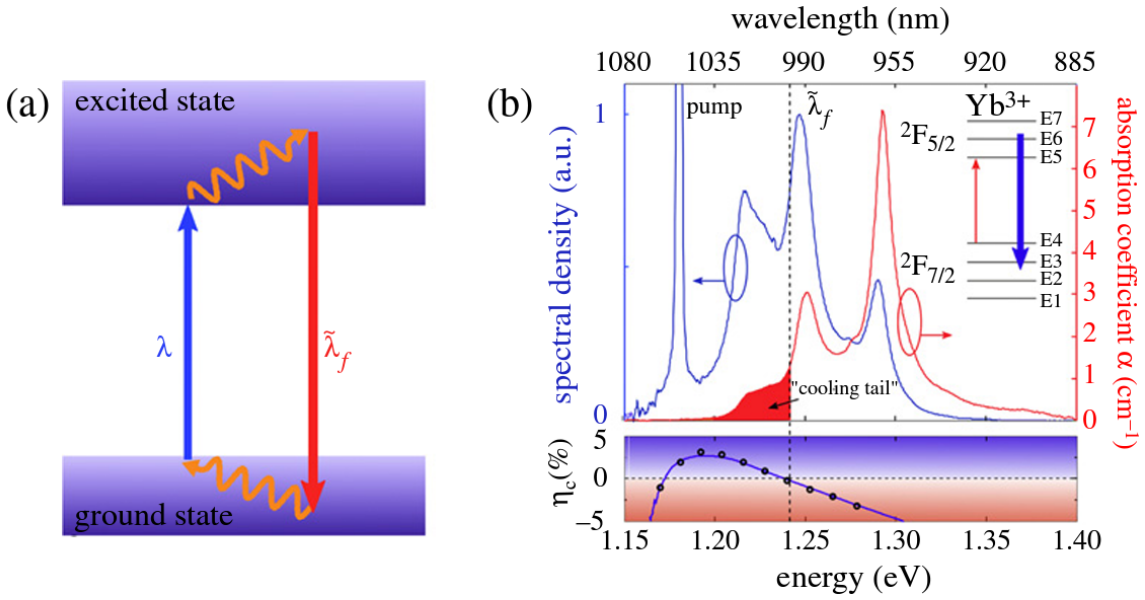

Figure 1.1: (a) Schematic energy diagram of a laser cooling cycle in a solid: an optical input at wavelength λ excites the electronic transition from a ground state to an excited state of an ion doped into a host matrix. After thermalization (wavy arrows within manifolds), excitation relaxes radiatively with an mean emission wavelength $\tilde{\lambda}_f < \lambda$. (b) Top, absorption (red) and emission (blue) spectra for a transition between $^2F_{7/2}$ and $^2F_{5/2}$ multiplet states of Yb^{3+}-doped $YLiF_4$ (Yb:YLF) at 300 K; excitation (labeled "pump") is below the mean emission wavelength $\tilde{\lambda}_f$, i.e., in the "cooling tail" (shaded) of the absorption curve. Bottom, data points (open circles) and fit of the cooling efficiency (η_c) spectrum of Yb:YLF. Cooling (η_c) occurs slightly below $\tilde{\lambda}_f$ and reverses sign at longer wavelengths because of background absorption. Reprinted with permission from [6] ©The Optical Society.

Under standard conditions, materials will not spontaneously absorb low energy light and emit high energy light with high efficiency. This process, commonly referred to as anti-Stokes luminescence, can occur when selectively excited with red-shifted light with respect to the normal transition wavelength. However, the normal luminescence process is Stokes luminescence where blue-shifted light is absorbed, and then red-shifted light is emitted. During Stokes luminescence, the remaining energy from

the original photon is commonly converted to photothermal heat. In anti-Stokes luminescence, there is no remaining energy after the transition. In fact, energy must be taken from the system to make the transition occur. This process can be seen in Fig. 1.1. For this to lead to cooling, however, there must be enough radiative emission to overcome any nonradiative relaxation. This process efficiency, referred to as quantum efficiency, must be approaching perfectly efficient for cooling to occur due to the low amount of upconverted energy compared to the overall photon energy. One nonradiative relaxation event will convert the photon energy into heat, offsetting dozens of anti-Stokes luminescence events. But if the process can approach near-unity quantum efficiency, the overall system will cool down, and laser refrigeration will have occurred.

The cooling efficiency of the anti-Stokes luminescence process is what dictates how high the external quantum efficiency must be. The cooling efficiency for the anti-Stokes process is defined as

$$\eta_c = \frac{h\nu_f - h\nu}{h\nu} = \frac{\nu_f}{\nu} - 1 = \frac{\lambda}{\lambda_f} - 1 \tag{1.1}$$

where η_c is the cooling efficiency, h is plank's constant, ν is the excitation photon frequency, λ is the excitation photon wavelength, ν_f is the fluorescence photon frequency, and λ_f is the fluorescence photon wavelength. While this is technically correct, it only applies to ideal systems with no losses due to nonradiative relaxation. If other contaminants are present that can absorb, we need to correct for background absorption. This modified absorption efficiency is

$$\eta_{abs} = \frac{\alpha_r}{\alpha_r + \alpha_b} \tag{1.2}$$

where α_r is the resonant absorption due to the rare earth ions and α_b is the background absorption from contaminants and impurities.

In addition to correcting the absorption efficiency, we must also correct for nonradiative relaxation. The quantum efficiency is used to correct for this, which is defined

to be

$$\eta_e = \frac{W_{rad}}{W_{rad} + W_{nr}} \tag{1.3}$$

where η_e is the quantum efficiency, W_{rad} is the radiative relaxation, and W_{nr} is the nonradiative relaxation. However, the quantum efficiency is not enough on its own. Emitted photons can become trapped in the crystal due to internal reflections, as well as reabsorption events can occur. To correct for this issue, we modify the quantum efficiency to extract the external quantum efficiency, which is the chance for photons to escape the crystal after an absorption event. The external quantum efficiency is defined in this case to be

$$\eta_{ext} = \frac{\eta_e W_{rad}}{\eta_e W_{rad} + W_{nr}} \tag{1.4}$$

where η_{ext} is the external quantum efficiency. When corrected for both absorption efficiency and external quantum efficiency, the final cooling efficiency looks like

$$\eta_c = \eta_{ext}\eta_{abs}\frac{\lambda}{\lambda_f} - 1 \tag{1.5}$$

which corrects for both background absorption and reabsorption probabilities. Due to physical limitations in upconversion probability, the ratio of λ over λ_f is only slightly greater than one. This means that the product of η_{ext} and η_{abs} must be near one in order to have a nonzero cooling efficiency. Background impurities must be nearly nonexistent, and the doping level of rare earth ions must be low to prevent reabsorption. While a low rare earth level is required, this also limits cooling power, since the rare earth is what drives the cooling, leading to an engineering challenge of optimizing cooling power while minimizing reabsorption. When the system is optimized properly, however, η_c becomes positive, which means that anti-Stokes luminescence is carrying heat out of the system and the system as a whole is cooling.

1.2.2 Materials for Laser Refrigeration

As discussed earlier, solid state laser refrigeration was first achieved using ZBLAN:Yb^{3+}, a heavy metal fluoride glass with fluorides of zirconium, barium, lanthanum, alu-

minum, and sodium. Fluorides are desirable for laser refrigeration applications due to the low phonon energy, which is a barrier to thermal upconversion and must be kept low for laser refrigeration. Yb^{3+} is the most common rare earth fluoride used due to its electron configuration leading to only the ^2F manifold for the state of the ion. Due to spin-orbit coupling, the ^2F manifold of the Yb^{3+} ion splits into the $^2F_{7/2}$ and $^2F_{5/2}$ multiplets, which makes the optical transitions of Yb^{3+} relatively simple compared to other rare earth ions. While amorphous glasses such as ZBLAN can be laser refrigerated, crystalline materials are typically preferred as it limits the inhomogenous broadening of the absorption of the rare earth ions in the crystal. This means that the $^2F_{7/2}$ and $^2F_{5/2}$ multiplets have discrete energy levels depending on the crystal field splitting of the host lattice containing the rare earths.

The Yb^{3+} ions in the crystal can be treated as an ensemble in determining the average state of an Yb^{3+} ion in the host lattice. The ions follow a Boltzmann distribution of states in the $^2F_{7/2}$ based on the thermal energy available. For laser refrigeration to occur, the minimum photon energy must be used to prevent energetic downconversion. This means that ions must be excited from the uppermost state of the $^2F_{7/2}$ multiplet to the lowest state of the $^2F_{5/2}$ multiplet, which is usually around 1020-1030 nm for Yb^{3+} ions in the most common laser refrigeration materials. The Boltzmann distribution of states becomes very important to laser refrigeration since ions must be in the uppermost state of the $^2F_{7/2}$ multiplet. The larger the crystal field splitting applied, the wider the energetic gap and fewer ions will be in that state. To counteract this, crystals with very low crystal field splitting offer the best potential for laser refrigeration. For this reason, YLF is the most commonly used material since it can be grown in bulk and has a very low crystal field splitting in the ground state ($\sim 477 \pm 10$ cm^{-1}). The beta phase of NaYF offers lower crystal field splitting, but the hexagonal crystal structure has large thermal expansion coefficient anisotropy, preventing it from being grown from melt due to strain and cracking when cooling the crystal down. NaYF can still be used as microcrystals due to the less extreme

conditions of hydrothermal synthesis, and it has been shown to cool, though its use is not common yet.

1.3 Optical Tweezers

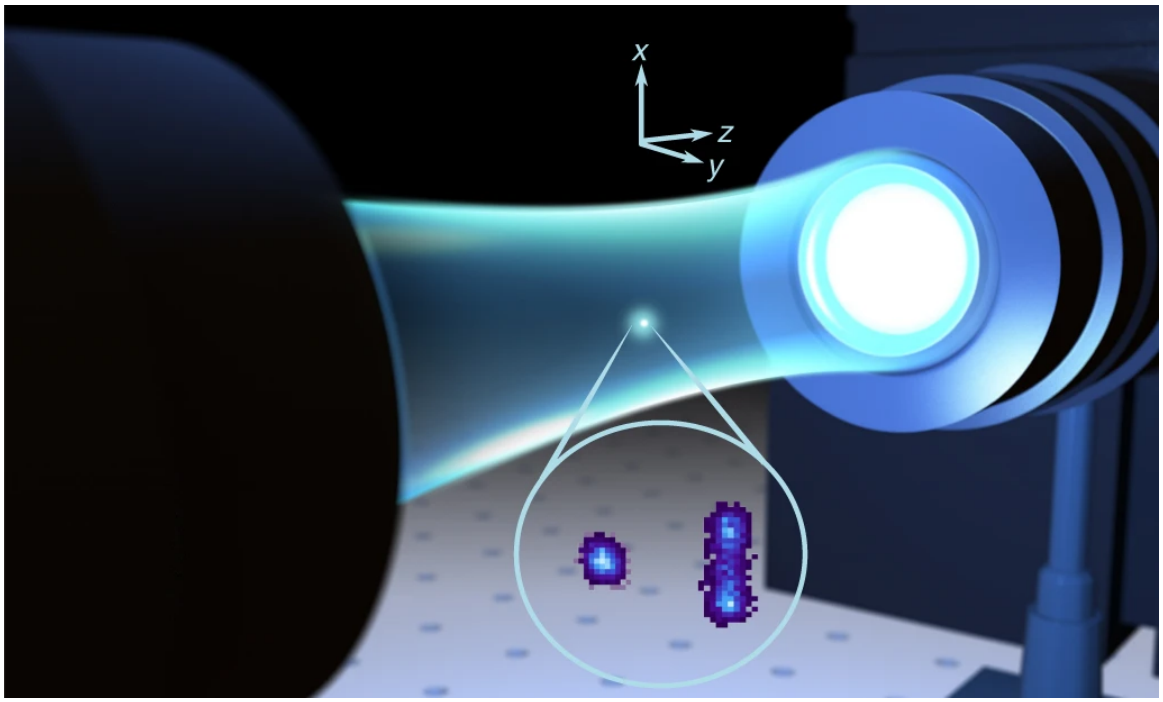

Figure 1.2: Artistic rendering of a silica nanosphere levitated in vacuum by an optical tweezer. Inset: motion of the levitated sphere's centre of mass observed in the plane transverse to beam propagation, showing Brownian motion below threshold (left) and coherent oscillation along the x axis above threshold (right). Reprinted with permission from [7].

Optical tweezers are a versatile instrument for the manipulation of micro and nano scale materials. They are capable of many applications, including ultra-precise force sensing,[8] magnetometry,[9, 10] microfluidic control of biological samples,[11, 12] optical refrigeration,[5, 13, 14] generating squeezed light,[15] and quantum computers,[16, 17] among other applications. Since then, optical tweezers have been used for micromanipulation in many experiments, especially biological experiments.

First developed in 1970 by Arthur Ashkin,[18] who went on to observe that light could trap transparent dielectric spheres,[19] optical tweezers are the use of tightly focused light to trap objects near the focal plane of the light. This discovery directly led to the trapping of atoms and laser cooling of atoms discussed above, which received the physics Nobel prize in 1997. In addition to Doppler cooling, atom trapping has been used in many breakthrough experiments, including the observation of Bose-Einstein condensates as well as atomic clocks. Optical tweezers are so critical to many scientific experiments that Ashkin himself received the physics Nobel prize just four years ago in 2018 for his work in discovering optical tweezers. Despite their use in fundamental physics experiments, optical tweezers are more widely known for their applications in biology. They enable experiments with isolated single cells or proteins and allows for the direct probing of systems that are otherwise difficult to measure, such as cellular mobility, cellular assembly, or biological motor strength. More recently, there has been great interest in using optical tweezers to trap nanocrystals and 2D materials, such as quantum dots, nanodiamonds, and graphene/graphene oxide.

1.3.1 Optical Twezers Mechanisms and Forces

Optical tweezers work by focusing a laser through high numerical aperture objective. This focuses the light to a near diffraction limited spot. This tightly focused light generates a strong electric field gradient, described first in Ashkin's paper. This strong electric field gradient generates two forces that act upon nearby particles. These forces are the gradient force and the scattering force (sometimes referred to as radiation pressure). The gradient force arises from the induced dipole caused by the electric field gradient, and it is expressed by

$$F_{grad} = \frac{1}{2}\alpha \nabla E^2 \tag{1.6}$$

where F_{grad} is the gradient force, α is the particle's polarizability, and E is the electric field. The gradient of the electric field what drives this force, which is why a tightly focused electric field is required. If the electric field does not strongly vary over the size of the particle, there will be little force driving the particle into the trap, and the trapping felt due to the gradient force becomes stronger as the particle gets closer to the focal plan of the trapping laser.

The other major force experienced due to the optical tweezers is the scattering force. This force is caused by the scattering of the photons from the trapping laser off of the surface of the particle. When photons reflect off of the surface of the particle, momentum is imparted during this process. When considered using the Rayleigh approximation, this force can be expressed as

$$F_{scat}(r) = \frac{k^4\alpha^2}{6\pi c n_0^2 \epsilon_0^2} I(r)\hat{z} \tag{1.7}$$

This force pushes the particle along the direction of beam propagation, which in contrast to the gradient force, which draws particles to the center. This balance of forces causes particles to be most stable slightly out of the focal plane of the laser trap. This can shift in stable position can be minimized by the use of a high numerical aperture focusing lens or objective, which causes the beam to be focused at sharp angles that minimize the scattering force. This is important for imaging inside the trap, where most useful information is, as well as for stable trapping. Since the gradient of the electric field is strongest at the focal plane, minimizing the scattering force is essential to creating strong traps for stable isolation of particles.

Chapter 2

SYNTHESIS OF RARE EARTH FLUORIDES

2.1 Synthesis of Hexagonal Sodium Yttrium Fluoride

While most rare earth fluorides are grown from melt, this method is not viable for the beta phase of sodium yttrium fluoride (β-NaYF). The hexagonal crystal structure leads to anisotropic thermal expansion coefficients. This causes immense strain on the crystal as it cools from the melt, leading to fracture and polycrystalline products. To explore solutions to this issue, we explore the possibility of using hydrothermal synthesis to grow β-NaYF while avoiding extreme temperatures.

2.1.1 Introduction to β-NaYF Hydrothermal Synthesis

Alkali-fluoride crystals doped with trivalent lanthanide cations are currently under active investigation based on their large infrared-to-visible optical upconversion efficiency and corresponding applications. These materials can be used directly as luminescent phosphors,[20, 21] laser gain crystals,[22] and radiation balanced lasers,[23] or they can be used in broader applications for quantum information science,[24] solar energy harvesting,[25] localized temperature control,[26] counterfeit protection,[27, 28, 29] in vivo refrigeration,[5] labeling of biological tissues,[30] and vision therapy.[31] These rare-earth-doped alkali-fluoride materials have also proven to be leading candidates for solid-state laser refrigeration based on antistokes photoluminescence with near-unity quantum efficiency.[32]

While optical refrigeration of metal atoms in the gas phase was proposed in 1929 by Pringsheim,[1] solid-state refrigeration was not experimentally observed until 1995 by Epstein.[2] Rare-earth-doped fluoride crystals have been laser-refrigerated to cryo-

genic temperatures without the need for electrical contacts or mechanical vibrations from moving parts that are detrimental to sensitive optical measurements.[33, 34, 35] Recent progress has demonstrated laser cooling in physiological media[5] and to a record low temperature of 91 K in vacuum.[36]

Among alkali-fluoride crystals, significant attention has been given to the beta phase of NaYF, which is a crystal with a variable, nonstoichiometric composition $Na_{3x}Y_{2-x}F_6$.[20] β-NaYF has been calculated to have significantly lower crystal field splitting compared to most rare earth fluoride crystals, suggesting that it has the potential to reach cryogenic temperatures.[37] However, β-NaYF has not been thoroughly explored for optical refrigeration due to difficulties in growing bulk single crystals.[38] The large anisotropy within the hexagonal structure's thermal expansion coefficient causes thermal stresses and fracturing of crystals grown using Czochralski processing. While bulk crystals are limited by this effect, microcrystals of β-NaYF have been grown using a Bridgman process,[39] and nanocrystalline $NaLnF_4$ has been precipitated out of glass matrices.[40]

An alternative to growing crystals from a melt is hydrothermal synthesis. Single-crystalline β-NaYF can easily be grown via hydrothermal and solvothermal methods with a wide array of morphologies.[41, 42, 43, 44, 45, 46] Synthesizing via hydrothermal processes allows for several advantages, including the ability to consistently grow single-crystalline β-NaYF, lowered cost of synthesis, and controlled morphology of the product.[47] In addition to these benefits, β-NaYF is safer to grow relative to other rare earth fluoride crystals in that sodium fluoride (NaF) can be used as a fluoride precursor due to the high solubility of NaF in water (43 g/L at 25 °C). In contrast, growing $LiYF_4$ requires the use of ammonium bifluoride (NH_4HF_2), a hazardous reagent that produces HF during hydrothermal synthesis.

Recently, nanowires of β-NaYF have been synthesized and used for solid-state laser refrigeration in physiological media.[48] However, these materials were only shown to undergo solid-state laser refrigeration in one nanowire morphology with little con-

trol over the final aspect ratio and size of the product. Growing larger microcrystals would increase the length of the beam path, allowing for greater absorption of the cooling laser and greater cooling power than their nanocrystal counterparts. There is also the possibility for large hexagonal discs to exhibit cavity (Mie) resonances,[49] including whispering gallery modes,[50] if they can be grown with appropriate dimensions. However, to date cavity resonances have not been investigated in the context of solid-state laser refrigeration in large part because synthetic methods are not readily available for growing β-NaYF microcavities with control over final cavity dimensions. Other synthetic methods either cannot grow crystals sufficiently large or have poorly formed facets that are not suited for optical cavity resonances.

2.1.2 Method for Synthesizing β-NaYF with Aspect Ratio Control and Construction of Composite Devices

β-NaYF crystals were grown using a hydrothermal process in a stainless-steel autoclave (Parr Instrument Company). YCl_3, $YbCl_3$, $ErCl_3$, $TmCl_3$, and ethylenediaminetetraacetic acid (EDTA) were used to create a chelated rare earth precursor solution with NaOH used to assist in dissolving the EDTA. NaF was dissolved to form the fluoride precursor solution. Nine equivalents of YCl_3 and one equivalent of $YbCl_3$ were dissolved in water to make a stock solution of 0.2 molarity (M) YCl_3:10% $YbCl_3$ (90% by moles YCl_3, 10% by moles $YbCl_3$). $ErCl_3$ and $TmCl_3$ can be added to this solution as dopants for upconversion/anti-Stokes luminescence experiments. EDTA was dissolved in water with 3 equiv of NaOH to make a 0.2 M tri-sodium EDTA solution. NaF was dissolved in deionized water (ρ = 18.2 MΩ·cm) to make a 1 M stock solution.

A typical synthesis went as follows: 5 mL of 0.2 M YCl_3 (10% $YbCl_3$) was placed in an autoclave liner and chelated with stirring by 5 mL of 0.2 M tri-sodium EDTA for 10 min. Four milliliters of 1 M NaF was then added drop by drop to the mixture and stirred vigorously for 30 min. The mixture was then transferred to a stainless-steel

autoclave and heated in an oven at 230 °C for 24 h. The autoclave was allowed to cool down to room temperature naturally. The sample was collected from the autoclave liner and isolated by centrifugation and then washed twice with water and twice with ethanol. The sample was then dried at 80 °C for 12 h, followed by calcination at 300 °C for 4 h in air to remove surface ligands and adsorbents. A schematic of the reaction is shown in Figure 2.1.

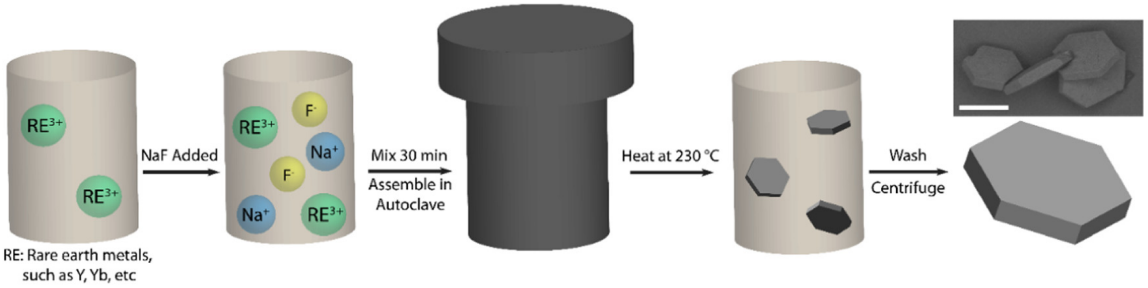

Figure 2.1: Synthesis of β-NaYF microcrystals. A schematic diagram for the hydrothermal synthesis of β-NaYF microcrystals. A YCl_3 solution (doped with rare earth chlorides) is chelated with EDTA. NaF is added drop by drop, and the mixture is stirred for 30 min. This is then heated at 230 °C for at least 24 h and then washed and centrifuged to isolate the product. Scale bar represents 2 μm.

To maximize the potential cooling of the crystals, we need to isolate the contact with other materials to prevent unwanted heat conduction. To minimize contact heating, devices were constructed with optomechanical CdS nanoribbon cantilevers synthesized according to Pant et al.[51] This thermally isolates the crystals from the silicon substrate and also provides a method of thermometry. Samples were prepared for optical measurements by use of a nanomanipulator with a tungsten dissecting probe. A CdS nanoribbon was placed hanging off the edge of a silicon substrate with the nanomanipulator, allowing the CdS nanoribbon to function as an optomechanical cantilever for β-NaYF crystals. A single crystal was deposited on the end of the cantilever with the nanomanipulator. The silicon substrate with the sample was then transferred to an optical cryostat. All optical measurements were done with a

1020 nm diode laser. The sample devices were placed over the main axial window of the cryostat to allow for both forward-scattered laser radiation and back-scattered photoluminescence to be collected. The forward-scattered laser radiation was focused onto an avalanche photodiode. The voltage was collected in real time for 1 s and then was Fourier transformed from the time domain to the frequency domain to read out the vibrational eigenfrequencies of the sample cantilever. Back-scattered photoluminescence from Yb^{3+} ions was collected by a spectrometer fitted with a silicon EM-CCD detector after filtering to remove the cooling laser with a 1000 nm shortpass filter. All temperatures reported were calibrated in the cryostat using a temperature controller while using sufficiently low laser irradiance to not affect the sample temperature within our measurement sensitivity (10 kW/cm^2).

2.1.3 Characterization of β-NaYF Product and Analysis of Synthesis Results

The synthesis yielded a white powder of hexagonal β-NaYF crystals. These crystals varied in size from microplatelets to microrods depending on synthesis parameters, discussed in more detail below. The microplates had diameters up to 5 μm and thicknesses of 250 nm, and the microrods had diameters of 700 nm and heights of 1.25 μm. The resultant powder was confirmed to be β-NaYF using both X-ray diffraction (XRD) analysis and select area electron diffraction.

The phase of the product is highly dependent on the temperature of the reaction. At temperatures below 160 °C, only the nonstoichiometric cubic alpha phase (represented by $Na_{0.5-x}Y_{0.5+x}F_{2+2x}$) was observed with x $\sim$ 0.07.[52] The alpha NaYF (α-NaYF) grains exhibited a quasispherical nanocrystalline morphology with diameters of approximately 100 nm. At 180 °C, the reaction leads to some residual α-NaYF remaining in the product, indicating the parallel synthesis of both phases. To avoid the incomplete formation of β-NaYF, the reaction was run at 230 °C to ensure that the reaction ran to completion.

The β-NaYF morphology was highly dependent on the presence of EDTA. EDTA is

not strictly required to synthesize the β-NaYF phase; however, the resulting product is limited to rods with faceted ends. This faceting is undesirable for the goal of using these crystals as optical microcavities for enhanced absorption and cooling. The addition of EDTA removes this faceting and produces flat hexagonal faces. The exact mechanism for this process is unknown, but it appears to be due to preferential binding of the EDTA along the (0001) Miller plane of β-NaYF crystals.

Other synthesis parameters were investigated including the pH of the EDTA solution and the length of time for the reaction. The pH of the EDTA solution was increased with NaOH. This causes deprotonation of the carboxylic acid groups on EDTA and affects the chelation of trivalent cations (Y^{3+} and Yb^{3+}) with EDTA. Previous work on the synthesis of β-NaYF has shown morphological dependence on pH in similar systems using sodium citrate.[43] In our system, a severe reduction in the solubility of EDTA began to occur at pH values below 7.0, though successful syntheses were run at pH values as low as 6.0. Below pH values of 6.0, incomplete conversion of α-NaYF to β-NaYF was observed. Under basic conditions (pH $>$ 8.0), the net size of the β-NaYF crystals decreased significantly. Because pH provided poor control of the system, all future syntheses were run at a pH of 7.0.

Using time to control particle morphology was also not successful. Short time scales (6–12 h) allowed for the formation of α-NaYF as well as irregular faceting of β-NaYF. Reactions held for 24 h showed complete conversion to β-NaYF as well as high crystallinity. Beyond 24 h, there was no observable difference in the product of the reaction, indicating that modifying the reaction time alone cannot be used as an effective parameter for controlling the morphology and the aspect ratio of β-NaYF.

The ratio of fluoride to trivalent cations has been reported to control the morphology and the aspect ratio of β-NaYF materials.[53] The increase in fluoride ions causes longer crystals due to increased growth along the high-energy (0001) hexagonal Miller plane. Varying the fluoride to trivalent cation ratio allows for extensive aspect ratio control, as shown in Figure 2.2. A stoichiometric ratio of 4 parts NaF to 1 part triva-

lent cation (4:1) yields a microplatelet that is disclike in appearance (Figure 2.2a). Increasing the fluoride content to a 6:1 ratio yields hexagonal microprisms (Figure 2b). Increasing the fluoride concentration further to a ratio of 8:1 yields microrods (Figure 2.2c). Ratios higher than 8:1 lead to large defects in the crystal formation, while ratios below 4:1 lower the overall product yield with no observed change in morphology. The fluoride to trivalent cation ratio gave control over the aspect ratio from 0.5 to 10.5 as measured by corner-to-corner diameter divided by thickness.

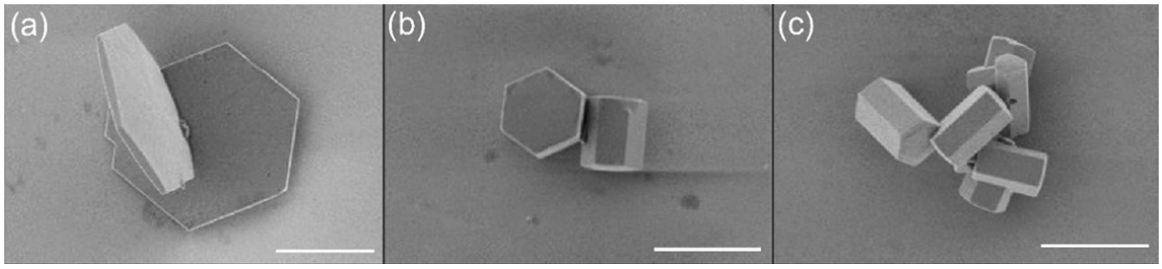

Figure 2.2: Aspect Ratio Control of β-NaYF Product. SEM images of β-NaYF microcrystals synthesized with NaF to rare earth molar ratios of 4:1 (a), 6:1 (b), and 8:1 (c). Scale bars represent 2 μm.

After the synthesis, the β-NaYF crystals remain coated with EDTA, which can inhibit any optical refrigeration from occurring. The EDTA capping creates a slight bulging effect with crystals appearing thicker in the center than at the edges. The immediate β-NaYF product was calcined in air to remove organic material from the surface that could increase the background absorption of the cooling laser. If the β-NaYF is only partially calcined, the crystal appears flat with the sections of EDTA significantly elevated from the surface, demonstrating the thickness of the EDTA coating. After fully calcining the crystals, the root-mean-square roughness was observed to be less than 1 nm. All materials tested for cooling were first calcined at 300 °C for 4 h to remove EDTA from the surface of the crystal.

2.1.4 Laser Refrigeration of β-NaYF Microcrystals

The β-NaYF crystals showed strong Yb^{3+} upconversion when excited with a 1020 nm laser. This emission (shown in Figure 2.3a) comes from the $^2F_{5/2} \rightarrow {}^2F_{7/2}$ transition and is characterized by a strong peak centered at 977 nm with a broad set of overlapping peaks from 980 to 1030 nm. A considerable portion of the broadness arises from the nonstoichiometric variation in the crystal structure due to fractional Yb^{3+} occupation at trivalent cation sites in the crystal.[38] The differences in an atomic composition will cause energetic differences at the local level of an individual unit cell. Over the scale of an entire microcrystal, this variation results in the broad emission bands observed. In addition to the fractional occupancy, the stoichiometry of the β-NaYF is also variable and can be described as $Na_{3x}Y_{2-x}F_6$ in contrast to the commonly used stoichiometry of $NaYF_4$.[20, 54] The emission can potentially vary between the synthetic batches of β-NaYF due to the variable stoichiometry and mol % of NaF versus YF_3 in β-NaYF.[55] While these fluctuations are typically small, their impact may complicate optical thermometry. The locations of photoluminescence peaks can be elucidated somewhat further by probing the upconverted luminescence when the sample is cooled to 77 K (Figure 2.3b). At cryogenic temperatures, peaks begin to emerge at 985, 992, and 997 nm, though the peak width limits the resolution of other peaks.

The laser refrigeration of these materials was first investigated through noncontact optical thermometry based on fitting different photoluminescence regions to a Boltzmann distribution based on previous work in similar materials.[56, 57] Two separate peaks were chosen from the same luminescence band and were integrated. The relative area of each peak was related to the Boltzmann distribution of the population of the energy levels from thermal upconversion and can be calibrated for thermal sensing.[58] The experimental setup is shown in Figure 2.4a, and an SEM micrograph of a device can be seen in Figure 2.4b. The photoluminescence of the β-NaYF was

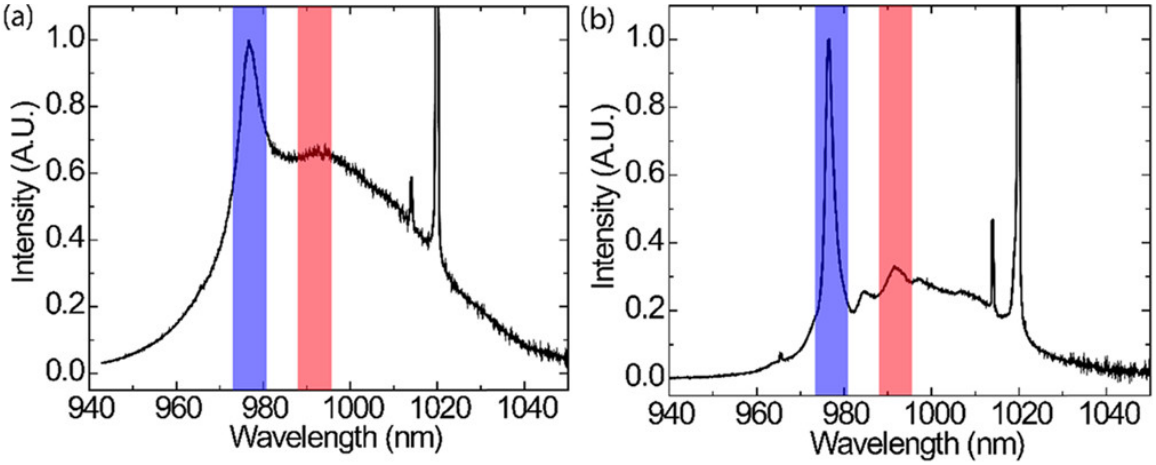

Figure 2.3: PL of 10% Yb^{3+}-doped β-NaYF crystals excited with a 1020 nm laser at (a) 295 K and (b) 77 K. The PL shown is from the Yb^{3+} $^2F_{5/2} \rightarrow {}^2F_{7/2}$ transition. The intensity was normalized to the 977 nm peak. The blue- and red-shaded regions show the integration regions used for optical thermometry. The sharp peak at 1020 nm is an unfiltered excitation laser line, while the other sharp peak at 1013 nm is a weak secondary line from the 1020 nm laser.

integrated over two different areas, from 973 to 981 nm over the first strong peak and from 988 to 996 nm over the second strongest peak. The ratio of the intensities of these areas should be proportional to the temperature of the crystal lattice, but the broadness of the emission makes it difficult to determine if the shift in emission is purely because of a Boltzmann distribution shift in the two peaks being integrated or if overlap from nearby peaks is contributing significantly to the shift in relative intensities. While this complicates the thermometry, the temperature of the crystal can be calculated at various irradiances by calibrating the ratio in a cryostat at known temperatures. After calibrating, the ratiometric analysis shows the β-NaYF crystals from this synthesis to be capable of cooling by at least 12.5 °C (Figure 2.4c). Based on previous work on the heat transfer of rare earth fluoride microcrystals on CdS nanoribbons, we anticipate heat transfer lifetimes in microsecond time scale.[59]

One difference this sample shows from previous work on YLF is the saturation ir-

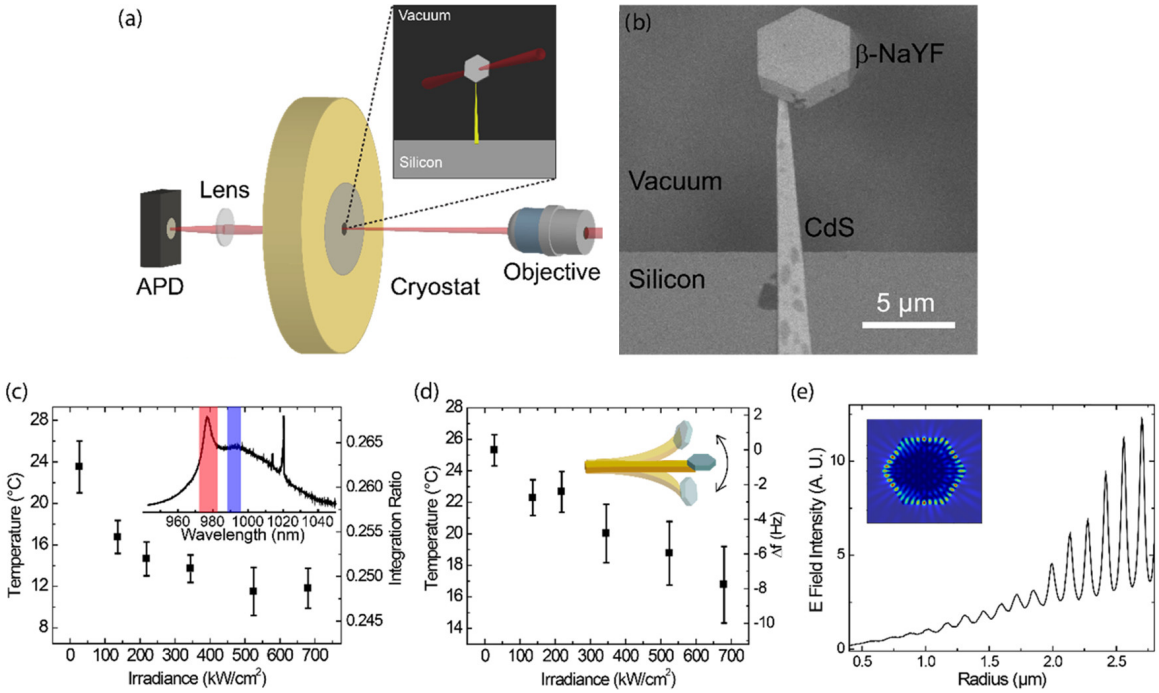

Figure 2.4: Laser Refrigeration of β-NaYF microcrystals. (a) Schematic of the optical setup used to collect PL from β-NaYF crystals. (b) SEM micrograph of the β-NaYF CdS cantilever device. (c) PL cooling data of the β-NaYF crystal. Error bars represent one standard deviation from six different measurements. Inset: Integration regions for the β-NaYF luminescence. (d) Eigenfrequency data of the CdS cantilever. Error bars represent one standard deviation from six different measurements. (e) Electric field intensity from a 1020 nm laser inside a hexagonal β-NaYF crystal as a function of crystal radius from FDTD calculations.

radiance of Yb^{3+} ions. Bulk YLF has shown saturation on the order of approximately 100 kW/cm^2, yet the sample we have shown does not appear to fully saturate before at least 700 kW/cm^2. This is in part due to the unique size and morphology of our sample. We are not irradiating at Brewster's angle, so we anticipate that reflections will reduce the absorption of the light to some degree. Additionally, the size of the β-NaYF crystal is close to the size of the focal point of the light, in stark contrast to bulk YLF. This will likely lead to a high degree of scattering, reducing the absorption of the crystal. Overall, we anticipate that significantly higher irradiances of 1020 nm

laser light are needed to achieve saturation due to these effects.

The crystals were separated from the silicon substrate using CdS cantilevers. This prevented heat from the silicon wafer entering the crystal, and the CdS cantilever used to suspend the β-NaYF crystal can also be used as a method of thermometry. The Young's modulus of the CdS nanoribbon is sensitive to temperature, causing a shift in the frequency of the fundamental vibrational mode.[51] These vibrations arise spontaneously from the thermomechanical noise of nanoscale cantilevers. We can measure this noise spectrum and take the Fourier transform of it to extract the temperature.[60] As the temperature of the CdS cantilever decreases, it stiffens significantly and causes the frequency to blue-shift to higher values. We calibrated the system by monitoring the frequency of the cantilever at low laser powers to minimize the impact from heating or cooling. When the β-NaYF crystal was actively being cooled by the 1020 nm laser, a blue shift in the eigenfrequency was observed, which corresponds to an 8 °C drop in temperature of the CdS cantilever (Figure 2.4d), with the error bars originating from the standard deviation across six separate measurements. The reduced cooling is expected since we are not directly cooling the CdS nanoribbon, and the CdS is in direct contact with the large thermal mass of the silicon substrate.

While these β-NaYF crystals demonstrate optical refrigeration, the minimum achievable temperature of the β-NaYF may still be limited by the size of the crystals. The crystals could demonstrate increased cooling by matching the resonant modes of the laser inside the crystal to maximize absorption. By tuning the size of the crystal, it should be possible to maximize absorption by generating perturbed whispering gallery modes inside the crystal.[50] We have performed calculations with MIT electromagnetic equation propagation (MEEP) to calculate the enhancement of the electric field from a 1020 nm laser in β-NaYF crystals of varying radii. As the crystal radius increases, sharper increases in the electric field are seen, with enhancements of a factor of 4 near radii of 2.5 μm. Using the synthesis demonstrated here, it should

be possible to excite the perturbed whispering gallery mode and observe increased absorption and a corresponding increase in cooling capacity.

We have also calculated what laser wavelengths would be resonant with a whispering gallery mode in a hexagonal crystal with a radius of 2.5 μm to demonstrate the sensitivity of β-NaYF crystals as a cavity to varying wavelengths. The resonant wavelength for a crystal of this size was 1018 nm with a peak-to-peak distance between resonant wavelengths is approximately 35 nm. It is easy to envision an experiment where a similar crystal with a resonant frequency close to 1020 nm is chosen, and therefore, a greater cooling is achieved due to enhanced absorption of the laser.

2.2 Nucleation of Sodium Yttrium Fluoride

Classical nucleation theory (CNT), first described by Gibbs over 140 years ago, has been a robust model for describing the formation of crystals from homogeneous solution.[61] However, despite its simplicity and general validity for many crystallization processes, some proceed via so-called "nonclassical" mechanisms.[62, 63] These mechanisms include, but are not limited to, the formation of amorphous or poorly-crystalline species and the oriented aggregation and attachment of individual building blocks.[62] Broadly speaking, nonclassical crystallization is a realization of Ostwald's step rule, which suggests that systems will not necessarily take the most direct route to their most stable phase, but rather that they tend to go through a series of intermediates that are closer in free energy to the initial state.[64, 65]

The nucleation of rare earth fluorides is not well-characterized in the current scientific literature. It is known that β-NaYF can grow through mesocrystal formation of the alpha phase,[47] so an understanding of nonclassical methods is necessary to fully understand the formation of NaYF from aqueous solution precursors.

2.2.1 Nonclassical Nucleation of Solid State Materials Through Spinodal Decomposition

One such nonclassical crystallization mechanism is two-step nucleation via a dense liquid phase (DLP), typically formed through spinodal decomposition (SD).[66] In this mechanism, the highly supersaturated initial phase spontaneously separates free of a thermodynamic energy barrier[67] into ion-rich and ion-poor liquid phases, and crystals then nucleate from the ion-rich phase, often via an amorphous intermediate.[68] This mechanism has been observed directly via liquid cell transmission electron microscopy (TEM) of gold nucleation from solution[68] as well as in electrochemical reactions in nanoparticles,[69] in molecular dynamics (MD)[70] and kinetic studies of calcium carbonate,[71] in bulk chemical studies of $MgSO_4$ at high temperature,[30] by optical microscopy in crystallizable polymer solutions,[72] in MD simulations of highly supersaturated NaCl solutions,[73] and in optical microscopy and light scattering studies of protein solutions.[66] Some systems have also shown a distinct intermediate step in which the DLP condenses into an amorphous phase prior to crystallization.[74] These studies, among others, suggest that the two-step mechanism via a DLP can readily be accessed in a wide range of solution-based systems, because, when taken to sufficiently high supersaturation, nearly all solutions will reach their limit of stability.[75]

One aspect of these two-step pathways via a DLP that remains largely unexplored is that the stoichiometry of the intermediate phase is variable and ill-defined and it must evolve over the course of the reaction in order to generate the final stable phase. This is because the compositions of the ion-rich and ion-poor liquids are defined by a phase line that spans a range of compositions rather than by a set of line compounds. Therefore, for crystallization to proceed, ions must be rejected from or drawn into the solidifying regions of the ion-rich liquid. This adds a level of complexity to other previously investigated nonclassical systems, in which the intermediate phases are all

line compounds, which can either be identical for each phase, for example, as in the case of $CaCO_3$ (ignoring waters of hydration), or they can be distinct and require chemical transformation, as documented for the calcium phosphate system.[76] For the latter, charged calcium triphosphate species undergo aggregation accompanied by Ca^{2+} binding and deprotonation to create the amorphous phase, and then undergo a second step of Ca^{2+} binding and deprotonation to create the first crystalline phase. In a DLP-mediated pathway, on the other hand, ions may exchange more dynamically rather than via specific transformations to these discrete line compounds. The added complexity in these two-step pathways is further emphasized when the final compound has a ternary or more complex stoichiometry, which increases the difficulty of the required ionic reorganization. Given the common occurrence of the formation of DLPs in highly supersaturated solutions and the preponderance of ternary and more complex compounds in natural and synthetic systems, the further study of the chemical evolution of intermediate phases in these systems is therefore necessary.

2.2.2 Experimental Design Probing NaYF Nucleation

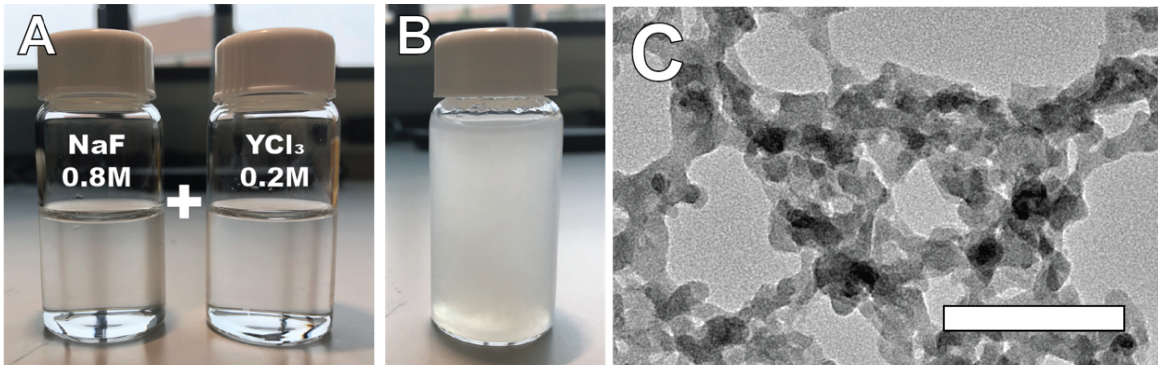

Figure 2.5: Synthesis of NaYF gel from aqueous precursors. A) Solutions of 0.8 M NaF and 0.2 M YCl_3 combine to form the gel. B) The gel product from combining precursors. C) TEM bright field image of the structure of the gel product. Scale bar = 50 nm

Here we investigate this multi-step crystal growth pathway using a model system based on ternary NaYF materials. This is an ideal system for exploring the role of chemical evolution during crystallization because the stoichiometry of NaYF materials has been shown[55] to change based on a combination of NaF and YF_3 that varies continuously with a final stoichiometry in the cubic phase of $Na_{0.5-x}Y_{0.5+x}F_{2+2x}$, or (0.5-x)NaF • (0.5+x)YF_3, with $0<x<0.5$. As x approaches zero, the stoichiometry approaches $NaYF_4$, which is used frequently as shorthand for this material. Due to the importance of the variable stoichiometry of this system, the shorthand NaYF is used instead, reserving the $NaYF_4$ notation for the hypotherical ideal stoichiometric structure. The majority of aqueous syntheses of NaYF use either microemulsion solvent systems[47] or organic capping ligands[77, 78] for the purpose of controlling both the size and shape of discrete nanocrystals[79]. In contrast to these syntheses, we synthesized ligand-free NaYF materials to provide a clear understanding of the role of solvated aqueous ion dynamics by eliminating the effects of ion chelation and surface passivation by organic species. Our results demonstrate the formation of a previously uncharacterized DLP in the NaYF system through a two-step mechanism, followed by a third step of solid-state diffusion that determines the final stoichiometry of the material. This change in stoichiometry has not previously been studied in systems that proceed by spinodal decomposition. Further investigation of this mechanism may facilitate new design of many functional materials using multi-step nucleation and growth with nonstoichiometry in the design of materials for a diverse range of applications including solid-state laser refrigeration[48], optical thermometry[80], nanoscale lasing[81], night vision[82], and electrochemical energy storage.[83]

In order to probe the nucleation and growth of NaYF materials in the absence of organic species, we first prepared aqueous electrolyte solutions of both NaF and YCl_3, and then combined them at standard conditions with relative concentrations stoichiometric to $NaYF_4$ (Figure 2.5A). Immediately upon mixing the starting solutions, we observed the apparent formation of a gel-like material (Figure 2.5B), which can be

filtered to a translucent solid. This gel remains relatively stable, but slowly condenses into a nanocrystalline white powder over the course of hours. TEM imaging of the gel shows an interconnected, porous structure (Figure 2.5C). Scanning TEM (STEM) tomography reveals not only the interconnected three-dimensional morphology but also the open-cell structure that can't be seen in conventional TEM. Brunauer-Emmett-Teller (BET) surface area measurements show a surface area of the gel phase on the order of 100 m^2/g, and powder XRD data show very broad peaks consistent with α-NaYF or a similar cubic material. Assuming the initial nucleation occurs via spinodal decomposition, we can estimate the time of separation using the Cahn-Morral equation, which is a multicomponent analogue to the Cahn-Hilliard equation describing spinodal phase separation.[67, 84] By modifying a previously-reported model to solve the Cahn-Morral equation for a simplified version of the NaYF system,[85] we were able to estimate that the initial separation should be largely complete within 250 μs. The potentials of mean force for interactions between two YF_3 molecules or a YF_3 molecule and a YF_4 ion in vacuum indicate that the dense liquid phase is likely able to form due to attractive interactions.

While the XRD data were consistent with nanocrystalline α-NaYF, the peaks were not sufficiently resolved to be able to definitively conclude that the gel is purely α-NaYF, and TEM data suggest that there are some amorphous, poorly crystalline, or otherwise disordered regions. Furthermore, significant beam-induced crystallization in the TEM indicates that the crystalline regions observed in high resolution TEM (HRTEM) may in fact have been amorphous in the as-synthesized material, therefore underestimating the distribution of amorphous and poorly crystalline regions. Using STEM-EDS, We observe a that the composition varies smoothly between Na-rich and Na-poor regions, showing a correlation of the net counts of Na and F relative to Y and Yb, suggesting variable composition along the YF_3-$NaYF_4$ spectrum. EDS spectra extracted along the path of the line scan confirm the presence of a measurable sodium peak above the noise. It should be noted that the thermodynamically stable

orthorhombic structure of YF_3 was not observed in the gel. Considering the crystal structures of the two cubic phases (NaYF and YF_3), it is notable that they share a nearly identical lattice of fluoride ions (though each unit cell of YF_3 contains an extra fluoride ion at the center). This similarity in crystal structure allows for local variations in stoichiometry without significantly affecting stability within reason, consistent with much of the literature regarding cubic $NaF \cdot YF_3$ structures grown from melt, which suggest that the bulk material can be thought of as a solid solution of NaF and YF_3.[55, 86] However, to our knowledge, this has not been thoroughly characterized on the nanoscale. Based on these findings, we hypothesize that the gel initially forms via a dense liquid phase that condenses to an amorphous solid with a composition resembling YF_3, while the excess NaF in solution slowly incorporates into the matrix to seed and stabilize cubic crystals of NaYF with initially variable composition.

2.2.3 Probing Lability of Gel Phase

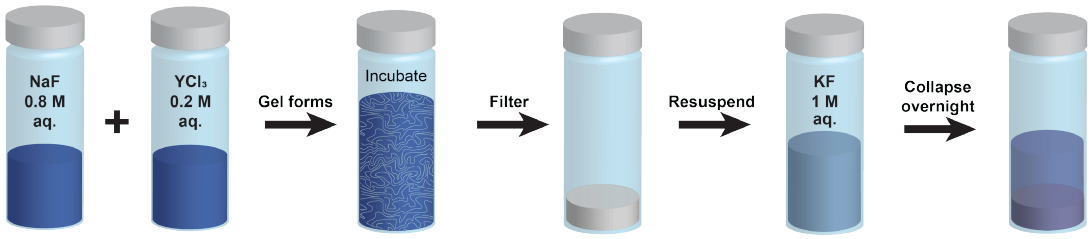

Figure 2.6: Experimental schematic for the cation replacement in the NaYF Gel. The gel was formed using a standard synthesis of NaF and YCl_3, then the reaction was arrested after a specific amount of time by vacuum filtration. The intermediate product was resuspended in a solution of KF and allowed to react to completion.

To investigate the gradual transition from YF_3 to NaYF, we attempted a cation substitution experiment on the gel using potassium cations. By removing the gel from

its native solution as shown previously, it is possible to temporarily suspend the process of monovalent sodium ion incorporation. After submerging the recovered NaYF gel in a concentrated (1M) KF solution, we observed that the remaining sodium-poor regions incorporated KF to form KY_3F_{10} (KYF) (Figure 2.6), which was distinguishable in XRD after the gel is allowed to fully collapse into single crystals. While KYF can form in multiple stoichiometries, the KY_3F_{10} stoichiometry forms in this case because it is stable in the cubic crystal phase and has the lowest potassium / yttrium ion ratio.[87] We studied this process by incubating the gel in its native solution for a set period of time (t_{inc}) before filtering and transferring it to the KF solution for long enough for it to fully crystallize (typically overnight). We could then observe how much sodium had incorporated into the gel and how much sodium-poor amorphous material remained at t_{inc}, with the amorphous sodium-poor fraction subsequently incorporating the free K^+ from the solution, and which we would later measure as a KYF peak in the XRD. As t_{inc} increases from 15 minutes to two hours, we observe that the proportion of the sodium phase increases linearly and is accompanied by a corresponding linear decrease in the relative amount of material that incorporates potassium. This shows that the incorporation of sodium into the gel occurs as the result of solid-state diffusion and is thus unambiguously a separate step from the initial formation of the yttrium-rich gel phase.

To characterize the local chemical environment of the ions without inducing crystallinity as we did with the TEM studies, we used solid-state ^{19}F nuclear magnetic resonance spectroscopy (SSNMR) to characterize the gel product compared to its eventual fully crystallized α-NaYF product as well as orthorhombic YF_3. We used orthorhombic YF_3 rather than the previously discussed cubic phase because the cubic phase is an unstable product that seems to only form in reactions similar to that reported here and, with one possible exception,[88] there are no literature reports of it being isolated without considerable incorporation of the countercation from the fluoride precursor.[89, 90]

^{19}F spin-echo magic angle spinning (MAS) NMRn shows the gel exhibits a broad resonance centered at -61 ppm with a peak width of 30 ppm. As reported by Bessada, et al.,[91] the ^{19}F chemical shift is highly sensitive to its coordination environment in molten fluoride mixtures, displaying a nonlinear and monotonic increase from -225 ppm to -28 ppm by increasing the concentration of YF_3 from 0 to 100% in the NaF-YF_3 mixture. Compared to orthorhombic YF_3, characterized by a relatively sharper peak at -58 ppm with a width of 12 ppm, and α-NaYF, which has a similarly broad resonance at -77 ppm with a width of 28 ppm, these data are again consistent with a gel that consists of some regions that are more similar to YF_3 and others that are closer to $NaYF_4$. Because the broadness of the NaYF ^{19}F spectrum can be attributed to a large distribution of isotropic chemical shifts due to the random arrangement of Na^+ and Y^{3+} around F^-,[92, 93] we show that the ^{19}F rotor-synchronized Hahn-echo spectra reduce the signals from faster-relaxing components and thereby allow for finer resolution of the remaining signal. The respective deconvolution of the resonances reveals that the gel does have some components similar to those in α-NaYF and YF_3 (-81 ppm and -69 ppm, respectively). However, the main peaks in the region that is expected to indicate YF_3 are not consistent with the major peak of orthorhombic YF_3 at 58 ppm, due to the variation in the coordination geometries of bridging fluoride ions between the cubic and orthorhombic polymorphs of YF_3 as well as amorphous regions.

This result emphasizes that the YF_3 product in the gel is not the orthorhombic phase but rather amorphous YF_3 and sodium-poor cubic NaYF. The ^{19}F spin-lattice relaxation time constant T_1 drops significantly from 19 s for α-NaYF and 9.2 s for orthorhombic YF_3 to 3.2 s for the gel, which indicates that the major fluoride species are more mobile and less ordered in the gel phase. This is consistent with our observation that there are significant amorphous, poorly crystalline, and disordered regions in the gel and also emphasizes the propensity for this gel (but not the final NaYF crystals) to undergo solid-state diffusion, as we have observed. Single-pulse ^{23}Na NMR spectra of

the gel and the α-NaYF samples both contain major resonances centered at -18 ppm and -9.5 ppm, which were assigned respectively to Na^+ sites in the bulk nanoparticles, and to Na^+ sites at the surface or near defects, as originally reported by de Queiroz, et al.[93] The fraction of the -9.5 ppm peak changes from 35% in α-NaYF to 75% in the gel sample, suggesting that the gel has over twice as many surface or defective Na^+ sites as compared to the final crystalline product, which is consistent with the high surface area present in the gel product.

2.2.4 On the Instability of the Cubic Phase of YF_3

Thus far, we have shown that this reaction proceeds via a two-step crystallization mechanism and furthermore in our ion replacement experiment that sodium incorporates into the matrix relatively slowly after the gel has formed. However, these results do not address when or how that sodium incorporation occurs, except that it is after the formation of the solid. Specifically, the sodium ions could incorporate into the dense liquid or amorphous solid phase before it crystallizes, or the gel could form a cubic YF_3 intermediate that then accepts sodium and fluoride ions (or sodium fluoride molecules) into gaps in the crystal structure. To answer this question, we turned to atomistic modeling methods. The first question to consider is whether it is even reasonable to expect a cubic YF_3 phase to form in the first place. While there are some reports of cubic YF_3 in the literature,[94, 95, 96, 88] some of those have since been disproven[89] and others may have other complicating factors such as the incorporation of additional ions. We used molecular dynamics simulations to model both cubic YF_3 and cubic $NaYF_4$. After allowing the lattice to relax for 10,000 cycles of 0.5 fs each, the cubic YF_3 lattice became highly distorted whereas the cubic $NaYF_4$ lattice remained highly ordered, indicating that cubic YF_3 is not a stable intermediate and we would not expect it to form initially. To quantify this disorder, we calculated the average root-mean-square displacement (RMSD) of each ion in each lattice. The cubic YF_3 structure showed an average RMSD of 0.435309 Å for Y^{3+}

and 0.591427 Å for F^-. This is over double the RMSD calculated for cubic $NaYF_4$ of 0.192565 Å and 0.257263 Å, respectively, and 0.216795 Å for Na^+, again indicating that the $NaYF_4$ structure is far more stable than the cubic YF_3. In fact, this analysis likely underestimates the actual stability of NaYF due to approximations made about the stoichiometry and the structure in the model that was used. To verify our methods, we performed the exact same MD analysis on the known stable structure of orthorhombic YF_3, and found RMSD values of 0.182276 Å for Y^{3+} and 0.217381 Å for F^-, comparable to the values calculated for $NaYF_4$. This again demonstrates that the cubic YF_3 would degrade within picoseconds and is thus not a stable product or intermediate. We would hypothesize that previously reported syntheses of cubic YF_3 were likely stabilized by the incorporation of what were assumed to be spectator cations. Even so, due to the existence of these literature reports and our TEM observations of sodium-poor crystalline regions, we also investigated whether the cubic YF_3 structure would be able to incorporate Na^+ ions if it could form. To do this, we performed minimum energy path (MEP) calculations using density functional theory (DFT) of ions entering the voids in a stable cubic YF_3 crystal lattice. These calculations showed large energy barriers of approximately 27 kcal/mol for sodium, 14 kcal/mol for fluoride, and 76 kcal/mol for NaF. This indicates that even if the cubic YF_3 phase was able to form as a transient intermediate, this would not a feasible mechanism for ion incorporation. Thus, we can conclude that the ions incorporate into the solid before it crystallizes, and any crystallization of YF_3 observed in TEM was indeed induced by the beam.

The multi-step crystal growth mechanism reported here is not only interesting in its own right, but it also opens the door for further applications of NaYF and similar materials that take advantage of its high surface area. For example, NaYF-gel materials could be useful for future energy storage applications,[83] and in fact we have demonstrated the successful use of this material as a reversible anode for sodium and lithium ion batteries. This may be possible due to the capability of active ion exchange

prior to crystallization. We also view this as a promising candidate for fluoride-ion batteries and will investigate further in future work.[97] This material may also have promise as an anti-reflective coating.[98] Anti-reflective coatings are a particularly interesting application because of the possibility of employing the optical refrigeration properties of NaYF to actively cool the surface.[48] In preliminary experiments, we observe optical refrigeration of the NaYF gel when doped with 10% ytterbium. We find that it can be laser cooled by approximately 0.55 °C and it does not heat under 1020 nm laser irradiation, indicating that it may be a good candidate for, for example, actively-cooled anti-reflective coatings, especially due to its lack of organic ligands on the surface, as the effective cooling efficiency of a nanocrystal is reduced by the heating of organic species on the surface.[99]

Chapter 3

LASER REFRIGERATION OF PAYLOADS & OTHER MATERIALS

3.1 Cooling of Nanodiamond Sensors on Rare Earth Fluoride Devices

Quantum sensors for nanoscale metrology is becoming evermore important for cutting edge scientific applications. Nanoscale emitters, when measured as single emitters, often have weak signals that require high levels of energy to isolate and measure, frequently through high levels of laser irradiance. This can damage the sensors or affect their sensing due to photothermal heating of the sensor, leading to a need for offsetting the heat in sensitive measurements with large excitation irradiance. Laser refrigeration is a good fit for this challenge, especially since the microcrystals grown are an appropriate size for attaching quantum sensors, such as nanodiamonds. In this chapter, we explore the properties of diamond as they relate to laser refrigeration and where laser refrigeration can be used for cooling payloads, such as quantum sensors.

3.1.1 Introduction to Nanodiamond Thermometry

The long (millisecond) spin coherence lifetime[100] and all-optical spin readout of the negatively-charged nitrogen vacancy (NV^-) point defect in diamond have enabled a wide range of applications including, quantum computation[101], quantum communication[102], and nanoscale quantum sensing of temperature[103], pressure[104, 105, 106, 107], and electromagnetic fields[108] based on optically detected magnetic resonance (ODMR). Optical levitation of nanodiamonds offers the additional advantage of extreme isolation, which is conducive to achieving mechanical oscillations with ultra-high quality factors and longer spin coherence times for potential applications

such as detectors in advanced cosmological observatories that study areas such as dark matter,[109] quantum gravity,[110] and gravitational waves.[111]

However, many applications of the NV^- center are limited by thermal drift of the NV^- center's zero phonon line (ZPL) due to photothermal heating. In particular, nanodiamonds frequently contain point defects including substitutional nitrogen (P1) centers and nitrogen vacancy centers (both neutral and negatively charged) that increase the background absorption of excitation lasers causing photothermal heating. To date, many applications involving NV^- centers have been limited by the photothermally-induced spectral wandering of the NV^- center's optical transitions. Photothermal heating can also lead to unintended ejection, graphitization, or burning of nanodiamonds within an optical trap.[112] The absence of conductive and convective pathways for removing excess heat from the optically-trapped particle *in vacuo* magnifies the effect of photothermal heating.

Laser refrigeration presents a unique solution to the photothermal heating of diamonds by enabling rapid (ms) optical temperature control of nanodiamond quantum sensors in both atmospheric and vacuum conditions. Solid state laser cooling is based on using a laser with low optical entropy to excite crystal field levels within Yb^{3+} ions within a fluoride host crystal.[57] The laser excitation is followed by the efficient emission of blue-shifted (anti-Stokes) photons with high optical entropy.[48] Recent advances have been made with solid-state laser cooling materials, such as cooling to sub-cryogenic temperatures[36], the development of laser cooled optical fibers[113], and the development of laser cooled spherical ceramic nanocrystals that have been levitated in vacuum in an optical trap.[114] However, there are no reports demonstrating the indirect laser cooling of quantum sensors, includng the NV^- center in nanodiamonds.

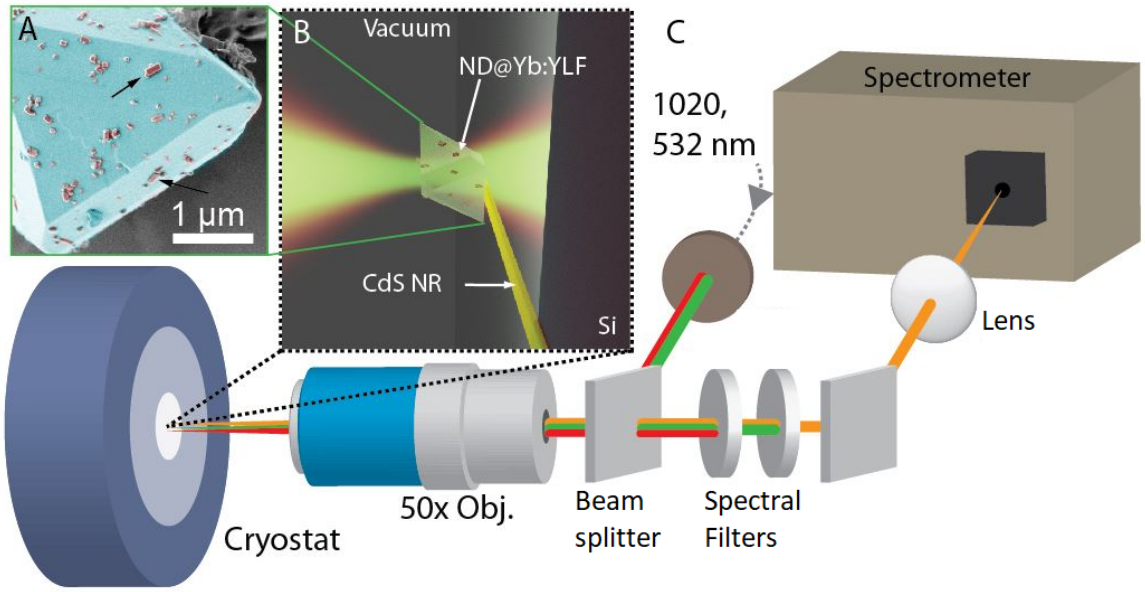

Figure 3.1: Experimental setup for nanodiamond sensor thermometry. A) SEM of a representative Yb:$LiYF_4$ crystal (blue) with NDs (red) dropcast on it (false colored for illustrative purposes). B) An illustration of the cadmium sulfide nanoribbon (CdS NR) cantilever device suspended in vacuum using a silicon substrate. C) A schematic of the photoluminescence measurement setup.

Experimental Design for Cooling of Nanodiamonds

To verify if nanodiamonds could be cooled by indirect laser refrigeration, nanodiamonds (NDs) containing NV^- centers are attached to ceramic microcrystals including 10% ytterbium doped YLF and β-NaYF by van der Waals bonding (Fig. 3.1A). NDs were coated onto the Yb:$LiYF_4$ crystal with a number density of $\sim 3.7 \pm 1$ μm^{-2}. The cooling microcrystals with NDs were placed at the end of a single-crystalline CdS nanoribbon cantilever that was suspended off of the edge of a silicon substrate (Fig. 3.1B). The small contact and cross-sectional area of the cantilever minimizes the losses through heat conduction from the microcrystal. The CdS nanoribbon is $\sim$110 nm thick in the direction of light propagation, and is optically transparent at 1020 nm (and partially transparent at 532 nm) which minimizes any additional heating due to

its low absorption coefficient ($\alpha_{1020nm} = 6.7 \times 10^{-13}$ cm^{-1}, α_{532nm}=1362 cm^{-1}).

The NaYF used was made through the synthesis described in chapter 2 according to [78]. The YLF nanocrystals was performed following modifications to Roder *et al.*[5] discussed here: 0.585 g (2 mmol) of EDTA and 0.168 g (4 mmol) $LiOH{\cdot}H_2O$ were dissolved in 10 mL Millipore DI water and heated to approximately 80 °C while stirring. After the EDTA was dissolved, 1.8 mL of 1.0 M YCl_3 and 0.2 mL of 1.0 M $YbCl_3$ were added and continually stirred for 1 hour. This mixture is denoted as solution A. Subsequently, 0.105 g (4 mmol) of LiF and 0.34 g (8 mmol) of NH_4HF_2 were separately dissolved in 5 mL Millipore DI water and heated to approximately 70 °C while stirring for 1 h. This solution is denoted as solution B. After stirring, solution B was then added dropwise into solution A while stirring to form a homogeneous white suspension. After 30 minutes, the combined mixture was then transferred to a 23 mL Teflon-lined autoclave and heated to 180 °C for 72 h in an oven. After the autoclave cooled naturally to room temperature, the YLF particles were sonicated and centrifuged at 4000 rpm with ethanol and Millipore DI water three times. The final white powder was then dried at 60 °C for 12 hours followed by calcination at 300 °C for 2 hours inside a quartz tube.

In the NV^- generation process, nitrogen initially enters the diamond lattice as a substitutional impurity during ion implantation (usually $\leq$ 200 ppm). Subsequent radiation damage induced by a variety of sources such as a beam of high-energy neutrons, electrons, or ions is used to create vacancies.[115] Annealing of the irradiated diamond at T $\geq$ 850 °C causes thermal diffusion of the vacancies. This results in the appearance of the NV^- centers.[115] However, not all the nitrogen atoms are converted to the NV^- centers, inducing a variety of undesirable defects.

In addition to the photothermal heat generated from the broad phonon overtones of NV^- centers, other surface or lattice defects within NDs may contribute to photothermal heating. To evaluate their presence, both electron paramagnetic resonance (EPR) and infrared photothermal heterodyne imaging (IR-PHI)[116, 117] were used

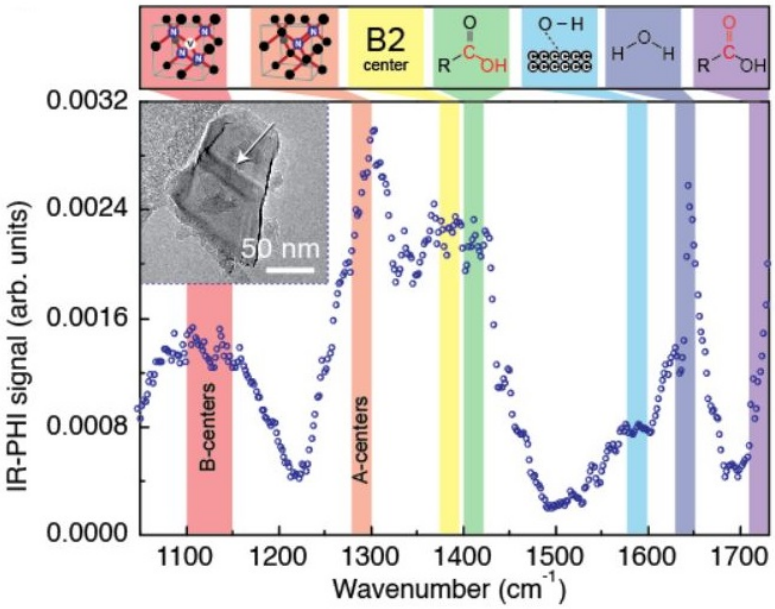

Figure 3.2: Nanodiamond compositional data. IR-PHI spectrum of a single nanodiamond sample. The peak assignments at wavenumbers (cm^{-1}) are 1100-1150: B-centers, 1280-1300: A-centers, 1380: B2 aggregates or C-H bond, 1415: carboxylic acid C-O-H stretch, 1590-1600: hydroxyl (O-H) on the surface, 1640: inclusions of water or water residue, 1730: carboxylic acid C=O stretch. Inset shows a TEM bright-field image of an individual ND used in the shown IR-PHI measurements.

to make measurements on ensemble and single ND particles, respectively. The EPR spectrum of an ensemble of ND showed a strong central line consisting of the sum of two derivative Lorentzian line shapes is due to surface and other paramagnetic defects.[118] There were very weak outer lines (green arrows) due to the P1 centers in the ND particles.[119] The weakness of these lines is due to the low concentration of P1 and the possible saturation of the signal. The NDs have <40 ppm of substitutional nitrogen (based on the manufacturer's specifications) which may also contribute to background photothermal heating.

Defects in nanodiamond also are observable using IR-PHI spectroscopy. IR-PHI enables infrared spectra with visible-region diffraction limits to be collected from

single ND particles.[120] A representative IR-PHI spectrum is shown in Fig. 3.2 with the inset showing a TEM image of an isolated ND particle used in these measurements. The IR-PHI spectrum shows evidence of sizable concentrations of defects and also absorption features from organic functional groups which passivate the ND surfaces. In particular, the regions highlighted in red (1100-1150 cm^{-1}) and orange (1280-1300 cm^{-1}) in Fig. 3.2, show evidence for the presence of a significant amount of complex substitutional nitrogen point defects in the form of B-centers and A-centers, respectively. In addition, the presence of non-zero IR-PHI signal in the range of 1380 cm^{-1} (yellow) may be due to the presence of B2-aggregates. These are complex objects in (100) planes that can range from a few nanometers to micrometers in size and are formed by carbon and nitrogen interstitials.[121] The presence of linear fringes across the center of the ND in the TEM image shown in the inset of Fig. 3.2 (white arrow) may also be the evidence of these defect centers. It remains unclear which defect species contribute most to photothermal heating.

3.1.2 Cooling of YLF Microcrystals with Nanodiamonds Attached to the Surface

The fluoride crystals were cooled through the efficient emission of upconverted infrared photons[122] excited by a focused 1020 nm laser beam (Fig. 3.1C). An all-optical Debye-Waller factor (DWF) thermometry[123] approach was used to measure the temperature of irradiated ND quantum sensors during laser cooling experiments. DWF thermometry is based on calibrating the ratio of the nanodiamond's ZPL emission relative to the adjacent phonon side bands ($I_{ZPL}/I_{overtone}$). In Fig. 3.3A, the black line shows the composite spectrum from the sample when both the 532 and 1020 nm beams were incident. Given that the NV^- emission spectrum was crucial in obtaining the temperature of the NDs using the DWF technique, it was necessary to subtract the background $^4F_{9/2}$ emission from the Er^{3+} impurities (dotted purple line) that overlaps with the emission of the NV^- center. This emission from Er^{3+} was subtracted from the composite spectrum (black line) at the respective intensity

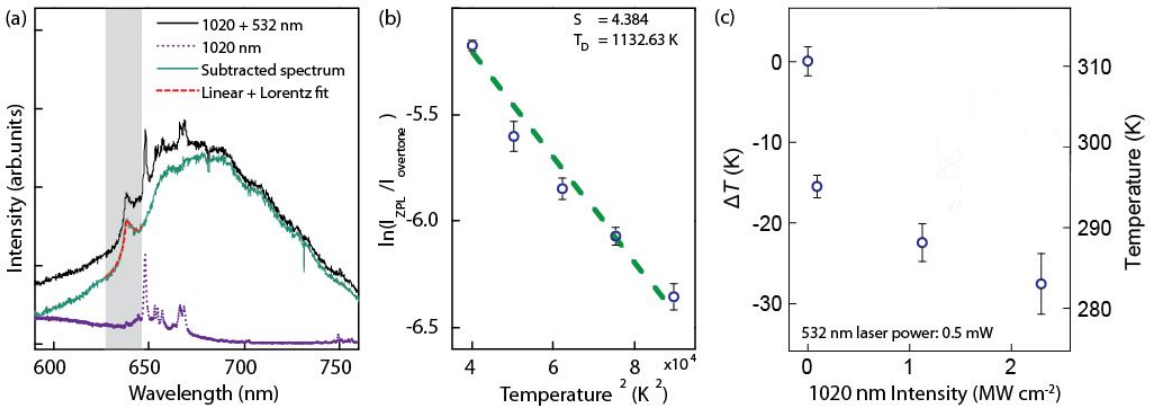

Figure 3.3: A) The composite PL spectrum, when both 1020 and 532 nm lasers are on, is shown in black. The contribution from the upconverted $^4F_{9/2}$ emission from Er^{3+} impurity ions is shown using a dotted purple line. The subtracted spectrum and the fitting function are shown using a green and dashed red line. B) The natural log of the DWF is plotted versus the temperature squared. A linear fit (dashed green line) to the data is used to extract T_D and S. C) The corresponding calibrated temperatures obtained from the measured value of $\ln(I_{ZPL}/I_{overtone})$ from the processed spectra are plotted for various laser intensities of 1020 nm while the 532 nm laser is kept consistently at an intensity of 0.073 MW cm^{-2}.

of the 1020 nm laser used to obtain the emission profile from the NV^- centers (green line). This prevents convolution of the Er^{3+} and NV^- emission, allowing for accurate calibrations and measurements of the temperature.

The ZPL was fit using a function consisting of a linear background and a Lorentzian around the ZPL (dashed red line) and the integrated intensity of the ZPL peak (I_{ZPL}), centered at 637 nm, was obtained from the amplitude of the Lorentzian component. The emission intensity from the phonon side bands ($I_{overtone}$) was obtained by subtracting the ZPL area from the integrated area of the spectrum. As the temperature of the cryostat was changed from 200-300 K, the DWF was calculated and plotted against temperature squared (Fig. 3.3B). The data points were fit to the calibration function (dashed green line) discussed in [123] to obtain the Debye temperature (T_D=1132.6 K) and the electron-phonon coupling parameter (S=4.38). These values

were used as a calibration for subsequent measurements. Fig. 3.3C shows the calibrated temperature of the NDs at various 1020 nm laser intensity, where a continuous wave (CW) 532 nm laser at an intensity of 0.073 MW cm^{-2} was used as a probe beam to excite the NV^- centers. As the 1020 nm laser intensity was increased, an immediate drop in temperature and subsequent saturation trend was observed. A maximum temperature change of 27.7($\pm$3.8) K measured at 2.12 MW cm^{-2} of 1020 nm laser intensity using DWF thermometry agrees well with the temperature change of the YLF microcrystal. Therefore, the cooling power generated by YLF microcrystal in vacuum allowed net cooling of the attached NDs by 27.7($\pm$3.8) K.

Indirect Cooling of Nanodiamonds Via Laser Refrigeration

The photothermal heating of NDs from the 532 nm probe laser was measured to be 25.6 mK·μW^{-1} at zero 1020 nm intensity. Heating from the probe laser can be reduced by using low probe laser intensities on the order of 10 KW cm^{-2} along with sensitive detectors. As the intensity is increased, the cooling induced blue-shift of the ZPL peak is observed from their respective fits. Tuning the 1020 nm intensity allows for the stabilization of thermally-induced spectral wandering of the NV^- center's ZPL. A feedback loop can therefore be established so that the red-shifts in ZPL due to heating can be sensed optically and counteracted by increasing the intensity of the cooling laser. The ND temperature may be adjusted orders of magnitude faster than a large cryostat's temperature considering the micro-to-millisecond timescales taken by the microcrystal to reach steady state temperatures.

Alternatively, the cooling of NDs can also be measured using ODMR[103] which does not require the subtraction of unwanted background emission from Er^{3+} ions. A hexagonal, oblate microcrystal of Yb:NaYF grown via hydrothermal synthesis[78] was used to make a device analogous to the device discussed above for DWF thermometry. A frequency-doubled Nd:YAG laser (532 nm, 370 μW) was used for exciting the NV^- centers. The sample was also illuminated from the bottom by a collimated

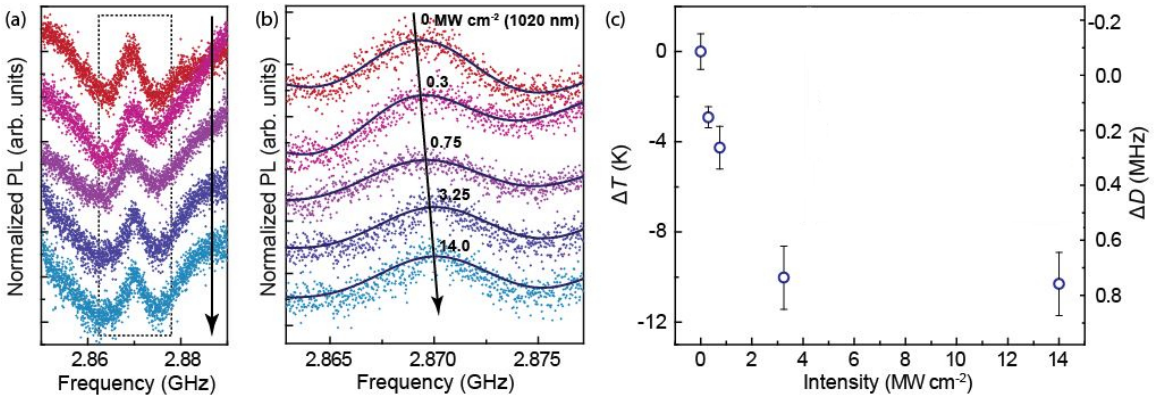

Figure 3.4: A) Full frequency range of ODMR measurements with two resonance dips; at 1020 nm intensities of 0, 0.3, 0.75, 3.25, and 14 MW cm^{-2}, increasing in the direction of the black arrow. B) Variation of the zero-field splitting parameter D as a function of the cooling laser intensity. The ODMR signals, zoomed around 2.87 GHz, show a blue-shift in D revealing the cooling of crystal with increased 1020 nm laser intensity. C) Blue-shift in the splitting parameter D (right y-axis) and the corresponding reductions in the crystal's temperature (left y-axis) versus the intensity of cooling laser.

while light beam and the back-scattered light was collected to locate and monitor the position of the sample. Microwaves (30 dBm) were applied on the sample using a loop antenna which delivered a sequence of 100 ms alternative on/off microwave (MW) pulses (500 repetitions per location) to control the electron spin of NV^- centers, and the frequency of the MWs was scanned over 2.85-2.89 GHz to perform ODMR measurements. Ambient pressure ODMR spectra of the electron spins in NV^- centers in nanodiamonds were used to measure the temperature of the NDs. The readout of NV^- spin systems is readily accessible by visible lasers and MW radiation. Fig. 3.4A shows the ODMR spectra for low to high intensities (in the direction of the arrow) of the 1020 nm cooling laser. Fig. 3.4B shows the ODMR spectra zoomed around the center frequency and the respective fits are shown using blue lines. As the laser intensity is increased, a blue-shift in the zero-field splitting parameter (D) is observed in these spectra, indicating a reduction in the internal temperature of the

crystal.[103] The net shifts of calibrated temperature measured (using the net shift in the splitting parameter) at these intensities are shown in Fig. 3.4C. The corresponding increase in the splitting parameter is also shown in the right y-axis of Fig. 3.4C. The splitting parameter increases as the laser intensity increases from 0 to 3.25 MWcm^{-2}, corresponding to ∼10 K cooling in the crystal based on previous reports[103] of the temperature dependence of the zero-field splitting parameter (dD/dT = -74.2 kHz K^{-1}). The smaller temperature change compared to the measurements with YLF in vacuum is attributed to the different cooling crystal used (NaYF) and the presence of conductive heat transfer at ambient conditions. However, the cooling saturates by further increasing the laser intensity, where the heating due to background absorption counteracts anti-Stokes cooling. The ODMR-based temperature measurements are also consistent with recent reports[124] that fit the NV$^-$ centers' PL spectra around the ZPL. Fitting the ZPL spectra of the NV$^-$ centers with and without 3.25 MWcm^{-2} cooling laser irradiation on the crystal also indicates cooling. The calculated change in temperature agrees with the 10 K cooling found in the ODMR measurements.

3.2 Reduction of Photothermal Heating Directly in Diamond

The cooling of nanodiamond via contact with rare earth fluorides is a significant advance in offsetting heat in nanoscale sensors. However, it would be ideal if it were possible to directly cool the nanodiamond through laser refrigeration. Rare earth fluorides are a well-studied class of materials for laser refrigeration, but there is nothing fundamentally specific to them that allows for laser refrigeration as opposed to other materials. Any material that undergoes anti-Stokes luminescence with a sufficiently high external quantum efficiency can use laser refrigeration to cool. Some diamond defects are known to have very high quantum efficiency, but controlling the defects in diamond is challenging. If it were possible to control the defects in diamond and use careful anti-Stokes excitation, it may be possible to reduce photothermal heating or even induce cooling directly in diamond.

3.2.1 Photothermal Heating in Diamond Defects

Photothermal heating in nanodiamond materials[125] has created challenges for quantum sensing measurements based on optically detected magnetic resonance,[126, 127] including scenarios when nanodiamonds are optically trapped in high vacuum conditions where offsetting heat is difficult.[128] Recently, progress has been made in reducing photothermal heating in diamond materials grown via high-purity chemical vapor deposition (CVD);[129] however, CVD methods are difficult to apply to diamonds grown at high-pressure, high-temperature (HPHT) conditions. Currently, there is significant interest in developing solid-state laser refrigeration[130] materials that can mitigate detrimental photothermal heating for future applications in cavity optomechanics,[26, 131] biophysics,[5, 132] and quantum information science and technology.[133, 26] In addition to band-to-band transitions and Auger emission from semiconductors,[134] dipole transitions from point defects in semiconductors, including both the NV^- center[132] and the nitrogen–vacancy–nitrogen (H3) center[133] in diamond, have been proposed recently as potential candidates for solid-state laser cooling. However, to date, the experimental demonstration of solid-state laser cooling of semiconductors remains a longstanding experimental challenge.[134, 135, 136]

The H3 center in diamond exhibits several promising characteristics[137, 138] for laser cooling applications including a neutral charge state, a high radiative quantum yield ∼95%,[139] a long excited-state lifetime (∼17 ns), and efficient anti-Stokes photoluminescence[140] that make it a potential candidate for demonstrating solid-state laser cooling of diamond. The H3 center consists of a nitrogen–vacancy–nitrogen (NVN) complex with C_{2v} rotational symmetry along (111) zone axes within diamond's face centered cubic Bravais lattice [Fig. 1(e)]. Its characteristic emission features consist of a prominent ZPL at 503 nm with the corresponding wide phonon sidebands (PSBs) red-shifted from the ZPL. Its photostability and high quantum efficiency have also been used to report tunable laser action in the visible spectral region between 500

and 600 nm.[139] Here, we demonstrate both efficient anti-Stokes emission from the H3 center and also reduced photothermal heating in macroscopic HPHT diamonds that have been enriched with H3 centers relative to control samples containing NV centers. If the NV and P1 centers within diamond crystals could be reduced, the lowered background absorption will lead to reduced photothermal heating in the diamond crystal.

3.2.2 Bulk Diamond Thermometry

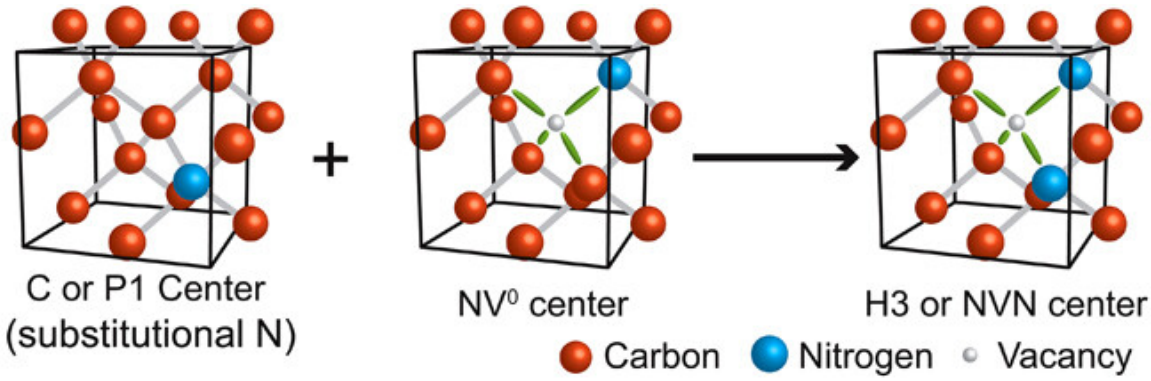

Figure 3.5: A schematic showing the mobilization of NV and integration of substitutional nitrogen (C-centers or P1 centers) with NV^0 centers at high pressures and temperatures to form NVN or H3 centers.

The experimental optical setup designed to collect the emission from macroscopic diamond crystals excited locally to investigate the photothermal properties of the H3 center was based on the optical setup described earlier in this chapter. Two diamond samples were studied, one enriched with H3 centers using the technique reported by Rand et al.[139] and the other grown with a high concentration of NV centers. The mechanism with which the H3 centers are formed in a diamond is shown in Fig. 3.5. The H3 diamond was treated at high-pressure and high-temperature conditions[139] under which the neutral nitrogen vacancy (NV^0) centers become mobile and form the H3 center through recombination with P1 defects.[141]

The H3 diamond sample was hexagonal-shaped and predominantly contained point defects in the form of H3-centers (NVN-centers). It was yellow-green colored around the center of the crystal, while the areas away from the center had a red/purple hue. The area with the red/purple hue was observed to have a higher proportion of NV^0 and NV^- centers. For these experiments, the central area, which has a high proportion of H3 center to other defects, was used. The second sample (the NV sample) was triangular-shaped and had a bright red/purple hue overall due to a high concentration of NV centers. The samples were fixed to a Janis ST 500 cryostat's stage using a double-side copper tape. The focal spot of the lasers was maintained $\sim$10 μm below the top surface of the diamonds, and the focal volume heated and probed using the lasers was approximated to be less than 100 μm^3 Given the large absorption coefficient and thickness of the diamond compared to the laser spot size, the divergent beam reaching the lower part of the diamond substrate had a low irradiance, which resulted in negligible photothermal heating of the copper tape due to the laser.

3.2.3 Analysis of Diamond Luminescence

The Stokes part of the emission spectra was collected from the H3 and NV diamonds under laser excitation of 532 nm excitation as shown in black and red in Fig. 3.6a, respectively. The emission wavelength of NV^0 and NV^- ZPLs are marked using yellow and red dashed lines centered at 575 and 638 nm, respectively. The counts are normalized using the laser power used and the acquisition time. The integrated emission intensity from NV^- centers from the NV diamond sample was measured to be 11 times higher relative to NV^- emission from the H3 diamond. This more intense NV emission indicates a higher concentration of NV centers present within the NV diamond in comparison with the H3 sample.

The anti-Stokes part of emission spectra collected from the H3 and NV diamonds using a 532 nm excitation is shown in black and red in Fig. 3.6b, respectively. Strong anti-Stokes emission from H3 centers is observed in the H3 diamond, while it is absent

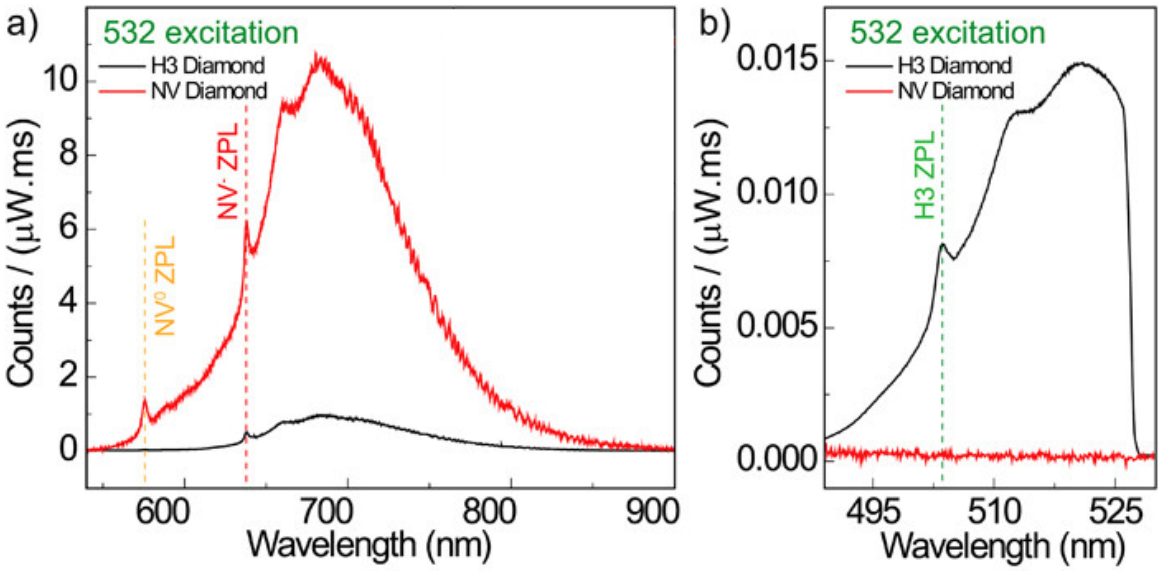

Figure 3.6: Stokes and anti-Stokes photoluminecence of Diamond Samples with 532 nm laser. a) Normalized room temperature spectra of NV^0 and NV^- emission from both H3 (black) and NV (red) samples using a 1 mW 532 nm laser excitation spot. b) The anti-Stokes wavelength band spectra for both the H3 (black) and NV (red) samples using 532 nm excitation.

in the NV diamond. Green dashed line shows the H3 ZPL center wavelength at 503 nm with the red-shifted wide Gaussian phonon sidebands. The presence of anti-Stokes fluorescence is important for realizing solid-state laser refrigeration and motivates conducting experiments in the future to evaluate the efficiency of this process at different excitation wavelengths. The spectra were cut off at 527 nm due to the notch filter used to remove the scattered 532 nm laser.

The Stokes part of emission spectra from the H3 and NV diamond spots measured using a focused 445 nm laser excitation is shown in Fig. 3.7a for both H3 (black) and NV (red) samples, respectively. Emission from the H3 diamond predominantly consists of emission from the H3 ZPL at 503 nm and a broad phonon overtone emission with a center around 530 nm, representing a relatively high concentration of H3 centers in the sample. The instrument-induced intensity variation with wavelength was

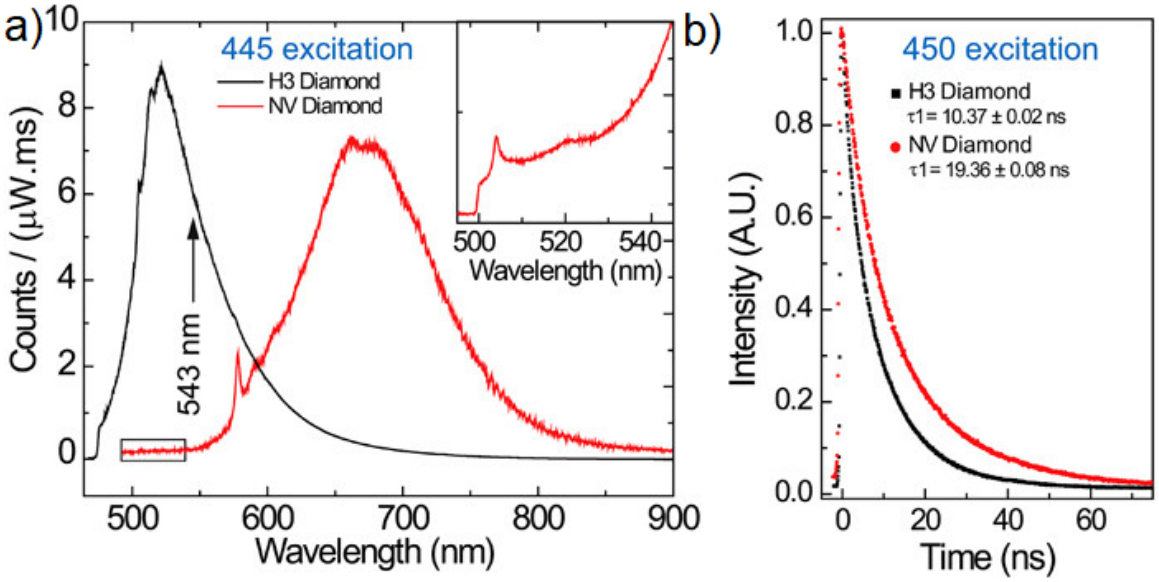

Figure 3.7: Stokes Emission and Lifetime Induced by 445 nm Laser. a) Normalized room temperature full-range spectra using a 445 nm laser excitation spot. The inset shows a zoom-in view of the H3 center signal in the NV diamond sample. b) Measured and exponential fitted lifetime data for H3 sample (black) and NV sample (red) with a 450 nm excitation.

corrected using a calibrated halogen lamp to obtain the mean wavelength. A Jacobian transformation was applied following Mooney et al.[142] to convert the intensity vs wavelength data into intensity vs energy. The frequency centroid was calculated to obtain the mean emission energy ($\bar{E} = h\bar{\nu}$) of 2.28 eV. This mean emission frequency corresponds to the mean wavelength ($\bar{\lambda} = c/\bar{\nu}$) of 543.71 nm. A 475 nm long-pass filter was used to block the laser signal from entering the spectrometer, which resulted in a cut-off in the emission signal from the H3 diamond sample. Statistical fitting was performed to extrapolate the signal on the blue side of 475 nm. This is important for laser refrigeration applications as only wavelengths red-shifted to this wavelength can be used to observe the net cooling of diamonds through H3 centers doped in them.

While Fig. 3.7a shows no NV emission from the H3 diamond when the pump laser was focused tightly within an area with a low NV concentration, emissions from NV

centers are observed when the entire crystal is optically excited. Photoluminescence excitation (PLE) spectra of the H3 diamond were collected at 530 and 680 nm, which are the emission wavelengths with the highest intensity of the phonon sidebands of the H3 and NV centers, respectively. The PLE spectra confirm the presence of NV centers in the H3 diamond, as well as other point defects that likely contribute to background absorption. Two-photon absorption can also contribute to the emission from H3 diamond. However, it has been predicted to be quite weak as shown by Lin et al.[137] and will have a different power dependency compared to the anti-Stokes emission.

As can be seen in Fig. 3.7a, for an excitation wavelength of 445 nm, the emission from the NV diamond predominantly consists of the NV^0 ZPL at 575 nm and a broad phonon overtone centered around 680 nm. The weak NV^- ZPL emission at 638 nm is due to the strong photo-ionization of NV^- centers to NV^0 using the 445 nm laser. The emission from the NV sample primarily occurred due to the NV centers where a large fraction of the emission intensity ($\sim$36.3%) was contributed by NV^0, indicating an efficient ionization of NV^- due to the high energy of the incident laser (445 nm). A very small amount of emission intensity in the NV diamond was from the H3 center due to the very low concentration of the H3 centers in this sample. This is indicated using a gray box and the close-up is shown as an inset in Fig. 3.7a.

Lifetime measurements using a pulsed 450 nm excitation laser were conducted on the H3 diamond with detection window centers both at 530 nm (maximum of H3 center phonon overtone emission) and 680 nm (maximum of NV^- center phonon overtones) as shown in Fig. 3.7b. Double exponential fitting to the 530 nm band decay spectrum shows 10.37 and 2.41 ns decay components. The time scales are smaller than the intrinsic H3 lifetimes of $\sim$16.7 ns.[143] The short decay time component (2.41 ns) can be attributed to the heavy quenching of H3 luminescence by other luminescent defects. Since an H3 center is created from an A-aggregate plus a vacancy, or NV centers and P1 centers, spatial correlations are likely between the H3 centers and the

A-aggregates, or NV centers.[144] The A-aggregates act as quenching centers, decreasing the lifetime of H3 ensembles in closer proximity to them.[144] No NV^- or NV^0 luminescence could be observed at the center of the H3 diamond, where the lifetime measurements were performed. However, NV^- luminescence could be observed when the 450 nm laser was focused near the edge of the H3 diamond. The NV^- emission from this region shows a rise and a decay component with time scales of 5.8 and 16.9 ns, corresponding to the excitation of the NV centers from the trapped H3 emission (similar to re-absorption and photon recycling effects in perovskite materials)[145] and the intrinsic NV^- center lifetime, respectively. The lifetime of emission from the 680 ± 10 nm phonon overtone from the NV diamond sample was fit to a double exponential with decay times of 19.36 and 7.4 ns. The 19.36 ns lifetime is much longer than the intrinsic lifetime of the NV^- center (12–13.5 ns)[146, 147] but close to the 21 ns intrinsic lifetime of the NV^0 center. The high emission percentage from the NV^0 in the NV diamond sample's spectrum due to blue light excitation as seen in Fig. 3.7a may contribute to these long time scales.

The room temperature emission spectra of the NV diamond sample were measured at six different laser irradiances and shown in Fig. 3.8. The measured counts normalized using the laser power and acquisition times are shown on the y axis with units of counts/(μW ms). The vertical green dotted line signifies an arbitrary separation of the emission spectra such that the left and right sides indicated using red and black lines represent the wavelength ranges in which the predominant amount of emission originates from the NV^0 center and NV^-, respectively. However, since the phonon overtones from the NV^0 are convoluted with the NV^-, a more sophisticated technique is required to measure the percentage of emission from the NV^0 as compared to the total emission. To calculate this, the NV^0 and NV^- ZPLs and the overtones were fit to Lorentzian peaks. The sum of amplitudes of the L_2 and G_6 - G_9 fit the normalized spectra gave the emission from the NV^0 centers. The sum of amplitudes from fits of all the other peaks contributes to the emission from the NV^- centers. The percentage

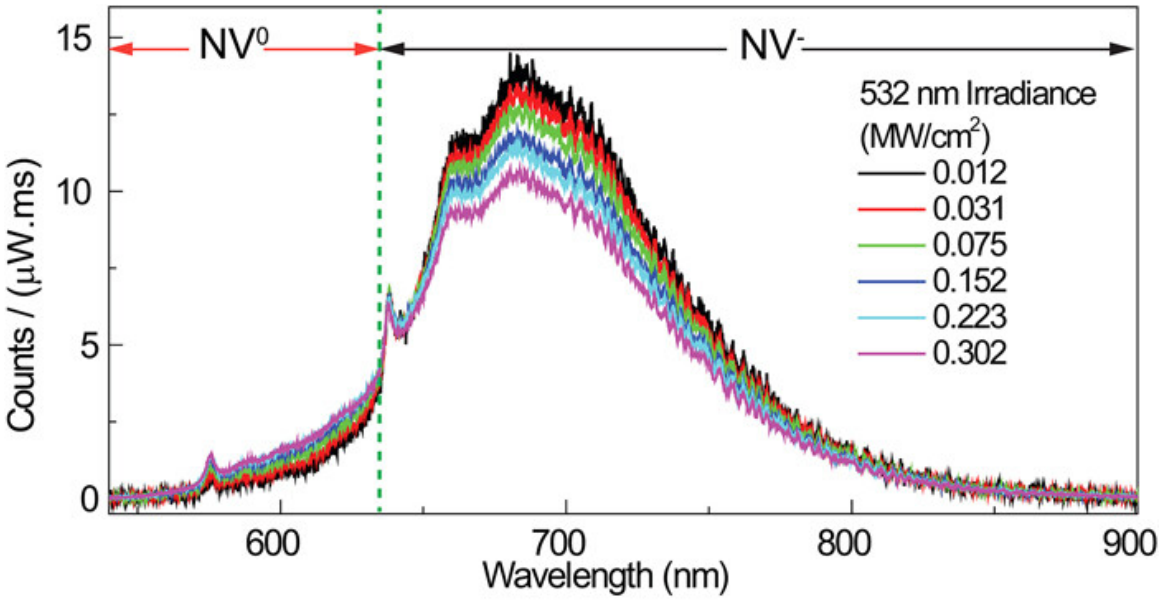

Figure 3.8: Shifts in NV^- concentration as a function of 532 nm laser power. Room temperature normalized emission spectra from the NV diamond sample at six different 532 nm irradiances.

of the respective charge state emission from NV^- and NV^0 was calculated. At higher irradiances, NV^- is dynamically ionized to NV^0 (and back) at a faster rate,[148] causing the relative percentage of emission from NV^0 to rise from 12 to 18% as the laser power increases from 81 to 2050 μW. The decrease in dynamic population of the NV^- suggests that the absorption by NV^- would progressively become smaller at higher irradiances as shown by Subedi et al.[149]

3.2.4 Reduced Photothermal Heating in H3-Rich Diamonds

To calculate the DWF, the area under the ZPL (I_1) was obtained by fitting the spectrum in a narrow wavelength range of around the 638 nm using a composite function consisting of a linear background and a Lorentzian. The amplitude of the Lorentzian is I_1. The area under the PSBs (I_2) can be obtained by integrating over the spectrum and subtracting the previously determined ZPL area from it. The DWF is calculated

by taking the ratio I_1 to I_2. The change in DWF with temperature has been reported by Plakhotnik et al.[150] Accurate temperature measurements using ODMR required precise detection of frequency shifts of at least 1.3 MHz for the NV diamond sample and 200 kHz for the H3 diamond sample.[151] Due to high sample strain and other paramagnetic defects, linewidths of the dips obtained in the ODMR signal from both the samples were not sharp enough to precisely measure the temperature changes. Therefore, DWF was chosen over ODMR as the thermometry technique. Moreover, using the DWF thermometry, one can avoid the need for microwave equipment in future laser cooling experiments.

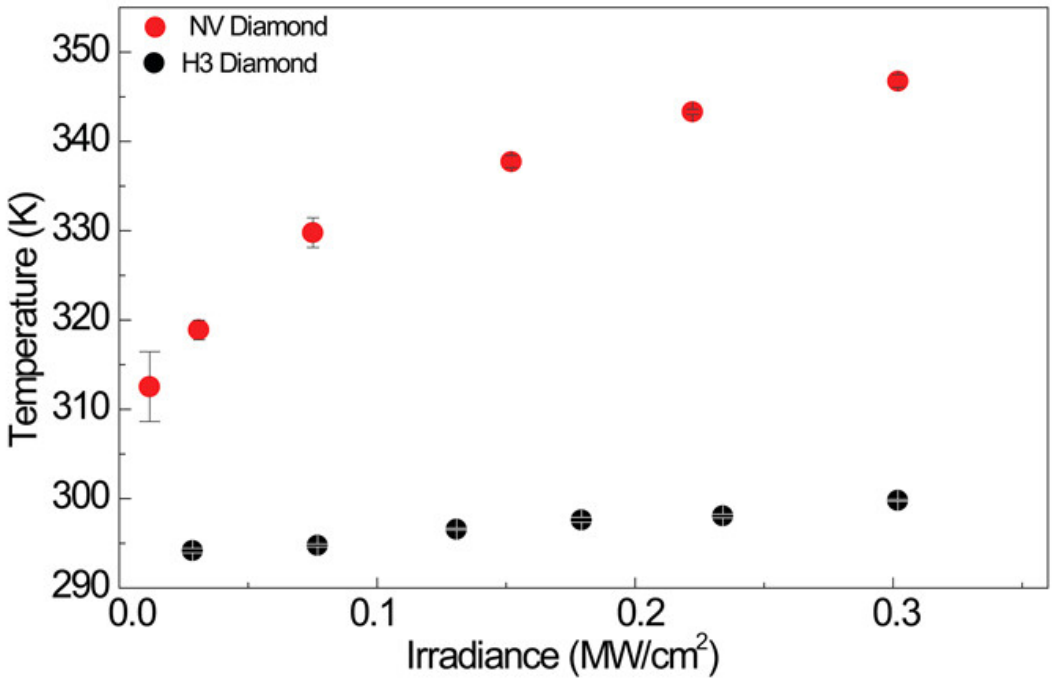

Figure 3.9: Irradiance dependent calibrated temperatures for the H3 (black circles) and NV (red circles) diamond samples.

The temperature-dependent measurement of the DWF for the H3 diamond was done using a laser irradiance of 12 kW/cm^2 at a wavelength of 532 nm. A fit to the DWF equation gives the Debye temperature $T_D = 1133.7$ K and the electron–phonon

coupling parameter S = 3.41. The same measurement was repeated on the NV diamond. The fit to the DWF equation gives T_D = 1164.3 K and S = 3.46. These values were used to calibrate the laser irradiance-dependent measurements to obtain the change in temperature as shown in Fig. 3.9. The calibrations were validated by comparing the calibrations curves of various laser power levels. The slopes of each curve were compared for any nonlinearity or deviation based on the power level. No such deviation was observed, suggesting that the calibrations done are valid for all laser powers used in this experiment. The overall temperature change near the laser spot in the H3 diamond is close to 5 K at the highest irradiance. However, at the same laser irradiance, the NV diamond heats to temperatures 50 K higher than room temperature. Note that the NV diamond sample does not heat linearly with the increase in laser irradiance, as one would expect for materials with a constant absorption coefficient at a particular wavelength. As the excitation laser irradiance is increased, it is likely that the absorption coefficient decreases due to a decrease in the population of the NV^-, shown previously.

Similarly, the 10-fold decrease in photothermal heating of the H3 diamond can be attributed to the significantly smaller amount of NV centers in the sample as discussed above. This is encouraging for further exploration of methods to convert NV centers to H3 centers in a diamond sample. The ability to maintain a relatively high stable population of H3 centers in a sample may result in minimized heating which is advantageous considering its possible applications as a lasing medium. Additionally, the presence of anti-Stokes emission from the H3 center motivates its further exploration as a laser refrigeration color center for radiation-balanced lasers.

As noted above, H3 centers can be formed by heating samples with NV centers at temperatures high enough to enable their diffusion. The NV dissociation energy is higher than the migration energy, so NVs diffuse as a complex, limited by the nearly equal barriers (4.8–4.85 eV) calculated for nitrogen/vacancy exchange and realignment via the vacancy moving away to 3rd nearest neighbor distance and returning

along a different path.[141] In order to optimize this process for laser cooling, it is critical that nearly all NV centers are transformed to H3 centers via binding with P1 centers. This can be achieved by using long-time, high-temperature anneals in systems with high substitutional N concentrations.

Both theory[141, 152] and experiment[153, 154] indicate that temperatures above about 1500 °C are required to activate NV diffusion. Extrapolating the hopping rate calculated by Chakravarthi et al.[154] (which closely aligns with the theoretical value) combined with a diffusion-limited reaction rate and moderate range capture distance (∼4 nearest neighbor) leads to an estimate for the time constant of NV transformation to H3 via capture by P1 of about 2 h at 1600 °C for a P1 concentration of 1000 ppm (with proportionally longer required for lower P1 concentrations). Once formed, the stability of H3 centers is limited by the dissociation into A-centers and vacancies (two nitrogen + vacancy). Theoretical calculations indicate a barrier of 6.5 eV for this process.[152] Assuming an effective attempt frequency of about 10 THz, this gives a dissolution rate of about 8 h at 1600 °C. Thus, there appears to be a possible window for the formation of large densities of H3 defects via annealing of N-rich, NV^- rich samples. Higher densities of H3 centers can be achieved at lower temperatures, with the trade-off being longer annealing times. For example, at 1500 °C, the time constants for H3 formation (at 1000 ppm N) and decomposition would be about 11 and 80 h, respectively. To avoid graphitization at such high temperatures, especially for nanodiamond samples, it is desirable for annealing to take place at high pressures in the absence of oxygen, as can be achieved in diamond anvil cells or HPHT reactors. Point defect diffusion has also been reported to depend on the defect's charge state.[155] Consequently, Coulombic interactions may accelerate the formation of H3 centers from P1 centers and negatively charged NV centers.

An alternative route to the formation of H3 centers is irradiation and annealing of Type IaB diamond that already contains large numbers of A-centers.[137] However, while the H3 signature can be observed in these materials, there are also large

concentrations of other competing complexes, including NV, N3V (N3 centers), N4V (B-centers), and N4V2 (H4) complexes.[153] It has also been found that the H3 emission is quenched by the large density of N aggregates in such materials.[156]

Chapter 4

PROPERTIES AND APPLICATIONS OF RARE EARTH FLUORIDES IN OPTICAL TWEEZERS

4.1 Laser Refrigeration of Alpha NaYF in Optical Tweezers

One of the major challenges with laser refrigeration is thermal isolation from substrates that can conduct heat into the cooled sample. Laser refrigeration is an inherently low power method of cooling due to saturation limits on absorption and the low amount of energy leaving the system per photon. This makes thermal isolation critical to successfully cooling, especially on the micro and nanoscale. While previous experiments used CdS nanoribbons to isolate crystals from a larger bulk substrate, a good solution for microscale systems is using optical tweezers, which will allow for non-contact levitation of the cooled sample. If sufficiently high vacuum is used, it is theoretically possible to isolate the cooling crystals from contact with any external molecules, including gasses. This makes optical tweezers extremely interesting as methods of studying the properties of rare earth fluorides for laser refrigeration applications.

4.1.1 Optical Tweezers for Nanocrystal Laser Refrigeration Experimentation

Optical trapping was first demonstrated by Ashkin in the 1970s[18, 157, 19], and since then, optical trapping of atoms, ions, and biological material (optical tweezers) has been intensely studied. Over the last decade, there has been new interest in trapping nano-scale particles in air and vacuum. Optically levitated nanoparticles have emerged as versatile high quality factor oscillators[158] whose motion can be precisely controlled with center-of-mass (COM) cooling[159, 160, 161]. Recently, COM

cooling reached the motional ground state[161, 162]. Levitated nanoparticles have been used as phonon lasers[7] and as precision force sensors for detecting Coulomb forces[163, 164, 165], Casimir forces[166, 167], and torques[168, 169, 170, 171, 172]. They have force sensitivities on the zepto-Newton scale[164] due to their isolation from the environment when trapped in high vacuum, which has applications in the search for non-Newtonian gravity.[173]

Trapped nanoparticles are good systems in which to study defect centers, due to their isolation from their environment. Color centers in general, and NV centers in diamond in particular, have received much attention for their atomic-like energy levels, ability to produce single photons[174, 175], and isolated spins with long coherence times at room temperature[176, 177]. NV centers have been used for thermometry[178] and extensively studied for quantum computing[179, 180, 181]. Levitating nanodiamonds with NV centers creates hybrid systems with motional and spin degrees of freedom in an isolated environment[177, 182, 183, 184, 185]. However, nanodiamonds are difficult to trap in high vacuum because optical absorption of the trapping laser causes the nanodiamond to heat and graphitize[186, 187, 188] when there is not enough thermal contact with gas molecules surrounding the nanocrystal to dissipate the absorbed energy, though recent work has shown that purer nanodiamonds are less prone to heating[189]. To take advantage of the spin degree of freedom in NV centers and pursue quantum behavior in trapped particles, the heating of levitated nanocrystals must be mitigated.

One way to overcome photothermal heating is laser refrigeration. Laser refrigeration was first suggested by Pringsheim in 1929[1] and realized experimentally in 1995[2]. Since then, rare-earth ions have emerged as excellent vehicles of laser refrigeration that have been doped into numerous crystals[190, 191]. Laser refrigeration can be used on optically levitated nanocrystals to combat optical heating since it is an optical technique and can address levitated nanocrystals without disrupting their isolation from the environment. Laser refrigeration of optically trapped crystals has

been demonstrated in Yb:YLF[5, 192] and shows promise to be a useful technique, but its effectiveness, limitations, and dependence on pressure need to be explored in more detail. Laser refrigeration of nanodiamonds themselves has also been proposed[193] but has not been demonstrated.

4.1.2 Trapping Design for Alpha NaYF

We observed anti-Stokes cooling of optically levitated Yb:NaYF nanocrystals. Yb^{3+} ions have a smaller splitting in the ground state manifold when doped in NaYF than other crystals, allowing for greater cooling efficiency[37]. Our Yb:NaYF particles were isotropic and nearly spherical, allowing us to avoid the rotation effects seen in previous work[192]. Yb:NaYF is safer to synthesize than Yb:YLF and predicted to be able to cool to $\sim$ 5 K colder[5, 37]. We explore the dependence of the cooling on the intensity of the cooling laser and the pressure of the surrounding gas. Cooling increases linearly with the intensity of the cooling laser. Further, we find that below pressures of $\sim$ 5 mbar the cooling is reduced due to the lack of thermal conduction to the gas molecules, which facilitates greater heating from the optical absorption of the trapping laser due to the presence of surface ligands on the nanocrystals.

We trap α-NaYF crystals with a nominal size of 100 nm doped with 10% Yb^{3+} [see Fig. 4.1a]. α-NaYF is a non-stoichiometric cubic phase represented by the chemical formula $Na_{0.5x}Y_{0.5+x}F_{2+2x}$. The exact stoichiometry can be measured with XRD[52]. The α-NaYF used in these experiments was observed to have x $\sim$ 0.07, leading to a stoichiometry of $Na_{0.43}Y_{0.57}F_{2.14}$. The α-NaYF crystals were grown using modified a hydrothermal process described in chapter 2. A 10% Yb:YCl3 solution is placed in an autoclave liner and chelated by stirring with an equal amount of tri-sodium EDTA. NaF is then added drop by drop to the mixture and stirred vigorously for 30 min. The mixture is then transferred to a stainless-steel autoclave and heated in an oven at 100 °C for 24 h. After cooling, the sample is collected from the autoclave liner, isolated by centrifugation, and then washed twice with water and twice with ethanol.

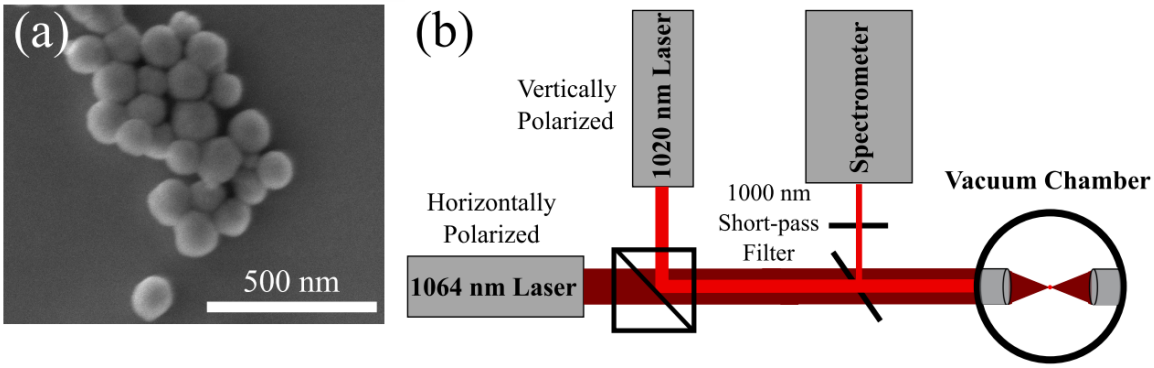

Figure 4.1: a) SEM image of NaYF nanocrystals used for laser refrigeration in the optical trap. b) A 1064 nm laser is used to create an optical dipole trap. Once trapped, the Yb3+ ions are excited using a 1020 nm laser, producing photoluminescence in the 930-1020 nm range, which is sent to the spectrometer.

Finally, the nanocrystals are dried at 80 °C for 12 h. These nanocrystals are dispersed in ethanol and nebulized into a vacuum chamber where a tightly focused 1064 nm laser creates an optical dipole trap. The electric field of the 1064 nm trapping laser induces a dipole in the nanocrystal, and the induced dipole moves in the intensity gradient of the laser to the point of highest intensity, the focus of the laser

4.1.3 Thermometry of NaYF Inside of Optical Tweezers

Once a crystal is trapped, a 1020 nm laser is introduced colinearly with the 1064 nm laser to excite the Yb^{3+} ions. Anti-Stokes PL emitted by the trapped crystal is collected through the same lens used to focus the trapping and cooling lasers. A 1000 nm dichroic beam splitter and a 1000 nm short-pass filter separate the PL from the laser light. The filter cuts off PL at wavelengths higher than 1000 nm, which is impossible to separate from the trapping and excitation lasers. Figure 4.1b is a schematic of the experimental setup showing the 1064 nm horizontally polarized trapping laser, 1020 nm vertically polarized excitation laser, vacuum chamber, and spectrometer. The collected PL is sent to a spectrometer, and the spectra are used

to determine the temperature of the crystal.

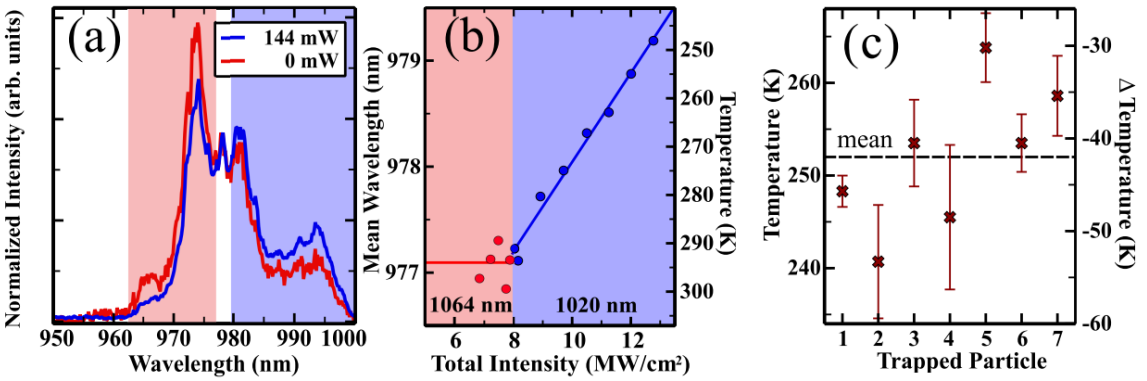

Figure 4.2: a) Normalized spectra taken with (blue) and without (red) the 1020 nm laser. With the 1020 nm laser, there is more PL from lower energy spectral peaks (blue region) and less PL from higher energy peaks (red region), which indicates cooling of the crystal lattice. b) Calculated mean wavelength for various intensities of the 1064 and 1020 nm lasers at 200 mbar. Intensities up to 8.1 MW/cm2 (red) are achieved with the 1064 nm laser, and intensities above 8.1 MW/cm2 (blue) are the 1020 nm laser added to the 1064 nm laser. The change in temperature is shown on the right axis. c) Lowest temperature reached by seven nanocrystals. The mean cooling is 42 to 252 K, with crystal 2 cooling the most, 53 to 241 K. Error bars are a one sigma confidence interval on the room temperature mean wavelength.

The PL emitted by Yb^{3+} ions can be used to calculate the crystal's temperature because the electrons in the excited state are in thermal equilibrium with the crystal lattice. Since the time scale of electron transfer between the excited state sublevels is much shorter than the lifetime of the state, the proportion of the election population in each sublevel follows the Boltzmann distribution. As the temperature of the crystal decreases, there are fewer electrons in the higher energy sublevel and therefore, higher energy (shorter wavelength) transitions become less likely. Figure 4.2a shows typical area normalized spectra with (blue) and without (red) the 1020 nm laser. To determine the temperature, the mean wavelength of each spectrum is calculated by taking a weighed average. Cooling the crystal results in a redshift in the mean wavelength with PL increasing at lower energy peaks [blue region of Fig. 4.2a] and decreasing at

higher energy peaks (red region).

The mean wavelengths for a range of both the trapping (1064 nm) and cooling (1020 nm) laser intensities are presented in Fig. 4.2b. The range of 1064 nm intensities is shown in red, and the range in blue shows the 1020 nm laser added to the 1064 nm laser. The mean wavelength does not significantly change over the range of 1064 nm intensities. For crystals at atmospheric pressure or low vacuum (>100 mbar), thermal contact with gas molecules keeps the crystal at room temperature when only the 1064 nm trapping laser is on. Variation in the mean wavelength is predominantly due to noise; the noise is significantly higher when only the 1064 nm laser is on because the PL counts are considerably lower, leading to more variation in mean wavelength. To compensate for the noise, the mean wavelengths for the 1064 nm intensities are averaged. The average is used to establish the room temperature (294 K) mean wavelength for each crystal and contributes the largest factor to the uncertainty in the total cooling. As the 1020 nm intensity is increased, the mean wavelength redshifts linearly, indicative of cooling. While higher 1020 nm intensities may cool the nanocrystal further, smaller increases in the total PL from the crystal at high intensities suggest we are close to saturating the cooling power of the Yb^{3+} ions

4.1.4 Calibration of Optical Tweezers Luminescence and Experimental Results

It is necessary to calibrate the redshift of the mean wavelength to determine the crystal's final temperature. To relate the change in the mean wavelength to the change in temperature, crystals were deposited onto a glass slide in a cryostat. Spectra were taken as the temperature of the cryostat was varied, and the change in the mean wavelength was noted. The shift in the mean wavelength is linear over a wide range of temperatures from 300 K down to 125 K. Below 125 K, the crystal phonons are frozen out and can no longer transfer electron population between sublevels. Therefore, the Yb^{3+} ions emit little to no PL in the 930–1000 nm range, and the mean wavelength of

the spectrum can no longer be used to calculate the temperature. The shift in mean wavelength with temperature was measured for multiple locations on the glass slide, and the slopes were averaged, giving the calibration of $\Delta\lambda_{mean}/\Delta T = 0.046 \pm 0.001$ nm/K, where the uncertainty is the standard deviation of the fitted slopes.

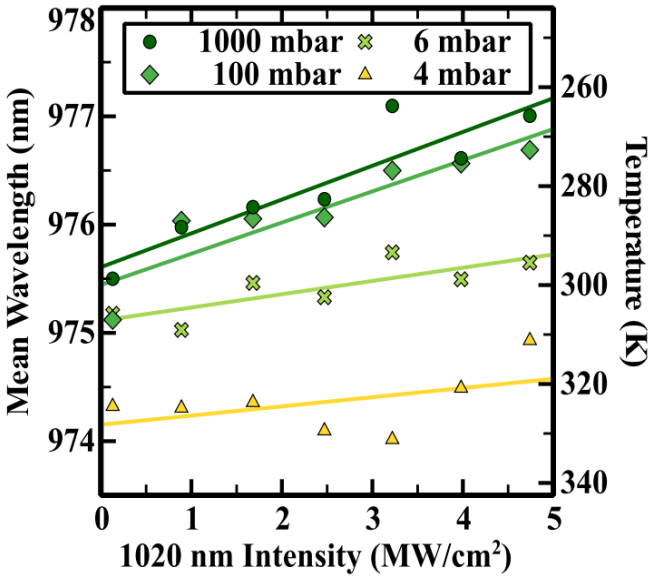

Figure 4.3: Mean wavelength as a function of 1020 nm laser intensity for a range of pressures. The amount of cooling achieved by the crystal is highly dependent on the surrounding pressure. At lower pressures, there is less thermal conduction from gas molecules, and the anti-Stokes cooling is balanced by heating due to optical absorption of the lasers.

Using the temperature calibration of the mean wavelength shift, the maximum achieved cooling can be calculated for each trapped crystal. Figure 4.2c shows the lowest temperature for seven trapped crystals. On average, crystals were cooled by 42 to 252 K, with the most efficient crystal cooling 53 to 241 K. Aside from the intensity of the 1020 nm cooling laser, there are two main factors determining the crystal's temperature: the pressure of the vacuum chamber and the intensity of the trapping laser. Collisions with air molecules provide the crystal's primary thermal contact and tend to keep the crystal at room temperature. Blackbody radiation is

negligible due to the small surface area of the trapped nanocrystals. As the pressure is decreased, the crystal becomes more thermally isolated, and the heating due to optical absorption and the laser refrigeration act in opposition. At pressures $\sim$ 5 mbar, the laser refrigeration begins to lose and the crystal cools less, showing an initial temperature 30 °C above room temperature and only 10 °C of cooling as the 1020 nm laser intensity is increased for a final temperature that remains above room temperature. The cooling achieved by the nanocrystals is controlled by surface effects of ligands left by the synthesis process. The surface contributes significantly to heating and is most affected by the thermal dissipation by gas molecules in the chamber. The dependence of the cooling on the pressure of the surrounding gas can be seen in Fig. 4.3. At high pressures (1000 and 100 mbar), the difference in the amount of cooling is 7°C with the crystal cooling the most at atmospheric pressure. When the pressure is in the single millibar range, the crystal's initial temperature is above room temperature and the amount of cooling decreases, leading to a final temperature that remains above 294 K.

4.2 Applications of Beta NaYF as Levitated Sensor

NaYF has applications in optical tweezers beyond potential refrigeration for nanodiamonds. While cooling some payload is the most simple application for laser refrigeration, it can also allow the NaYF (or other rare earth fluoride) to be used in sensing applications under more extreme conditions than other materials. The disc like morphology of the β-NaYF phase has a high aspect ratio that allows it to function as a levitated sensor. The unique feature of NaYF is that it could be cooled as a levitated sensor if the levitation beam is an appropriate wavelength. Every other type of material will experience some photothermal heating, even if it is supposed to be optically transparent and sufficiently pure. But having active cooling means that large laser irradiances can be used without vaporizing the sensor or affecting its mechanical and electronic properties.

4.2.1 Levitated Sensors in the Search for Gravity Waves

The field of levitated optomechanics is both rapidly developing and of high scientific interest, with a number of impressive recent results including achieving cooling to the quantum ground state[194, 195], high resolution surface force mapping[196, 197, 198], material limited gigahertz rotations[199], microscopic material studies[200], and high precision force[201] and acceleration[202] sensitivity. Near term goals include contributions to dark matter and energy searches[203] and astrophysics, including searches for high frequency gravitational waves (GWs) in the Levitated Sensor Detector (LSD), currently under construction[204].

With the first detection of gravitational waves[205], there have been a number of proposed and constructed experimental efforts to extend the observable GW frequency spectrum, such as the upcoming LISA mission[206, 207] and various other proposals[208, 209, 210, 211, 212, 213, 214, 215, 216, 217, 218]. Levitated sensors have been identified as a promising route to search for gravitational waves in the range of 10 kHz to a few hundred kilohertz[204, 219], where sources can include GW emission from annihilation of axions in clouds around spinning black holes or from inspirals and mergers of nearby sub-solar-mass primordial black holes within the Milky Way. In addition, a cosmological network of cosmic strings produces a stochastic background spanning frequencies from the nanohertz up to a cutoff well beyond the LSD band[220]. The sensitivity of such a levitated sensor detector benefits from low photon-recoil-heating and greater mass of the levitated particle. Both can be enabled by trapping disclike objects instead of spheres[204].

4.2.2 Demonstration of Beta NaYF as a Levitated Sensor

Here, we demonstrate optical trapping and study the motional dynamics of high aspect ratio, high mass, high mechanical frequency hexagonal prisms in vacuum. We compare the measured motional spectra with simulations, and we illustrate the

potential advances for high frequency gravitational wave detection made possible by trapping particles of this geometry. The main advance here is in achieving optical trapping and characterizing the dynamics of a dielectric object with a low-photon-recoil geometry while maintaining a large mass and high trapping frequency, which is essential for realizing the design sensitivity for the LSD gravitational wave search at frequencies above 10 kHz[204].

While small spherical particles can be trapped at high frequency ($\sim$300 kHz)[194, 195], the near-isotropic nature of their light scattering yields significant photon recoil heating, and their low mass is undesirable for the application of GW detection. Larger diameter ($\sim$10 μm) spherical particles have significant mass, but have only been realized in subkilohertz-frequency trapping configurations[202, 221]. The disclike geometry of high-aspect-ratio hexagonal prisms allows the ideal combination of high mass, high frequency, and low photon-recoil heating, and exhibits a clear improvement over levitated spheres, both in the regime when the sensor is dominated by thermal noise and when the sensor is limited by photon recoil. While these objects are of a lower mass than in our ideal design of LSD[204], this work represents a significant step along the technical roadmap and prepares us for trapping more customized similar objects in the final detector.

Since the first experimental demonstration of cold Brownian motion[5], solid-state laser refrigeration[87] has proven to be an effective way of preventing detrimental photothermal heating of optically levitated materials. In addition, NaYF and other rare-earth-doped crystals have been studied before in the context of optical vacuum levitation[222, 131] and have been shown to exhibit laser refrigeration when trapped with light of an appropriate wavelength. Previous experiments with both cubic (α) and hexagonal (β) phases of NaYF have either been with low mass subwavelength particles[131] or not optically levitated in vacuum[48]. By choosing such a material for the sensor, in the future laser refrigeration methods may enable higher trapping intensity and higher trap frequencies for gravitational wave searches approaching the

several hundred kilohertz frequency range. To produce multimicrometerscale high-aspect ratio particles relevant for GW detectors, we recently developed a novel hydrothermal synthesis[78] to drive growth of the hexagonal beta NaYF into thin, wide plates that was not previously possible[87].

Finally, as a general tool for precision sensing experiments, high aspect ratio trapped objects enable levitation of a multimicron scale object with mechanical frequencies in the tens of kilohertz, much higher than what is possible for similar mass spherical objects at similar optical powers[202, 221], due to the subwavelength size of the object in the optical axis. Additionally, β-NaYF has a density roughly double that of SiO_2, further increasing the mass of the trapped particle. Because of common noise sources at lower frequencies, for example from ground vibration or acoustic noise, this is a useful experimental platform for measurements, e.g., accelerometry, that would benefit from a sensor with larger mass and higher bandwidth.

4.2.3 Design of Dual-Beam Optical Trap for Levitated Sensor

A top-view schematic of the experimental setup is shown in Fig. 4.4a. Two focused counter propagating linearly polarized Gaussian beams, which are obtained from a 1550 nm laser via polarization-maintaining fiber-optic couplers and circulators, create a standing-wave optical dipole trap. Yb-doped β-NaYF hexagonal prisms are released from a glass substrate when driven by a piezoelectric transducer under 2–12 mbar of N_2 gas[223] and trapped in one of the antinodes of the standing wave (total power at the trap P $\approx$ 475 mW, and beam waist w $\approx$ 12 μm). We study two batches B1 and B2, with aspect ratios of approximately 8:1 (2.5 μm in diameter and 300 nm thick) and 15–25:1 (3–5 μm in diameter and 200 nm thick), respectively. The β-NaYF crystals are hydrothermally grown in an autoclave, resulting in a distribution of particle radii and thicknesses.

To characterize the motional dynamics of the prisms in the trap, we employed multiple independent detection mechanisms, as illustrated in Fig. 4.4a. Light scattered

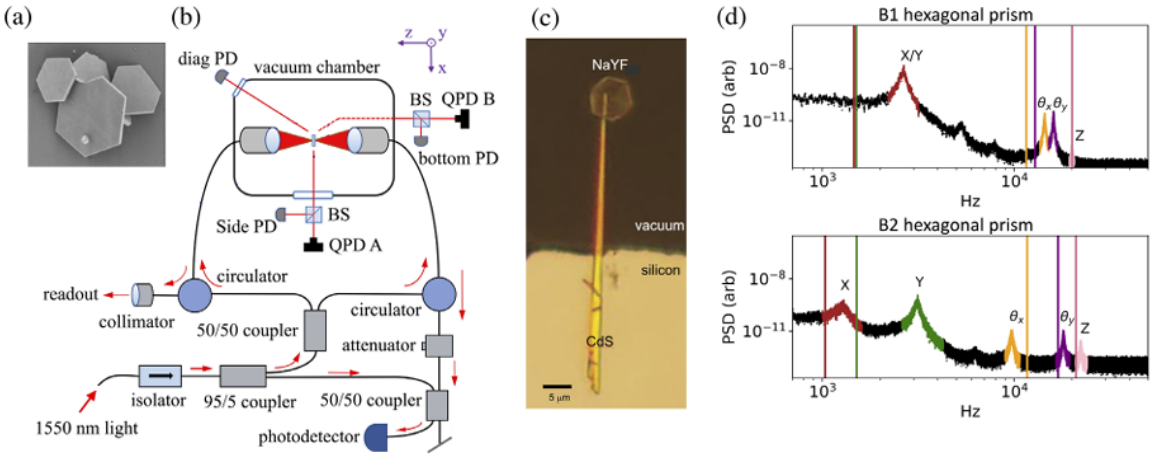

Figure 4.4: a) SEM micrograph of a cluster of NaYF hexagonal prisms from the B2 sample. b) Optical experiment design. The hexagonal prism is trapped at the foci of two 1550 nm counterpropagating beams. Fiber-based detection is achieved through homodynelike measurement through the fiber and the reference light out of the coupler through a fiber photodetector. Scattered light is also detected through photodiodes (PDs) and quadrant photodetectors (QPDs). c) Optical micrograph of NaYF prism, adapted from Ref. [78]. d) Spectral density of the motional signal at 2.2 mbar recorded by one of the QPD detectors. Motion corresponding to five principal degrees of freedom (x;y;z;θ_x;θ_y) of the hexagon is visible. Vertical lines indicate calculated frequencies from a finite-element simulation for similar prisms, showing qualitative agreement.

from the prism is partially coupled back into the polarization maintaining fiber and interferes with the reference light out of the 95/5 optical coupler to achieve homodyne-like interferometric detection through a fiber photodetector. The image of the prism is projected onto two quadrant photodetectors from the side and bottom of the vacuum chamber, respectively. Additionally, scattered light is directly detected by three free-space biased photodiodes which view the prism from the side, bottom, and top diagonal windows of the chamber. Along the optical axis the positional information of the prism is encoded mainly in the phase of the light given the prism's subwavelength thickness in this direction. Off-axis positional information is encoded mainly in the intensity due to the much larger (a few micrometers) transverse dimensions of the

prism.

4.2.4 Modeling and Observations of Dynamics of Trapped Hexagonal Prism

Optical trapping of spheres in the Rayleigh, Mie-Lorentz and geometric optics regime is a fairly well studied problem experimentally and theoretically. Furthermore, several novel geometries have been explored in the subwavelength (Rayleigh) regime. The expected form for nonspherical objects optically trapped in the Mie-Lorentz regime is a topic of recent theoretical investigation[224]. While a sphere trapped in the Mie-Lorentz regime will exhibit 3 degrees of freedom, in contrast for a high-aspect ratio radially symmetrically object (i.e., a disc or disc like object) we would expect to see 5 degrees of freedom, since the 6th degree of freedom (that of the hexagonal prism spinning around its most symmetrical axis) is poorly optically coupled. Our β-NaYF hexagons are neither perfectly symmetric nor optically isotropic so we would expect to see a coupling to the output light in the case that the rotations around that axis were driven. This could be explored in future experiments for example by using circularly polarized trapping light, since β-NaYF is birefringent.

The analytic approach predicts the mode ordering in frequency space that we observe, however, due to the noninfinitesimal thickness of the hexagonal prisms used in the experiment we use a finite element model implemented in PYGDM2[224] to compute the expected optical forces and frequencies of the trapped prisms. Computed frequencies for our geometries are overlaid over experimental data in Fig. 4.4d.

Power spectral density data for the motion of two sizes of hexagonal prisms, lower aspect ratio B1 and higher aspect ratio B2, trapped using 475 mW of laser power at a pressure of 2.2 mbar are shown in Fig. 4.5 for each of the detection mechanisms described previously. We pinpoint the mechanical resonances of the prisms by identifying peaks at same frequencies in multiple detectors. Peaks corresponding to primary translational and rotational mechanical resonances x, y, θ_x, θ_y, and z are denoted by vertical dashed lines. All other peaks are identified as known harmonics, sidebands,

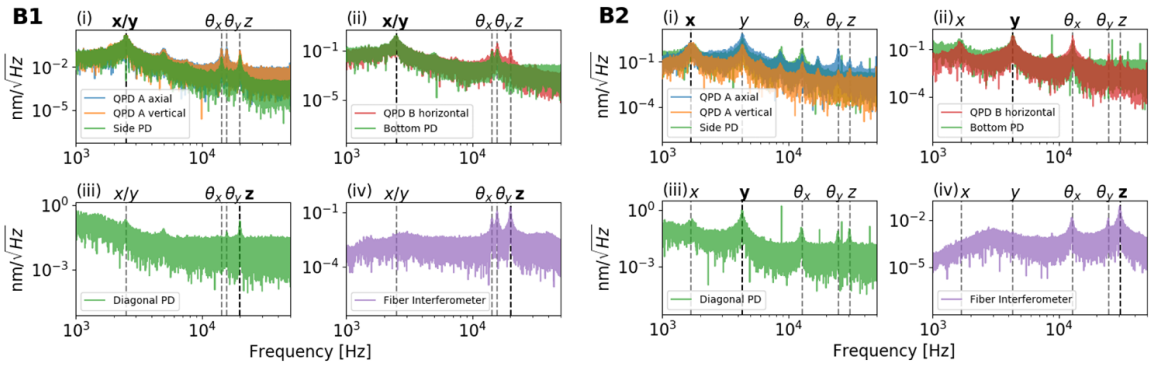

Figure 4.5: Experimentally obtained power spectral densities for two sizes of hexagonal prisms, B1 and B2 from detectors oriented to the side (i), bottom (ii), top diagonal (iii), and along the trap axis (iv). Detector types include quadrant photodetectors (blue, orange, and red), biased photodiodes (green), and a fiber-coupled homodyne-like interferometric detector (purple). Observed peak maxima corresponding to x, y, θ_x, θ_y, and z motion are denoted by vertical dashed lines. In some cases, higher harmonics of the labeled peaks are visible in the spectra, indicating the presence of nonlinearities.

or electronic noise in the system. The conversion to nm/$\sqrt{Hz}$ is done for a harmonic trapping potential by assuming thermal equilibrium and fitting a strongly coupled peak to a Lorentzian function. The thermally driven p torsional root-mean-squared amplitudes of the modes θ_x and θ_y can be estimated by the equipartition theorem: $\theta_{x(y)} = (1/2\pi f_{\theta_{x(y)}})\sqrt{(k_B T/I)}$, where $f_{\theta_{x(y)}}$ is the observed torsional frequency, k_B is the Boltzmann constant, T is the temperature, and I is the moment of inertia. The calculated root-mean-square amplitudes of θ_x and θ_y are 1.7$\times$ 10^{-2} rad and 1.5 $\times$ 10^{-2} rad, respectively, for B1 and 9.1 $\times$ 10^{-3} rad and 4.7 $\times$ 10^{-3} rad for B2. We do not observe free rotations or bending modes, tested up to 10 MHz, as expected since the θ_x and θ_y modes of the prism are small amplitude, stable linear oscillatory modes about the plane of the standing wave's interference fringes and bending modes are not predicted to be observable within our resolution for this geometry. Since no free rotations are observed, we also do not observe the presence of a significant precession term as in Ref. [225].

The analytic model for a thin disc from [226] predicts a small amount of mode splitting along x/y and θ_x/θ_y axes, with the effect increasing the further the levitated object is from the Rayleigh regime— specifically in the radial axis. Therefore, a wider hexagonal prism will have a less degenerate set of x/y and θ_x/θ_y modes. This effect can be seen in both the outputs of the numerical model and the experimental data. Specifically in Fig. 4.52, the x/y modes for the radially smaller B1 hexagon are nearly degenerate and the θ_x/θ_y modes are much closer together than for the radially larger B2 hexagon. Mode splitting is also often seen in levitated particles in the Rayleigh limit, caused by the asymmetric potential generated by polarization dependent focusing of the beam[227]. Since our prisms are well into the Mie-Lorentz regime, separation between the modes results both from the polarization dependent focusing bias of the lens and geometry-dependent scattering resonances within the levitated particle.[78]

Figure 4.4d shows the power spectral density (PSD) of an optically trapped hexagonal prism with values from the finite element model (FEM) overlaid. The location of the peaks in the PSD is broadly in line with that computed by the FEM. It is of note that the frequency of the z degree of freedom is mainly dependent on the thickness of the hexagonal prism, while the mode splitting is mainly dependent on its radius. We assume the prism has uniform thickness, and surface roughness is not modelled. Differences in the observed frequency of the x/y motional modes to those predicted by the FEM may be driven by edge effects due to the prism's tapered shape. Because of memory and CPU time driven resolution constraints the FEM assumes a flat face on the hexagons prism's thin edge. Differences may also result due to geometry dependent Fabry-Perot and whispering gallery-mode-like resonances within the levitated prism[78].

4.2.5 Sensitivity to Gravitational Waves

For the application of gravitational wave detection, a disc-shaped particle or hexagonal prism can be suspended in a standing wave in an optical cavity. For such a configuration, as discussed in Ref. [204], the minimum detectable strain h_{limit} for a particle with center-of-mass temperature T_{CM} is approximately

$$h_{limit} = \frac{4}{\omega_0^2 L}\sqrt{\frac{k_B T_{CM}\gamma_g b}{M}[1+\frac{\gamma_{sc}}{N_i\gamma_g}]}H(\omega_0) \tag{4.1}$$

for a particle of mass M trapped in a cavity with response function $H(\omega) \approx \sqrt{1+4\omega^2/\kappa^2}$ for a cavity of linewidth κ. Here $N_i = k_B T_{CM}/\hbar\omega_0, \gamma_g = (32P/\pi\bar{v}\rho t)$ is the gas damping rate at pressure P with mean gas speed $\bar{v}$ for a plate or disc of thickness t and density ρ, and b is the bandwidth.

The photon recoil heating rate for a plate- or disc-shaped structure is [204, 219, 228] $\gamma_{sc} = (V_c\lambda\omega_0/4L)[1/\int dV(\epsilon-1)] \times (1/F_{disc})$ is inversely proportional to the disc-limited finesse F_{disc}, i.e., 2π divided by the fraction of photons scattered by the disc outside the cavity mode. The integral is performed over the extent of the suspended particle. Here V_c is the cavity mode volume[219]. For a subwavelength spherical particle of volume V in the Rayleigh regime, $\gamma_{sc} = \frac{2}{5}(\pi^2\omega_0 V/\lambda^3)[(\epsilon-1)/(\epsilon+2)]$.

At higher pressure, the sensitivity is limited by gas collisions, while at ultrahigh vacuum, $\gamma_{sc} = N_i\gamma_g > 1$ and eventually the sensitivity is limited by photon recoil heating. The thermal-noise limited sensitivity generally scales as $\sqrt{P}$ in the gas-dominated, ballistic regime. At a given pressure, we can define a figure of merit $\eta_{thermal}$ which describes the dependence on particle mass, geometry, and trapping frequency as $\eta_{thermal} \equiv \omega_0^2\sqrt{M\rho l}$ where ω_0 is the trapping frequency along the cavity axis, $l = r$ or $l = t$ for spheres of radius r or plates of thickness t, respectively. Correspondingly, we define figure of merit $\eta_{recoil} \equiv \omega_0^{3/2}\sqrt{M/\gamma_{sc}}$ for sensitivity to GWs in the photon recoil dominated limit.

In Fig. 4.6b, we show $\eta_{thermal}$ for several recent experimentally realized configu-

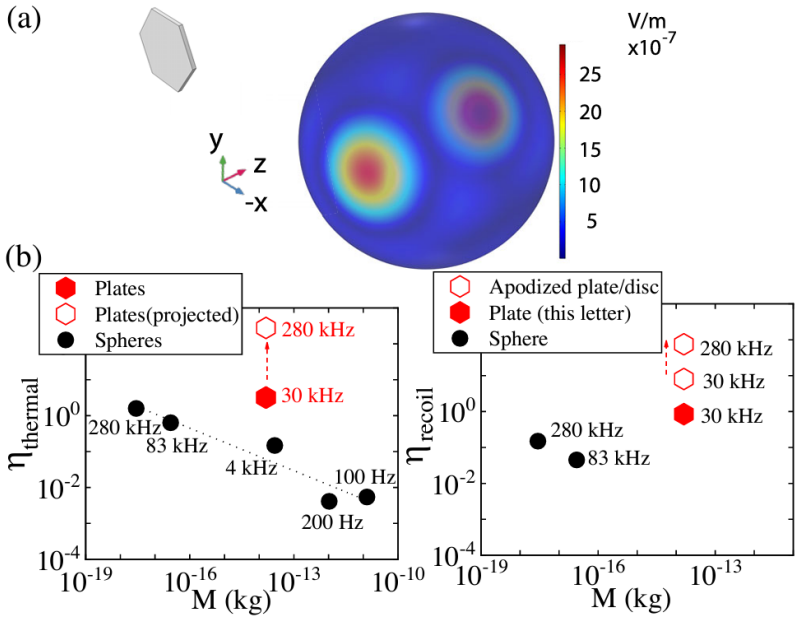

Figure 4.6: a) Calculated far-field scattered electric field profile for a hexagonal prism of thickness 200 nm and diameter 4 μm. b) (left) Figure of merit $\eta_{thermal} = \omega_0^2\sqrt{M\rho l}$ (in units of $\mathrm{Hz^2 kg/m}$) in the thermal-noise dominated limit. At equal masses, high aspect ratio levitated plates significantly outperform levitated spheres for gravitational wave experiments. Projected sensitivity for the same size plate held at higher trapping frequency is shown. (right) Figure of merit $\eta_{recoil} = \omega_0^{3/2}\sqrt{M/\gamma_{sc}}$ (in units of Hz $\mathrm{kg^{1/2}}$) in the photon-recoil-heating dominated limit. Projections shown for a prism of the size trapped here, for currently realized beam parameters with an estimated F_{disc} of 1.1×10^3 (solid hexagon) and for two trapping frequencies with a suitably apodized edge and beam waist profile, with an estimated F_{disc} of 10^5 (open hexagons).

rations. When comparing objects of similar mass, the higher frequencies obtained for our hexagonal prisms show a significant improvement.Although the values of $\eta_{thermal}$ realized in the present work are only marginally better than those obtained for some of the smallest nanospheres trapped at very high frequencies (driven by the ω_0^2 scaling), by raising the trapping intensity we estimate for our geometry it should be possible to greatly exceed the highest values obtained in these experiments.

In ultrahigh vacuum, disc or hexagonal prism shaped objects show a distinct advantage, due to the more-directional nature of their scattering [as shown in Fig.

4.6a]in contrast to the nearly isotropic scattering from small spherical particles in the Rayleigh regime. In Fig. 4.6b we plot η_{recoil}, focusing on the higher frequency domain with a comparison between nanoparticles in the Rayleigh limit and hexagonal prisms of thickness 200 nm and diameter 5 μm. The hexagonal prisms outperform the nanoparticles by 2 or more orders of magnitude for a disc-limited finesse of $F_{disc} = 10^5$, reasonable for a suitably apodized disc or prism trapped in a beam with waist equal to half the particle radius [204, 228]. For further GW sensitivity, a stacklike geometry[204] may be possible by using a central NaYF spacer and two end caps with high refractive index low-loss material such as Si or Al_2O_3, e.g., deposited by pulsed laser deposition[229] or evaporation.

Behavior of Alpha NaYF in Aqueous-Based Optical Traps

Previous discussion focused on the properties and behavior of NaYF trapped in air or vacuum, but it is also possible to trap while in solvents. Aqueous conditions represent a huge set of interesting chemical environments, especially for scientific fields like biology and geochemistry. NaYF could be used to study these chemical environments, especially when it comes to colloidal materials. Understanding the interactions of colloids is critical to modeling and predicting their chemistry, and NaYF can be used to study the interactions of colloids using optical tweezers to isolate individual crystals without causing significant heating that could affect local chemistry.

4.2.6 Important Colloidal Forces on Aqueous Nanocrystals

Colloids represent a massive set of chemical environments, and the interactions between colloidal particles govern the behavior of many important scientific fields & processes, including nanotechnology[230, 231], crystal growth[232, 233], and aggregation & assembly[234, 235]. Understanding the forces experienced by colloidal materials is integral to furthering colloidal science. Significant work has been done to under-

stand colloidal systems regarding particle assembly through the energetics of colloidal interactions, namely van der Waals interactions and surface potentials. While the energetics are critical to understanding assembly, it is important to not preclude or otherwise insufficiently account for the impact of solvent dynamics on particle interaction and assembly. DLVO theory[236, 237] or a modified version of DLVO theory is commonly used to model assembly and aggregation of colloids. While it is not uncommon to modify DLVO theory to include some hydrodynamic lubrication force corrections, a deeper look at the variables governing the hydrodynamics of a colloid is needed to form a more thorough understanding of colloidal interactions leading to assembly.

The net forces in effect on a colloid are not limited to just the energetic and dynamic forces. External forces can also be applied to colloids to drive aggregation. These include, but are not limited to, electric fields, magnetic fields, thermal convection, and optical forces. Most of these can be easily applied to bulk solvent, but it can be challenging to apply locals fields or forces at the micro-to-nano size scale. However, optical forces are especially well-suited to applying forces on the micro to nano size scale through the use of optical tweezers. The application of optical tweezers allows the study of extremely sensitive forces and can be used for a broad array of experiments, including recent experiments demonstrating cooling of trapped particles to quantum ground states[194]. By trapping particles with optical tweezers, it is possible to study dynamics of colloidal particles in aqueous systems relative to a fixed particle in the trap.

The colloidal dynamics and assembly of alpha-phase sodium yttrium fluoride (α-NAYF) crystals trapped in water due to optical tweezers were studied. Rare earth fluorides, such as α-NAYF, are in interesting class of materials to study with optical tweezers due to their applications in solar energy materials[25], bioimaging[30], laser gain media[22], infrared upconversion phosphors[238, 239], quantum memory devices[24], vision therapy[31], gravity wave sensors[240], and anti-counterfeiting by

functioning as barcodes through their luminescence[28, 27].

α-NAYF was initially chosen as the material due to its interesting applications in laser cooling and small crystal size ideal for near infrared optical tweezers. Ytterbium can be doped into the materials, and used to upconvert near infrared light with near unity efficiency to draw energy out of the lattice vibrations to lower the temperature of the crystal[133]. These materials have been demonstrated to be able to cool in aqueous and physiological conditions using optical tweezers to isolate them thermally from any bulk substrate beyond the solvent[5, 48]. These materials can also experience heightened trapping forces if the trapping laser is resonant with lanthanide dopants, making it possible to trap under lower laser irradiances compared to materials with similar indices of refraction[241]. Sodium yttrium fluoride is particularly interesting rare-earth fluoride for cooling applications due to its low crystal field splitting[242], but the composition of the crystal is complicated. The alpha phase in particular has a high degree of disorder and be better described as a crystalline solution of NaF and YF_3[86, 243]. This disorder leads to a nonstoichiometric ratio of ions in the crystal structure that can vary depending on synthesis conditions[55]. This variable composition can be measured using XRD[52], but the complexity of the structure of this material is worth noting, as the variable stoichiometry and disorder could lead to unusual behavior compared to pristine cubic systems.

The optically driven attachment and assembly of α-NAYF colloidal crystals into linear chains is demonstrated here. These crystals are suspended in pure water and are drawn into a trap from optical tweezers. When multiple crystals are drawn into the trap, they spontaneously assemble into a linear chains that persists even when the crystals are removed from the trap. The forces acting on these crystals are then calculated and it is shown that the increased roughness of the particles allows for the hydrodynamic repulsion to be overcome, allowing attachment to occur. This demonstrates the critical importance of understanding the impact of dynamics on colloids, which is used in conjunction with the energetics in determining the behavior

of the colloidal crystals under these conditions.

4.2.7 Observed Assembly of Alpha NaYF in an Optical Trap

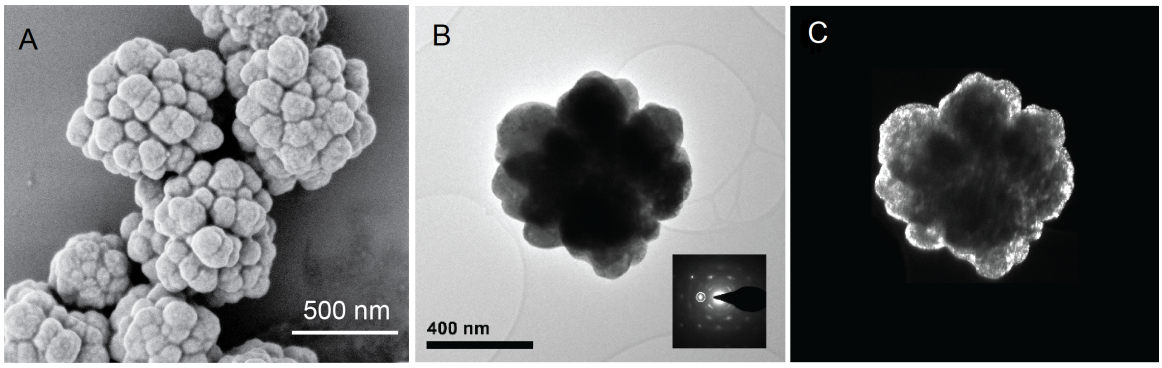

Figure 4.7: α-NaYF Sample Used in Optical Tweezer Assembly Experiment. A) SEM micrograph of ligand-free α-NaYF used in assembly experiment. B) Bright-field TEM micrograph of α-NaYF. Inset: SAED-diffraction of α-NaYF sample. C) Reconstructed TEM micrograph from SAED diffraction at a single spot, demonstrating single crystallinity of the α-NaYF samples

The experiments focused on the the observed assembly of α-NAYF into linear chains structures in the presence of optical tweezers. A powder of ligand-free α-NAYF was synthesized hydrothermally, which resulted in a rough morphology. This α-NAYF was suspended in water and studied in optical tweezers, where the spontaneous assembly process was observed. In the presence of a strongly focused laser, the optical forces experienced by the α-NAYF due to the laser were enough to overcome hydrodynamic resistivity, bringing the crystals close enough for van der Waals forces to become extremely strong, resulting in contact between crystals. This spontaneous assembly occurs through the use of focused light only. Many forms of assembly are possible, but they are typically done through chemical and photochemical reactions[234] or attachment to a substrate through some form of deposition[235, 244]. Recent work has also shown possible wire assembly through a nanosoldering process[245, 246]. The observed assembly in these experiments occurs without any major chemical reaction

or nanosoldering process occurring, and the assembly is truly 3D, as the assembly occurs while directly suspended in water with no substrate required for the assembly process.

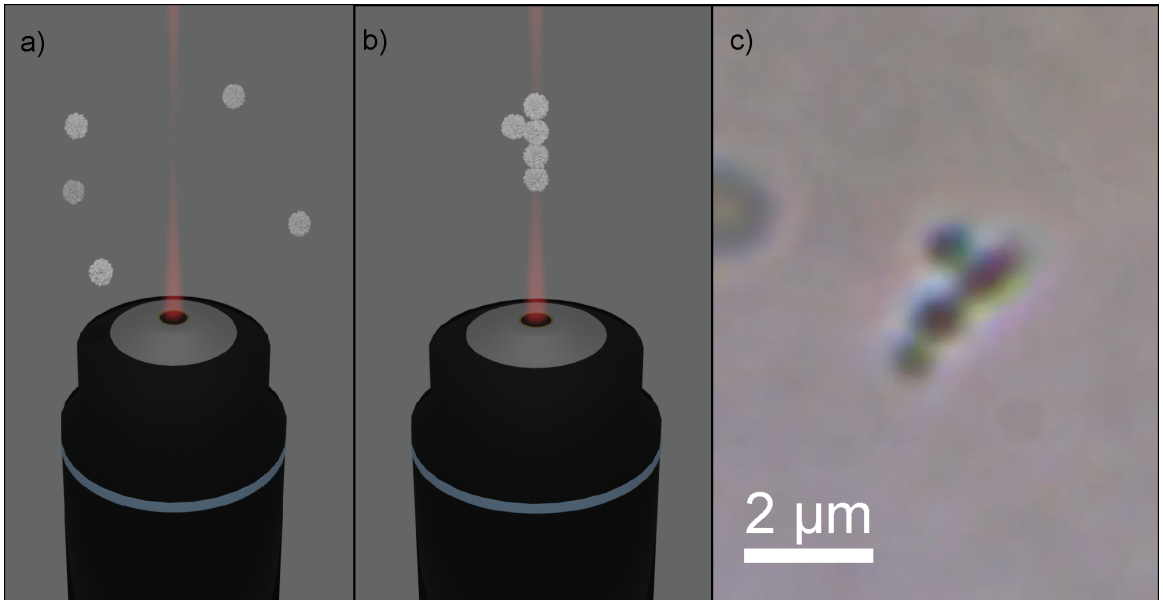

Figure 4.8: Schematic of α-NaYF assembly in water. A) Artistic representation of α-NaYF in free suspension near the optical trap. B) Artistic representation of α-NaYF that has been assembled into a chain, with one α-NaYF attached to the side. C) Optical micrograph of experimentally observed α-NaYF chain represented in (B).

The result of the synthesis was an usual morphology of α-NAYF that was very rough, seen in figure 4.7A. The rough surface at first appears to be an agglomeration of smaller α-NAYF crystals, but TEM data in figure 4.7B and C shows that the rough α-NAYF are single crystals despite their odd morphology. Smooth α-NAYF crystals were also grown for comparison. Both the rough and smooth α-NAYF crystals were confirmed to be the same composition using XRD. When a single α-NAYF crystal was trapped, no unexpected behavior was observed. However, when multiple rough α-NAYF crystals were introduced into the trap, the crystals unexpectedly assembled into a linear chain aligned with the trapping beam, shown in figure 4.8. The

linear structure persisted after the trapping beam was removed and no disassembly was observed over several hours of observation. Spontaneous assembly without the trapping beam was never observed, though occasional 'couplets' of two α-NAYF crystals could be found immediately after suspension, which may only be the result of twinned crystals in the synthesis process. Chain lengths of up to 10 α-NAYF crystals (approximately 8 μm long) have been made, with the main limitation being working distance of the objective lens. The limit for the chain length seemed to arise from the focal length of the laser used in the optical tweezers. After the chain exceeded 10 crystals, the far end of the chain rested well outside the focal plane and the linear structure began to be unstable. If the crystals were anchored to a surface or if the optical power used to form the trap were greater, it may be possible to make longer chains and structures. The shape and linear orientation of the assembled crystals may provide good samples to provide empirical data in comparison to optical force calculations of nonspherical nanostructures in existing literature[247].

4.2.8 Modeling of Colloidal Forces on Alpha NaYF Microcrystals

To understand the assembly process, the colloidal α-NAYF crystals were modelled by their position and velocity in a 3D space. Two α-NAYF crystals were placed in a 3D coordinate space, then their velocities were calculated by multiplying the sum of all forces by the mobility

$$V = M \cdot \Sigma F \tag{4.2}$$

where V is the velocity of the particle, M is the mobility, and ΣF is the sum of all forces acting on the particle. For our model, these forces include van der Waals forces, electrostatic forces, hydrodynamic repulsion, Brownian forces, and any external forces. When these forces are substituted in, the velocity for a given particle looks like

$$V = M \cdot (F_{vdw} + F_{elec} + F_{hyd} + F_B + F_{ext}) \tag{4.3}$$

where F_{vdw} is the van der Waals forces, F_{elec} is the electrostatic force, F_{hyd} is the hydrodynamic repulsive force, F_B is the Brownian force, and F_{ext} is any set of external forces acting on the system. The velocity calculated at each time step in the simulation, and the position of the particle is updated and the velocity recalculated. This calculation loop was repeated until the positions of the particles indicated contact, and the calculated time required for contact was recorded. The van der Waals forces and the electrostatic force are conservative forces that can be derived from the potential energy, hence them being part of the energetics that are commonly considered with colloids. The dynamics come from the non-conservative random force (i.e. Brownian force) and dissipative force, which we call here the hydrodynamic force. While the Brownian force is random, the hydrodynamic force is purely repulsive and inhibits assembly. As particles get closer to each other in proximity, the hydrodynamic force grows more repulsive. Having an accurate model of the hydrodynamic force is essential to determining the probability of assembly occurring as this force is a primary deterrent from particles getting close enough to assemble.

The energetics are straightforward to calculate, as they consist of the van der Waals forces and the electrostatic force. The van der Waals forces are derived from the material properties of the colloidal crystals. The electrostatic force was calculated based on the zeta potential of the crystals suspended in solution as an approximation for the surface potential. The zeta potential for the rough 1 μm diameter α-NAYF crystals varied slightly from synthesis to synthesis, but was always a positive value. We measured the maximum zeta potential to be $+29.1 \pm 4.0$ mV, which we will use as the upper bound for our simulations. We then measured the smooth 125 nm diameter α-NAYF crystals to have a zeta potential $+34.3 \pm 2.4$ mV. More details about the calculations of this force and the other forces can be found in the supplementary materials. The electrostatic force was used to solve the net force upon the crystals in the experiment and included in all calculations, but the magnitude of the zeta potential is very low and the effect of the electrostatic force was found to be negligible

in this system.

For colloidal particles in the presence of optical tweezers, many forces simultaneously influence the relative position and velocity of each particle. Some forces, such as the Brownian force, are well characterized, and an additional description of these forces are not required here. Instead, we will focus on describing the optical forces, the electrostatic force, and the van der Waals force that are affecting the particles in the trap.

The presence of optical tweezers introduces three forms of optical force on particles in the tweezers: the gradient force, the scattering force (also known as radiation pressure), and the spin-curl force[248]. The spin-curl force is only present with non-homogeneous polarization, which does not apply to our experimental conditions. The scattering force is always present with optical tweezers, but the direction of the scattering is in the direction of the beam propagation of the trapping laser. As such, it does not apply a significant relative attractive or repulsive force between particles when considering approach at close separation distances and especially if considering approach from a radial direction.

The main force of interest for the experiments shown here is the gradient force, which draws particles into the focus of the trapping laser. For simplicity of modeling the gradient force, we apply the dipole approximation which treats the trapped particles as dipoles with homogeneous internal fields. If this approximation is used, then the time-averaged gradient force can be expressed as

$$F_{grad}(r) = \frac{1}{4}\alpha_p' \nabla |E_i(r)|^2 \tag{4.4}$$

where r is the radial distance from the trap, α_p' is the real part of the polarizability of the particle in the trap, and E_i is the electric field incident on the particle from the laser. This can be simplified further using relation between the electric field and the intensity of the electric field for a Gaussian beam, which yields

$$F_{grad}(r) = \frac{1}{2}\frac{\alpha_p'}{cn_m} \nabla I_i(r) \tag{4.5}$$

where c is the speed of light, n_m is the refractive index of the surrounding medium, and I_i is the intensity of the electric field incident on the particle. This equation for F_{grad} is used in our calculations to determine the strength of the attractive external force (F_{ext}) on the particles.

The electrostatic force (or Coulombic force) determines the attraction or repulsion of colloidal particles due to surface potentials. This is well defined for point charges, and analytical solutions have been developed for spherical particles in a colloidal dispersion. Broadly, the electrostatic force between two identical colloidal particles can be descibed as

$$F_{elec} = 2\pi\epsilon_r\epsilon_0\psi_s^2\kappa_D\bar{a}e^{-\kappa_D h} \tag{4.6}$$

where ϵ_r and ϵ_0 are, respectively, the permittivity of the relative electrolyte solution and the permittivity of vacuum, ψ_s is the surface potential of the spheres, κ_D is the Debye screening vector which is the inverse of the Debye Length, $\bar{a}$ is the reduced radius of the particles which can be represented by just a for identical particles like described in this experiment, and h is the separation distance between the surfaces of the particles. This particular formulation works for point charges and does not account for the complexities of real objects like found in a colloidal suspension. Using existing solutions for spherical particles, and if we approximate our crystals as spheres, then we can solve for the electrostatic force of two spheres as a function of surface potential, which yields

$$F_{elec} = 2\pi\epsilon_r\epsilon_0 a\psi_s^2\kappa_D e^{-\kappa_D h}(1 - e^{-\kappa_D h}) \tag{4.7}$$

and is valid for the conditions $\kappa_D a \gg 1$ and $h \ll a$, which is in agreement with Ohshima[249] and Sader et al[250]. For the larger particles in this experiment, radii are on the scale 500 nm. The condition $\kappa_D a \gg 1$ is valid for these particles at net ionic concentrations above 10^{-4}, while the other condition is valid at short separation distances where the attachment events are occurring. When using this equation in combination with attachment events, all conditions should be valid with a sufficiently

high ionic concentration.

Lastly, the van der Waals forces are a major attractive force for colloidal particles at sufficiently small separation distances. As particle sizes increase beyond sizes on the order of 10 nm, the center of mass is sufficiently far away to have a diminished impact on the van der Waals forces. A more complex solution for the forces is necessary, which has already been solved for spheres by Pailthorpe and Russel[251]. Using their solution that has been solved for force values, we arrive at

$$F_{vdw} = -\frac{A_H}{3}[\frac{2a^2(h+2a)}{[(h+2a)^2-4a^2]^2} + \frac{2a^2(h+2a)}{[(h+2a)^2]^2} - \frac{h+2a}{(h+2a)^2-4a^2} + \frac{h+2a}{(h+2a)^2}] \quad (4.8)$$

where A_H is the Hamaker constant for the material of interest. While this equation is correct, it can be simplified at low separation distances. At conditions where $h \ll a$, the question can be greatly simplified to

$$F_{vdw} = -A_H a/h^2 \quad (4.9)$$

which is highly useful since attachment events between spheres must take place at low separation distances by definition.

A major component of modeling the repulsive forces experienced by trapped particles is the hydrodynamic force. This force is commonly thought to increase inversely with the distance between particles, but this applies to perfectly smooth objects. Imperfect, rough surfaces reduce the overall hydrodynamic repulsion experienced between two particles by allowing the external fluid to slip at the surfaces of the particles. This reduced hydrodynamic force is modeled by Jenkins & Koenders and is shown to produce a finite repulsive force at a zero separation distance[252]. We used their approach to model a rough sphere using a spherical mesh where elements of the sphere are allowed to randomly reduce the distance from the center of the sphere anywhere from 0% to 30%, using a boundary element computational approach based on previous works by Aragon[253] and Aragon & Hahn[254]. This allows for a highly roughened surfaced with negligible effect to the effective radius by using a sufficiently

high mesh count. Wire frame models of the shapes used can be seen in figure 4.9. The hydrodynamic force was modeled for the rough spheres and compared to the analytical solution for a smooth sphere from Jeffrey & Onishi[255]. The hydrodynamic repulsive force experienced by a smooth sphere exponentially increases as a function of decreasing separation distance according to the lubrication limit of a smooth sphere. In contrast, the rough sphere approaches an asymptotic limit to a finite resistivity caused by hydrodynamic repulsion. This would suggest that it is reasonable for sufficiently roughened particles to have minimal resistance to physical contact with each other and that optical tweezers may be able to generate sufficient force to drive rough particles into physical contact for assisted assembly, emphasizing the importance of thoroughly modelling and understanding the hydrodynamics of colloids. If dynamics are ignored or insufficiently understood, the predicted behavior may be extremely different.

The external force caused by the optical tweezers provides a net attractive force, drawing the crystals into the center of the focal plane of the optical trap. These forces consist of two main forces: gradient forces and radiation pressure. Gradient forces attract the particles to the center of the focal plane of the laser. Radiation pressure arises from light scattering off the surface of the particles. The momentum from the light is transferred into the particles, pushing them in the direction of the beam propagation and slightly out of the center of the trapping beam focal plane. These forces were simulated using the Optical Tweezers Toolbox, which is capable of modeling the forces on nanoparticles in an optical trap[256]. The smooth α-NAYF crystals were simulated using a sphere, while the rough α-NAYF crystals were simulated using a 3D model of close packed spheres to replicate the shape. These different shapes were simulated to extract out the optical forces on them at every position in space. These forces were then exported and used for simulating particle collision for two crystals entering an optical trap.

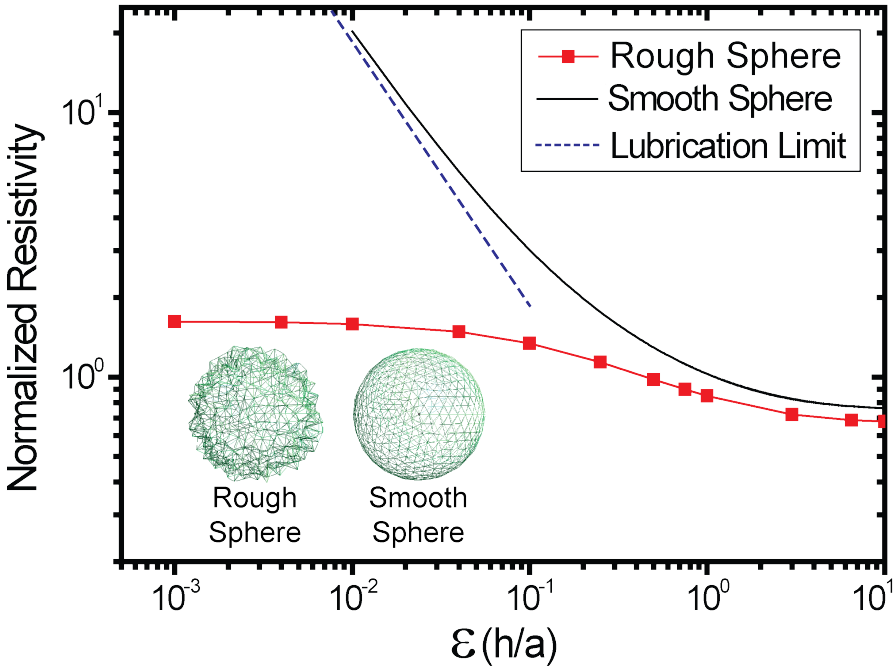

Figure 4.9: Hydrodynamic resistivity of α-NaYF approaching each other in an aqueous colloid for both rough α-NaYF and smooth α-NaYF, where h is the distance between the α-NaYF crystals and a is the radius of the α-NaYF crystals. Rough α-NaYF demonstrates an asymptotic limit to the resistivity as the α-NaYF grains approach each other, which is not seen in the smooth case.

4.2.9 Understanding the Interplay of the Energetics and the Optical Forces

Further physical insights on the attachment can be obtained by considering a coordinated interplay between the two major attractive forces in this system. The first attractive force is the optical gradient force (F_{grad}) due to the existence of an external optical field from the laser and the second one is the van der Waals force (F_{vdw}). The coordinated interplay represents that the gradient force brings particles together to a close separation where the van der Waals force can take over for collision. Based on the dipole approximation and a low separation distance ($h/\omega_0 \ll 1$) where h is the radial distance in the transverse plane and ω_0 is the beam waist, a radial component

of F_{grad} can be approximated by

$$F_{grad} = -\frac{2\alpha_p' I_0 h}{c n_m \omega_0^2} \tag{4.10}$$

where α_p' is a real part of particle polarizability, I_0 is the maximum intensity, c is the speed of light, and n_m is the refractive index of the surrounding medium[248]. On the other hand, F_{vdw} for identical spherical particles at the similar separation distances ($h/a \ll 1$) is described by

$$F_{vdw} = -\frac{A_H a}{h^2} \tag{4.11}$$

where a is the particle radius and A_H is the Hamaker constant that is dependent on frequency-dependent dielectric functions of constituent of the system, representing the strength of van der Waals interaction between the particles with the surrounding medium[257, 258, 259].

To predict the assembly process of particles in a colloid, we must consider the forces between two particles. From here, we will assume that there is a stable particle at the center of the optical trap, and that the previous equations on the optical forces still apply to a separate particle not yet in the trap while there is a particle already trapped. This approximation does not take into account optical binding effects that may complicate the optical forces as the two particles approach[260, 261], but the effects will be complex due to the non-trivial morphology of the rough particles and such effects are beyond the scope of this experiment and the report of the assembly process. The forces presented above should be sufficient for an approximation of the rough order of magnitude for the effects observed in these experiments. Further work will focus on more complex modeling of all the forces in effect, especially including the optical forces. Assuming that a reference particle is at the center, we can define a cross-over separation distance, $\hat{h}$, from a competition between the two attractive forces F_{grad} and F_{vdw}. This competition leads to a cross-over separation distance of

$$\hat{h} = (\frac{A_H a}{\kappa_r})^{1/3} \tag{4.12}$$

where $\kappa_r \equiv 2\alpha_p' I_0 / c n_m \omega_0^2$. This cross-over distance is the separation distance where the van der Waals contribution to the attractive forces becomes the dominant force. Because the van der Waals forces become noticeable at $h \leq \alpha$ in general, $h \leq \alpha$ would be a necessary condition for the optical field driven attachment to take place. Therefore, the maximum distance we would expect van der Waals forces to overtake the optical gradient force and begin driving assembly would be at the limit of $h = a$. This leads to a minimum electric field intensity enabling the attachment,

$$(I_0)_{min} \approx \frac{A_H c n_m \omega_0^2}{2\alpha_p' a^2} \tag{4.13}$$

for a given fixed system (i.e. fixed α_p', n_m, and A_H). The simple scaling indicates that one needs to tailor both ω_0 and a to drive the attachment, having already determined the constituents of the system.

While the above physical rationale provides the feasibility of the coordinated interplay between two attractive forces leading to the attachment, it is insufficient to understand kinetics of the attachment and does not directly correspond to an attachment frequency. This can be understood by considering a generalized relation between velocity and force, as seen in equation 4.2. This can be generally conceived as $V = MF$ where V, M, and F denote a relative velocity, hydrodynamic mobility, and force between particles, respectively. This is all to say that the relative motion between the particles (involving a time scale for the attachment) is heavily influenced by the hydrodynamic mobility, in addition to the nature of the force. Considering a radially approaching motion in close proximity as a key step for attachment event, the most appropriate attractive force would be F_{vdw}. As pointed out, $F_{vdw} \sim O(\varepsilon^{-2})$ where $\varepsilon \equiv h/a$, representing a normalized separation distance. With F_{vdw} being the dominant driving force at these separation distances, we can use it as an approximation for the net force in velocity calculation at very small separation distances. The mobility scales as $M_{rough} \sim O(1)$ for the rough particle and $M_{smooth} \sim O(\varepsilon)$ for the smooth particle in the lubrication regime, $\varepsilon \ll O(1)$ as noted in figure 4.9.

This leads to different scaling in the relative particle velocity for rough and smooth cases; $V_{rough} \sim O(\varepsilon^{-2})$ and $V_{smooth} \sim O(\varepsilon^{-1})$. The scaling implies that a time scale associated with the approaching motion for the rough particle in close proximity (i.e. $\varepsilon \ll O(1)$) would be order of magnitude faster than that for the smooth particle, leading to the noticeable difference in probability of attachment events.

The coordinated interplay between the optical force (i.e., optical gradient force, F_{grad}) and short-ranged attractive force (i.e., van der Waals force, F_{vdw}), along with the delicate balance between hydrodynamic and van der Waals forces at close separations brings a unique system to enable identifying the importance of hydrodynamic forces in the assembly of nanoparticles. A similar case has been observed in aggregation of aerosols under turbulence where a driving force is the turbulent shear and non-continuum nature of gas brings a significant variation of hydrodynamic force, resulting in drastic difference in the aggregation of aerosols, analogous to the surface roughness in our study.[262]

Using the forces above, we simulated if two α-NAYF crystals in a set of optical tweezers would reliably come into contact with each other. Each particle had the velocity calculated and position adjusted according to that velocity when time was stepped. At each time step, the crystals positions were checked to see if they had come into contact. Contact events were binned and the results were plotted as a probability density function histogram in figure 4.10. Due to synthesis limits, we are unable to grow smooth and rough α-NAYF at identical sizes. Because of this limit, we ran simulations for smooth and α-NAYF at sizes they cannot normally be grown to control for size effects in driving contact, while keeping other parameters constant in the simulation. Adjusting for crystal size, a sharp increase in contact between crystals is observed for rough crystals in both size domains, as the predicted by the order of magnitude difference in the scaling of velocity at a close proximity. Of note, the rough spheres come into contact much faster on average compared to their smooth counterparts, independent of size effects which is in agreement with

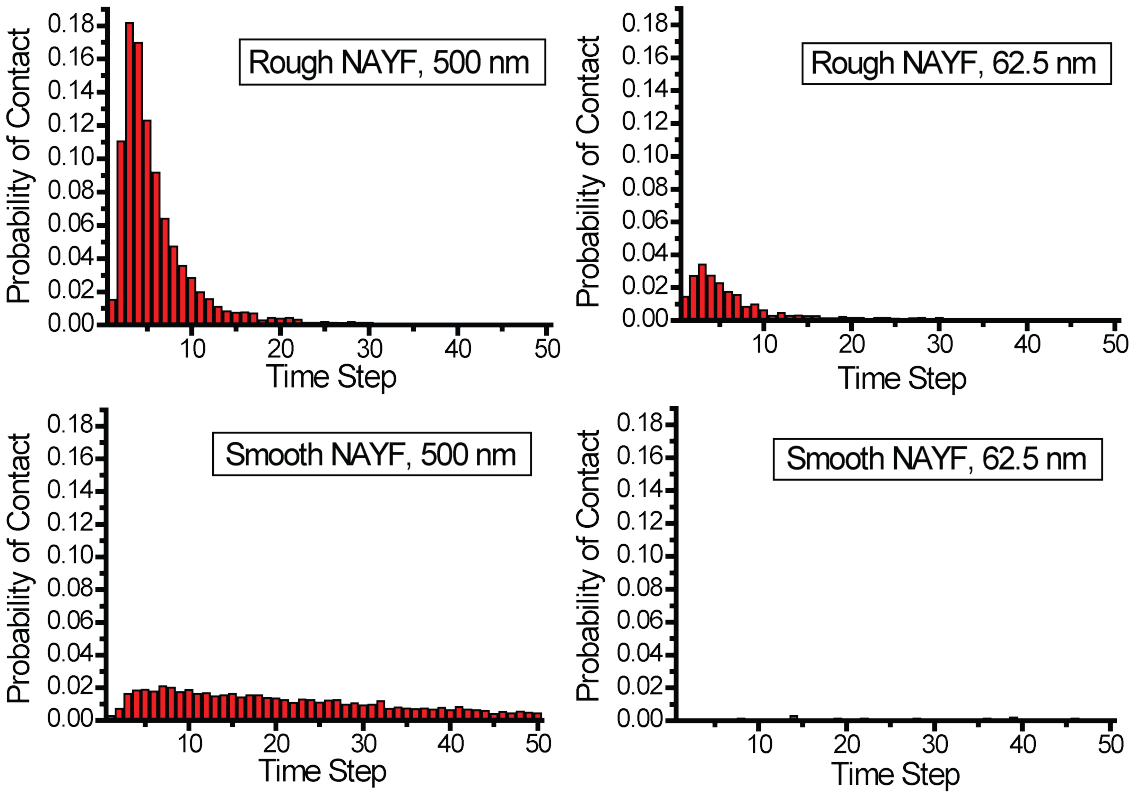

Figure 4.10: Probability density function for α-NaYF contact between two α-NaYF crystals in an optical trap. The roughness of the α-NaYF crystals dominate the probability of contact more than other variables, including crystal size. Comparitive sizes are plotted to demonstrate this point.

our expectations based off the scaling of velocity discussed above. The modeled probability functions match the empirical events observed in our optical tweezers, suggesting that the roughness of particles directly affects the probability of physical contact between two particles. The increased surface roughness directly affects the mobility of the colloidal crystals, allowing the rough particles to collide and assemble much faster and more frequently.

Chapter 5

ADDITIONAL WORKS: LASER REFRIGERATION AT THE EXTREMES AND PREPARATION OF QUANTUM DOT CAVITIES

Laser Refrigeration of Rare Earth Fluorides Under Extreme Conditions

Laser refrigeration not only has applications in optical tweezers, but it can also provide cooling in other systems where rapid cooling is difficult. Diamond anvil cells (DACs) are used to generate extreme pressures, but the diamond anvil cell itself blocks good thermal access to the samples being studies. There are thermoelectric coolers and heaters for DACs, but getting rapid responses is very challenging. Heating is fairly easy through photothermal heating. The use of a high powered laser will heat the sample extremely quickly, and it is fairly simple to create a feedback loop to heat to specific temperatures after calibrations. However, cooling is not trivial. If rare earth fluorides were added to the DAC, it may become possible to cool *in situ*, but it was not clear if laser refrigeration would work at extreme conditions until our experiments.

5.0.1 Understanding YLF Crystals at Extreme Pressures

Laser heating within a DAC has led to a range of significant advances towards the understanding of both the fundamental properties[263] and synthesis of materials at extreme conditions[264]. Since Takahashi & Bassett's original work in the late 1960s using laser heating to synthesize diamond from graphite [265], laser heating at extreme conditions has enabled scientists to study matter at conditions relevant to planetary interiors [266, 267] and synthesize a wide variety of new materials with unique phases and compositions [268, 269, 270]. Controlling the temperature within

DACs has also led to recent reports of metal-hydride materials with superconducting phase transitions near room temperature [271, 272, 273, 274].

In contrast to laser heating, solid-state laser refrigeration at extreme conditions has remained unexplored. The refrigeration of condensed phases was reported first in 1995 through the use of heavy metal fluoride glass[2]. During solid-state laser refrigeration, a material is refrigerated through anti-Stokes fluorescence [130]. A laser, with low optical entropy, excites electronic levels within ytterbium ions which then couple to optical phonons provided by the host lattice. This phonon-mediated excited-state upcoversion is followed by the spontaneous emission of high-entropy photoluminescence that transports heat away from the material[1]. The transition from amorphous glasses to crystalline ceramics such as Yb:YLF has had a major impact on the minimum achievable temperatures. Cooling from room temperature to cryogenic temperatures ($\sim$90 K) in vacuum has been demonstrated [275]. More recently, solid-state laser cooling in liquid water has led to the first experimental demonstration of cold Brownian motion [5] since Einstein's seminal 1905 paper on isothermal Brownian motion [276].

To date it has not been clear whether solid-state laser refrigeration is possible within a DAC due to the requirement for blue-shifted, anti-Stokes photons to escape and transport heat from the host material. Laser refrigeration within a DAC poses potential challenges for laser cooling considering the high optical index of refraction of diamond (n = 2.5), the metallic components of the DAC restricting the direction of emission, and the large conductive heat load, especially considering the contact with bulk diamond with high thermal conductivity. Additionally, high pressure phase transitions are known to occur for YLF [277, 278], which can lead to significant changes to the crystal-field (Stark) levels of lanthanide ions. In particular, increasing the splitting of the ground state manifold at high pressures could decrease the efficiency of phonon-mediated upconversion [130].

5.0.2 Use of a Diamond Anvil Cell to Measure Laser Refrigeration at High Pressure

Here, we report the first experimental demonstration of solid-state laser refrigeration of both individual Yb:YLF microcrystals and an ensemble of Yb:YLF microcrystals at pressures > 11 GPa, opening up new experimental possibilities for the rapid photothermal control of the temperatures of matter at extreme conditions. We observe that Yb:YLF in the scheelite phase cools > 20 K below room temperature at a pressure of ~ 4 GPa for both the single crystal and bulk. At pressures above 7 GPa, the tetratgonal scheelite phase undergoes a martensitic second order phase transition to a monoclinic fergusonite phase with increased crystal field splitting. Despite the phase transition, laser refrigeration > 5 K below room temperature is observed for the fergusonite phase for both the single crystal and bulk, opening up a new range of potential applications of laser cooling in high pressure science.

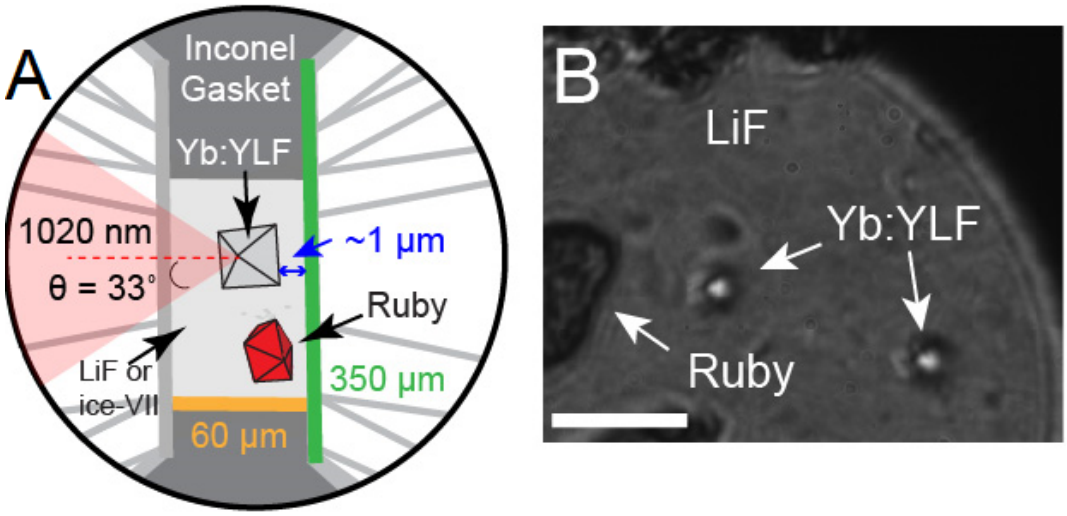

Figure 5.1: Experimental schematic of diamond anvil cell with YLF crystals A) An illustration of the diamond anvil cell chamber. Inside the chamber includes ruby, for pressure sensing, Yb:YLF, the sample, and finely ground LiF, the quasi-hydrostatic pressure medium. The critical angle of the microscope objective is denoted as θ. b) an optical micrograph of the DAC chamber. Components of the chamber are labeled in white. Scale bar is 10 μm

Two sets of experiments were performed inside a Merril-Basset and modified Bx90 type DACs to probe the Yb:YLF samples with increasing pressure (up to 12 GPa), as seen in Fig. 5.1. For the first set of experiments, single micro-grains of Yb:YLF were sealed within a LiF pressure tansmitting medium. The second set of experiments (seen in Fig. 5.4B&D) explore the optical refrigeration of approximately half of the DAC chamber filled with Yb:YLF micro-crystals, or a bulk sample set. To quantify the observed laser cooling in each set of experiments, temperature calibration was performed. As the pressure was increased, ruby was utilized to monitor the pressure and hydrostaticity of the DAC chamber, following procedures found in Chai and Brown.[279]. These procedures verified the DAC chamber was hydrostatic over all measured pressures. Therefore, any changes in photoluminescence spectra collected are due to compression only, not a nonhydrostatic environment.

The local environment of the scheelite Yb:YLF crystal contains a trivalent yttrium/ytterbium cation and a monovalent lithium cation coordinated by eight fluoride and 4 fluoride anions, respectively, as seen in Fig. 5.2. Under ambient conditions, the quasi-tetrahedral LiF_4^{3-} sub-unit has been characterized to have ionic bonding, which is more easily compressible than the Y/Yb-F bond [280, 281, 282, 283]. The point-group symmetry of the trivalent cation site is S_4. According to experimental [277, 278] and theoretical literature [283, 284, 285], as a YLF crystal undergoes compression in a hydrostatic environment, its phase changes from a scheelite phase (tetragonal, space-group $I4_1/a$) to a fergusonite phase (monoclinic, spacegroup $I2/a$), as seen in Fig. 5.2. The local symmetry of the trivalent cation site reduces to C_2 after the transition to the fergusonite phase. Raman and XRD pressure measurements [277, 278] place this phase transition pressure in a wide range pressures. Optical luminescence measurements of rare earth ions substitutionally doped into the yttirum site [277] have observed subtle reductions of local point-group symmetry at pressures above 10 GPa. Discontinuities in the phonon frequencies during Raman measurements, due to the stiffening of the LiF_4^{3-} bonds, indicated a structural phase transformation at 7 GPa

[281]. As previous papers have shown that photoluminescence from Nd and Eu ions can detect the transition from scheelite to fergusonite, we relied on these measurements for Yb, and the well known phase transition pressure of >10 GPa, to track the phase transition of our YLF crystals. Overall, the phase transformation from scheelite to fergusonite is slow with the major structural changes occurring at < 10 GPa. All studies showed a reversible transformation from the fergusonite phase back to the scheelite phase when going back to ambient pressures, which is corroborated by our measurements. Theoretical calculations have predicted these phase transitions can occur at a range of pressures between 5.5 GPa[286] and 9 GPa[287].

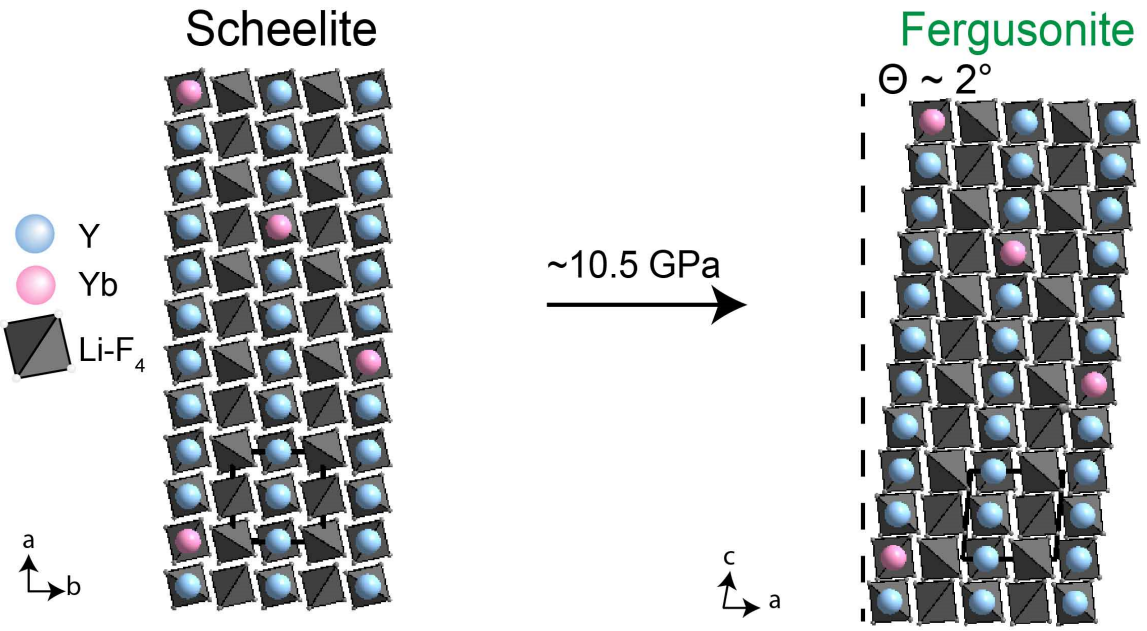

Figure 5.2: The phase transition of Yb:YLF from tetragonal Scheelite ($I4_1/a$, Z=4) to monoclinic Fergusonite ($I2/a$, Z=4). The small inset illustrates the local symmetry of the Y/Yb ion next to the 8 nearest F neighbors. The local symmetry is reduced from S_4 to C_2 when transitioning from scheelite to fergusonite, respectively

Figure 5.3 illustrates the fluorescence spectrum of a trivalent Yb^{3+} dopant in the YLF host crystal. Based on the crystal field interactions from the host lattice, the $^2F_{7/2}$ (ground state) and $^2F_{5/2}$ (excited state) spin-orbit manifolds are further split

into four and three Stark levels, respectively, giving a total of 12 possible transitions, as seen in Fig. 5.3B. The fluorescence peaks and their corresponding vibronic sidebands have been characterized by previous studies at low temperature and ambient pressure[288, 289]. From these studies, the energy transitions were derived based on the S_4 point group symmetry's reduced matrix elements and utilized to make predictions on the value of each energy level in the ground and excited state manifolds seen in Fig. 5.3B[289, 290].

5.0.3 Effects of Pressure on YLF Emission and Cooling

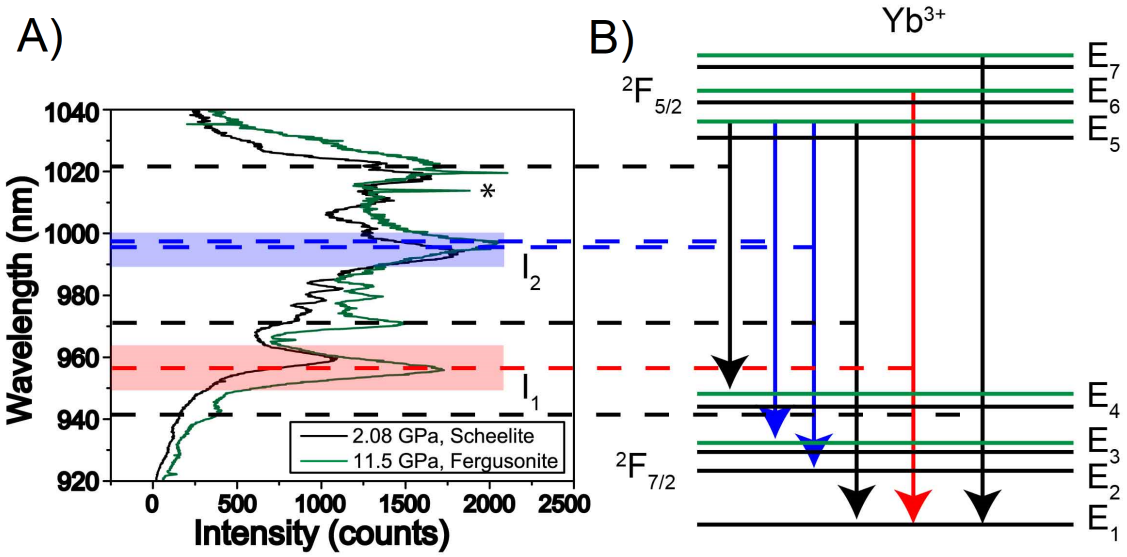

Figure 5.3: A) The full emission spectrum of Yb^{3+} ion at elevated pressure. The black line denotes the emission spectrum in the scheelite phase; the green represents the emission spectrum of the fergusonite phase. Key energy transitions are marked with a dashed line. The asterisk denotes a cosmic ray. B) The Stark manifold of the Yb^{3+} ion. The key energy transitions denoted in A) are matched to their respective energy levels in the manifold. The energy transitions in blue and red represent the levels used for Boltzmann ratiometric thermometry analysis.

Increasing the pressure with the DAC is observed to have a significant impact on the crystal field levels for Yb ions in the YLF host matrix. The black line in the

emission spectrum of Fig. 5.3A represents the emission when the scheelite phase is at elevated pressure (2.38 GPa) and the green line represents when YLF has already transitioned to the fergusonite phase (11.5 GPa). Overall, changes between the PL spectra clearly illustrate that the crystal field is being modified by the increasing strain. At a pressure of around 6 GPa, a prominent new luminescence peak at a wavelength of ∼970 nm (Fig. 5.3A), indicating the preliminary onset of the martensitic phase transition. Previous studies [291] have linked the point group symmetry of a rare earth doped fluoride scheelite with its ligand field Hamiltonian to calculate its vibronic intensity parameters. Modification of the rare earth ion's point group symmetry with pressure can alter its surrounding ligand field and thus alter the intensities of is electronic and vibronic transitions, as can be seen in the E_5-E_1 transition ($\lambda \approx$ 970) in Fig. 5.3A.

Figure 5.3B depicts the change in energy of the key transitions. This change in energy was measured at various pressures. The fluorescence peaks were based upon the fluorescence peaks at ambient conditions from Delic *et al.* (2004) [288]. As the spectra were fit at increasing pressures, the absolute energies of each level in the $^2F_{7/2}$ and $^2F_{5/2}$ manifolds were calculated based on the fitted energy transitions. These calculated energies were then checked with the E_7-E_1 energy transition, even as it blue shifted with increasing pressure.

The trends in energitc shifts depict discontinuities at approximately 6 GPa, which normally indicates a phase transition. As stated in the literature, the phase transition to fergusonite is observed at 10.5 GPa, but fluorescence experiments utilizing other RE ions show subtle structural changes as low as 5.5 GPa. The discontinuities at 6 GPa therefore illustrate similar trends. The most striking of the energy transition trends measured are the E_7-E_1, the E_6-E_1, and the E_5-E_1 transitions, illustrating an increasing energy as the pressure is increased with slopes of 5.3 ± 0.3 $cm^{-1}GPa^{-1}$, 4.3 ± 0.2 $cm^{-1}GPa^{-1}$, and 2.0 ± 0.4 $cm^{-1}GPa^{-1}$, respectively. Even though the individual E_5-E_4 transition demonstrates a clear red shift in energy, with a slope of -2.9 ± 0.4

$cm^{-1}GPa^{-1}$, overall the energy levels in the manifold are increasing. Subtle structural changes to the YLF host crystal, due to the increasing pressure, reduce the local symmetry of the Yb ion bonded to the LiF_4 tetrahedron to C_2.

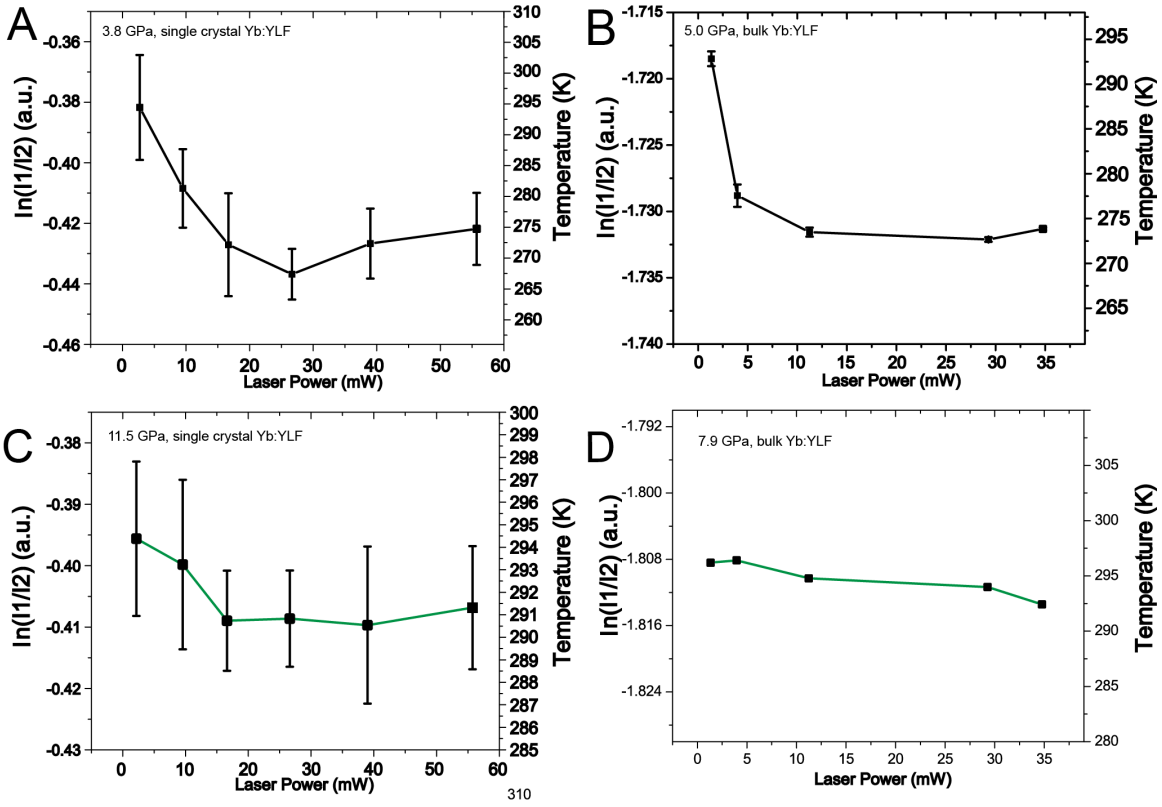

Figure 5.4: Optical Refrigeration of YLF at Extreme Pressures. Yb:YLF particle in the A&B) scheelite and C&D) fergusonite phase at varying pressures. Error bars represent the standard deviation of six separate measurements at each laser power.

Figure 5.4 demonstrates the first measurements of solid-state laser refrigeration for the scheelite phase of YLF at various elevated pressure conditions for both the single crystal and bulk experiments. Ratiometric luminescence thermometry was utilized to measure the temperature trend of a Yb:YLF crystal inside a diamond anvil cell chamber based on the Boltzmann distribution of thermally accessible states. Two fluorescence peaks are chosen for integration, the E_6-E_1 and E_5-$E_{2,3}$ transitions, as

seen in the blue and red shaded regions in Fig. 5.3A. When the laser power is varied, it is observed that the integrated photoluminescence intensities of these two peaks change based on the internal temperature of the host crystal. As the internal temperature of the host crystal decreases, so does the probability of Yb-ions accessing higher energy configurations, which is reflected in the photoluminescence intensity. Under these circumstances, it is expected that the integrated ratio between the aforementioned emission transitions will also decrease. This trend is illustrated for the scheelite phase in Fig. 5.4A&B. After temperature calibration, the decreasing ratio between the two peaks could be used to quantify the temperature. A temperature decrease of approximately 20±5 K below room temperature was determined for the single YLF particle in the scheelite phase at 3.8 GPa (Fig. 5.4A). This temperature change is consistent with numerical finite element simulations. Figure 5.4B also demonstrates the potential to refrigerate the bulk scheelite phase, as the ensemble was observed to cool approximately 17.0±1K below room temperature at a pressure of 5.0 GPa, immediately preceding the onset of the martensitic phase transition. One potential explanation for the smaller net cooling of the bulk sample is re-absorption from adjacent grains of Yb:YLF.

As discussed above, many of Yb^{3+} Stark manifold energy levels are modified with pressure. In particular, the E_5-E_4 energy level red shifts as it enters into the fergusonite phase. This has major implications on the net cooling of Yb:YLF as the incident excitation of 1020 nm is no longer exactly resonant to this transition. Because the incident source is more energetic, anti-Stokes fluorescence still occurs, however, a reduction in the magnitude of cooling is observed (Fig. 5.4C&D). For both the single crystal and bulk sample of Yb:YLF, the calibrated magnitude of cooling is much lower for the fergusonite phase than for the scheelite phase, with the former cooling by approximately 4K and the latter cooling by approximately 1.96 K. As what was seen with the scheelite phase, there is a lower net cooling between the single crystal and the bulk sample.

5.1 Preparation of Quantum Dot/Chalcogenide Cavities through Pulsed Laser Deposition

In addition to work on rare earth fluorides, I also worked on the generation of quantum dot/chalcogenide cavities using pulsed laser deposition (PLD). Quantum dots (QDs) contain remarkable emissive properties, but it is challenging to isolate single QDs into cavities for further study. Our work focused on producing a large amount of such cavities through quick and cost-effective manufacturing techniques like PLD. However, it was not clear if the QDs would survive the deposition process. We used CdS films to coat the QDs and measured the optical properties after deposition.

5.1.1 Importance of High-Efficiency Single Photon Microcavity Systems

High-efficiency single photon sources are extremely promising candidates for advances in quantum information and quantum communications systems.[292, 293, 294] Single photon sources have been generated using quantum dots dispersed into microcavities,[295, 296, 297, 298, 299] and work has been done to expand the sources into tunable ranges[300] and other light frequency ranges, such as the UV region.[301] These methods could be improved by the use of gentle processing techniques to allow for the generation of high-efficiency single photon sources without the expenses and difficulties traditionally associated with epitaxial growth of semiconductor films. Some gentle processing techniques do exist, but require the use of chemical precursors that may not match the exact system requirements, especially in matching material properties.[302, 303] These systems represent advances in the means to prepare single photon microcavities, but they are not necessarily applicable to all systems. This leads to a need for more processes to match the exact needs of the system.

One process that could be used for generating these cavities is pulsed laser deposition. PLD generates a film by the use of a laser to induce vaporization of a target medium into a vapor or plasma plume that strikes a substrate, where the vapor or

plasma condenses into a film. The use of PLD to generate films with embedded QDs as a single photon source has been demonstrated by Aubret et al.[304], making PLD a highly valuable technique to produce such cavities for quantum information sciences. This work is highly motivating in using PLD to generate single photon microcavities for quantum information systems in a scalable and inexpensive process. However, more work needs to be done to expand the set of media possible shown to be usable in producing single photon microcavities and to characterize the effect PLD on the quantum dots. While the emission can be preserved and single photon sources can be found, more data is needed to substantiate that the process is entirely non-destructive. Quantitative analysis of film composition and quantum dot emission and lifetime is necessary to understand the effect of the PLD plasma on the QDs.

Here, It is shown that it is possible to produce semiconductor dichalcogenide cavities of CdS with sub-monolayer dispersions of CdSe/CdS quantum dots through PLD. CdS was chosen as the cavity medium to match the refractive index of the shell of the QDs for optimal coupling of the emission of the QDs to the cavity. The structure and roughness of the films grown are characterized and the emission of the QDs are studied prior to and after deposition inside the cavity to detect if the PLD process is gentle enough to prevent damage to the QD luminescence. Composition analysis of the film is studied with atom probe tomography (APT) to detect any contaminants from possible QD breakdown during the PLD process, as APT is particularly suited finding spatial composition variance in heterogeneous samples.[305] Also presented are calculations of the effect of cavity CdS material on the radiative and non-radiative lifetimes of the QDs inside the cavity to account for possible effects on the QD luminescence.

5.1.2 Manufacturing and Design of the Cavity

The CdS thin films used to encase the QDs were deposited via PLD. A 1 cm^2 silicon wafer was attached to the center of a larger silicon substrate with copper tape for mounting in the vacuum chamber of the PLD instrument. The vacuum chamber was

pumped to 2×10^{-6} torr and held at that pressure for 30 minutes. No heating was applied to the silicon substrate as the heating could lead to defect luminescence in the CdS films that overlaps with the QDs. A 250 nm thin film of CdS was then deposited onto the silicon wafer, and the wafer was transferred to a glove box for it to receive a coating of QDs.

The QDs were dispersed in a sub-monolayer coating on the first CdS thin film deposition. The QDs were drop-cast onto the thin film inside of a glove box to prevent damage from oxygen and water in standard atmospheric conditions. The QD solutions were diluted to a concentration of 24 nM in hexane as measured by UV-Vis absorption measurements. 20 μL of the diluted QD solution was then drop-cast onto the CdS film and allowed to dry fully. The thin film was then transferred to the PLD instrument for the deposition of the second CdS layer.

The layered sample was transferred to an FEI Quanta dual beam focused ion beam-scanning electron microscope (FIB-SEM). We attempted to find evidence of quantum dots via visible bumps on the surface. A Pt capping layer was deposited on the surface over these bumps to protect the material from Ga ion damage during the milling process, and a cantilever was lifted out and serially mounted onto silicon microposts and sharpened into needles via standard methods found in the literature.[306]

APT was performed on a Cameca LEAP 4000X-HR instrument with a picosecond 355 nm UV laser. The specimen was cooled to 45.2 K at a vacuum pressure of 9.3×10^{-12} torr. The laser pulse energy was set at 40 pJ for the first approximately 750,000 counts and then reduced to 20 pJ. 888,422 ions were collected in total, after which the tip fractured, ending the run. The data were analyzed using Cameca's Integrated Visualization and Analysis Software (IVAS), and the tip profile was constructed based on an SEM image of the sample.

In order to understand the electronic structure of the CdSe/CdS core/shell quantum dots, density functional theory (DFT) calculations were performed using the Gaussian electronic structure software package [307] with the Perdew, Burke, and

Ernzerhof hybrid functional (PBE0) [308, 309] and the LANL2DZ pseudopotential and associated basis functions.[310, 311] A pseudo-hydrogen capping scheme is applied in order to terminate surface dangling bonds and compensate surface ions, which results in the $(CdSe)_{33}H_{60}$ as the core (diameter $\sim$ 1.04 nm). To examine the effects of shelling on the photoluminescence properties, CdSe/CdS core/shell structures were constructed by adding on one and two layer of CdS shells around the CdSe core structure following the same symmetry, respectively (diameter $\sim$ 1.61 nm for 1-layer and $\sim$ 2.02 nm for 2-layer structure). Geometries were considered optimized when both the forces (maximum and RMS force, 0.00050 and 0.000300 Hartree/Bohr, respectively) and displacement (maximum and RMS displacement, 0.0018 and 0.0012 Bohr, respectively) for all atoms were below the threshold criteria. This level of theory has been shown previsouly to match well with experiment for similar systems.[312, 313] The absorption and emission spectra of the quantum dots were computed through time-dependant DFT (TDDFT) within the linear-response framework. [314, 315, 316] Energies and oscillator strengths are computed for the lowest four excited states of all three QD structures as well as the ground-to-excited-state non-adiabatic coupling, to provide insights into the radiative and non-radiative decay of the QDs.

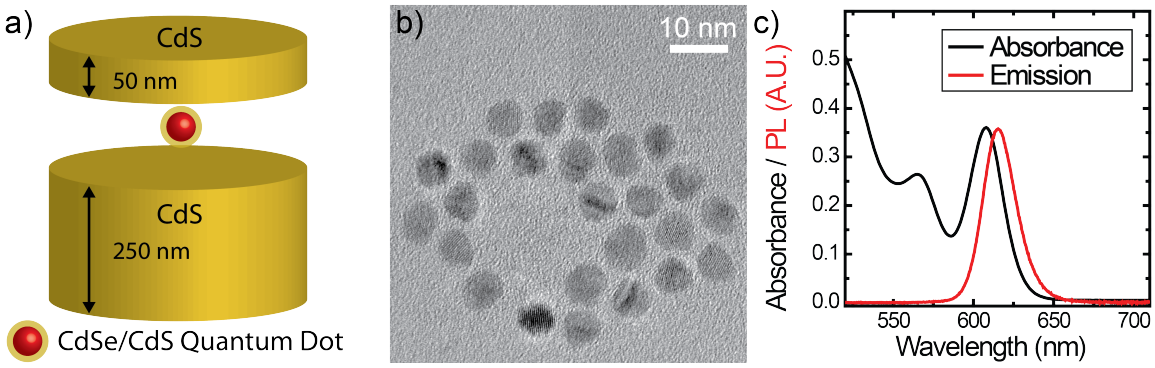

Figure 5.5: a) Schematic of thin-film device made by depositing 250 nm of CdS onto a silicon substrate, coating a sub-monodisperse layer of CdSe/CdS quantum dots onto it, then layering again with 50 nm of CdS. b) TEM image of 6.9 $\pm$ 0.6 nm CdSe/CdS quantum dots. c) Absorbance and photoluminescence of CdSe/CdSe quantum dots.

We formed a thin film cavity of CdS, within which CdSe/CdS QDs were dispersed. A schematic of the cavity structure can be seen in figure 5.5a. The thin-film bilayer cavity was formed via PLD of CdS onto a silicon substrate. After a deposition of 250 nm of CdS, the thin film was removed from the PLD vacuum chamber and a sub-monolayer of CdSe/CdS QDs was coated onto the surface of the thin film. The QDs had an average size of 6.9 nm (fig 5.5b). After vacuum drying to remove excess organic solvent, the thin film was reintroduced into the PLD vacuum chamber and an additional 50 nm of CdS was deposited on top of the CdSe/CdS QDs.

5.1.3 Analysis of Cavity Uniformity and Composition

The surface of the thin film cavity showed significant roughness via both SEM (fig 5.6a) and atomic force microscopy (fig 5.6b). We believe this to be due to poor crystal lattice matching between the CdS and the Si substrate, leading to polycrystalline or amorphous CdS being deposited on the Si substrate and uneven growth of the CdS crystal grains. In addition to the uneven surface, some bubble-like protrusions could be seen on the surface. We suspect that these arise from increased growth around the QDs. As CdS is deposited on the outside of the dots, the CdS grows isotropically around the dots leading to a semi-spherical growth around the dot. This structure expands as the top layer is deposited, resulting in the final protrusions observed. We inspected these cross-sections of these regions with TEM to observe the QDs embedded inside of the cavity device (figure 5.6c&d). A significant separation of the layers could be seen. EDS analysis suggests that this separation is caused by a layer of carbon, which could be caused by insufficient removal of the organic solvent from the QD coating. Under close inspection, we observed that the region we expected to find a QD had a gap in the film that may have once held a QD prior FIB etching, but we were unable observe it. The gap in the thin film layers contains a large amount of carbon and is wide enough to have held a QD, though no direct evidence of a QD was observed.

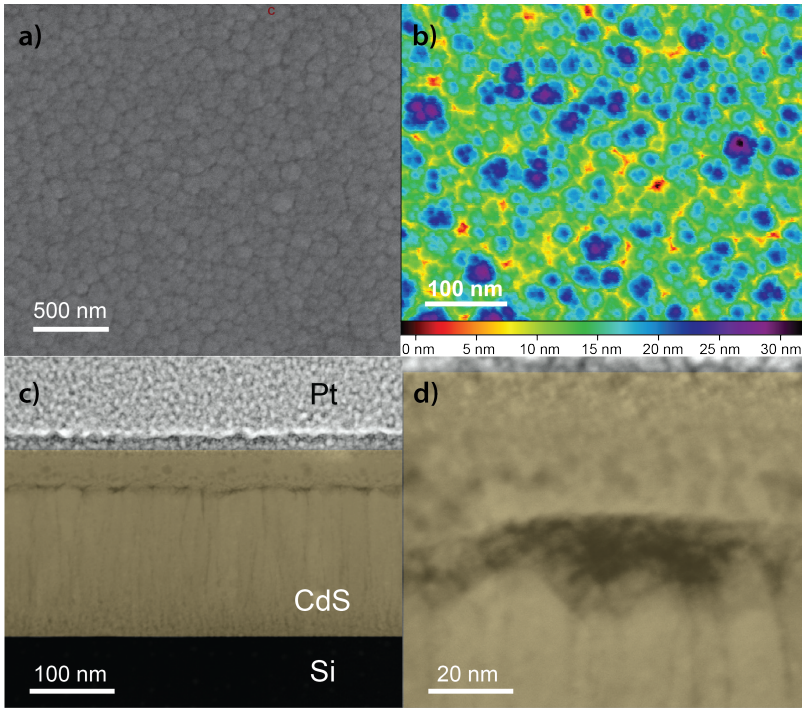

Figure 5.6: a) SEM micrograph of the top CdS surface of the thin-film device. The surface has a textured pattern approximately 50 nm in size. b) AFM image of the top CdS surface showing variations in height of approximately 25 nm between height extrema. c) and d) Cross-sectional TEM micrographs of the thin-film device. Contrast between the bottom and top CdS depositions can be seen. d) shows a small pocket between the layers where a quantum dot may have been located. Color overlay has been added to (c) and (d) to mark the approximate boundaries between the CdS and Pt.

We performed atom probe tomography (APT) on a sharpened tip made from the bilayer (Figure 5.7A). APT was performed on a Cameca LEAP 4000X-HR instrument with a picosecond 355 nm UV laser. The specimen was cooled to 45.2 K at a vacuum pressure of 9.3^{-12} torr. The laser pulse energy was set at 40 pJ for the first approximately 750,000 counts and then reduced to 20 pJ. A total of 888,422 ions were collected, after which the tip fractured, ending the run. The data were analyzed using Cameca's Integrated Visualization and Analysis Software, and the tip profile was constructed based on an SEM image of the sample. Due to difficulties in locating

the small 6 nm QDs under the 100 nm layer of CdS deposited on top, we were not able to isolate a tip that included a QD internally; however, we did observe a diffuse distribution of selenium within the CdS matrix (Figure 5.7B). The selenium does not appear to be localized within the tip and there is no reconstructed area that has more selenium than sulfur, which indicates that we did not capture a CdSe particle within the tip. However, the selenium concentration in the tip was measured to be roughly 1.4% of the total chalcogenide concentration and was clearly visible above the level of noise, which may indicate the vaporization and resputtering of some of the QDs during the PLD process.[317, 318, 319] The APT measurement was cut short due to a tip fracture. Immediately preceding the tip fracture, we observe a a large increase in the relative carbon concentration (Figures 5.7B). This carbon likely comes from the toluene and hexane solvents used to cast the QDs, and the increase in concentration near the fracture point suggests that the tip most likely fractured at the interface between the two CdS layers. This is expected based on the visible interface in figure 5.6c&d and serves to illustrate the difficulty in epitaxial growth using PLD, especially when potential contaminants such as organic solvents are present at the interface.

5.1.4 Modeling and Measurement of Quantum Dot Luminescence

To understand the electronic structure of the CdSe/CdS core/shell QDs, DFT calculations were performed using the Gaussian electronic structure software package [307] with the Perdew, Burke, and Ernzerhof hybrid functional (PBE0) [308, 309] and the LANL2DZ pseudopotential and associated basis functions.[310, 311] A pseudo-hydrogen capping scheme is applied in order to terminate surface dangling bonds and compensate surface ions, which results in the $(CdSe)_{33}H_{60}$ as the core (diameter $\sim$ 1.04 nm). To examine the effects of shelling on the photoluminescence properties, CdSe/CdS core/shell structures were constructed by adding on one and two layer of CdS shells around the CdSe core structure following the same symmetry, respectively (diameter $\sim$ 1.61 nm for 1-layer and $\sim$ 2.02 nm for 2-layer structure). Geometries were

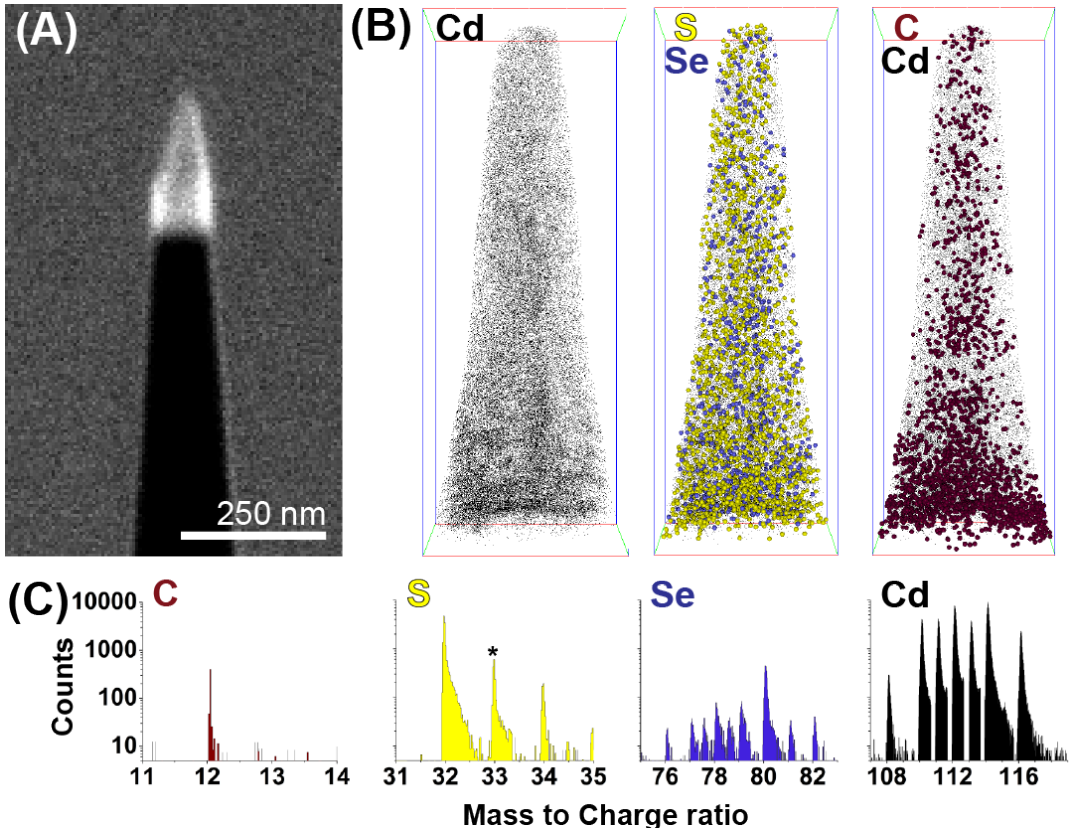

Figure 5.7: A) SEM image of the sharpened tip. This tip was used to generate the data in (B), which show the three-dimensional reconstruction of the tip up to the point of its fracture, highlighting the distributions of cadmium, chalcogenides, and carbon. (C) shows the mass spectra of the various species reconstructed in (B). There is some peak convolution present, as evidenced by the high apparent ^{33}S content. This peak, marked with an asterisk, indicates the presence of S_2^{2+}, specifically ^{32}S-^{34}S molecules.

considered optimized when both the forces (maximum and RMS force, 0.00050 and 0.000300 Hartree/Bohr, respectively) and displacement (maximum and RMS displacement, 0.0018 and 0.0012 Bohr, respectively) for all atoms were below the threshold criteria. This level of theory has been shown previously to match well with experiment for similar systems.[312, 313] The absorption and emission spectra of the QDs were computed through time-dependant DFT (TDDFT) within the linear-response framework. [314, 315, 316] Energies and oscillator strengths are computed for the

lowest four excited states of all three QD structures as well as the ground-to-excited-state non-adiabatic coupling, to provide insights into the radiative and non-radiative decay of the QDs.

The PL of the QDs were compared before and after the formation of the CdS thin film cavity. The PL was excited by a 532 nm single longitudinal mode laser. Nearly all PL was observed from a peak at 618 nm. This peak was preserved after the deposition of the CdS film on to the QDs (figure 5.8a). Careful control of the deposition parameters is needed to avoid CdS defect luminescence at 570 nm. The preservation of the QD PL after the deposition of the CdS suggests that the QDs survive the plasma generated by the PLD process and can still be used for optical measurements, but this does not inform us about in any damage at all has occurred.

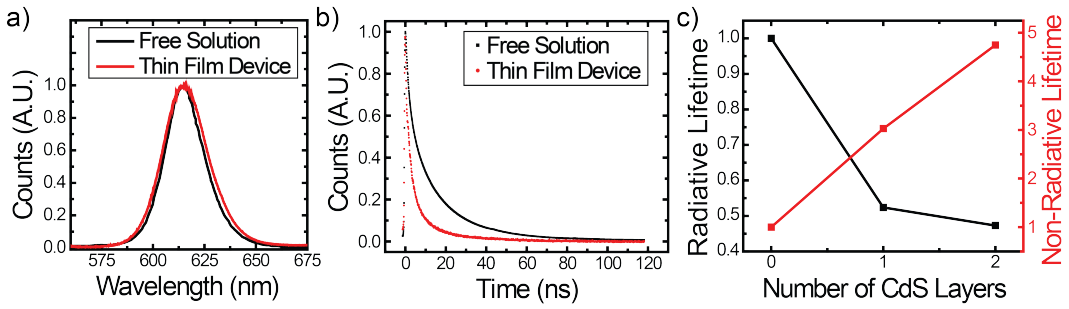

Figure 5.8: a) Photoluminescence from CdSe/CdS quantum dots in free solution and after incorporation into the CdS thin film device. CdSe/CdS quantum dot luminescence defect luminescence is preserved throughout the CdS deposition process, though some slight broadening and red-shifting is observed. b) Time-resolved PL lifetime decay curves of the CdSe/CdS quantum dots in free solution and in the thin-film device. c) Calculated radiative lifetime (black) and non-radiative lifetime (red) as a function of CdS shell thickness in CdSe/CdS quantum dots, using linear-response TDDFT method with the PBE0/LANL2DZ basis.

While the PL of the dots is preserved after the deposition of CdS, the lifetime of the PL is greatly shifted (figure 5.8b). While in free solution in toluene, the QDs have a lifetime of 17 ns while the QDs in the CdS thin film have lifetimes on the order of 1 ns.

Some of this lifetime shift can be explained by the proximity of the quantum dots to a planar dielectric interface.[320, 321, 322] It is established that the radiative lifetime of an electric dipole transition can significantly decrease as it approaches a planar dielectric or metal interface if the interface has an index of refraction greater than one while the separation distance is much less than the wavelength of light. This effect is due to increased radiative contributions from evanescent waves at short separation distances from an interface. The exact shift in lifetime is dependent on the index of refraction of the dielectric interface. The close proximity of the CdSe/CdS QDs in our experiments to the CdS cavity does account for some of the decrease in lifetime, but the refractive index for CdS (approximately 2.5 for the emission wavelength of the QDs) could not account for the shift of more than an order of magnitude observed experimentally. The calculations performed by Lukosz and Kunz[320] would predict no more than a shortening of the lifetime by a factor of approximately 3 for the index of refraction of our material at very close distances. While this effect does account for some of the shortening of the lifetime, it cannot account for all of it.

A large decrease in the non-radiative lifetimes could be explained by plasma-induced damage to the quantum dots during the deposition process. Additionally, the observed carbon in between the CdS layers may have come from the breakdown of the surface ligands on the quantum dots. This would explain the increased amount of carbon near the cavity layer interface where quantum dots are expected to be found. If the ligands are indeed being damaged and deposited as carbon, then non-radiative decay lifetime of the quantum dots will shorten considerably. This could explain the net shift in tandem with the dielectric interface explained above.

Another explanation for the shift in lifetime is increased effective layer of the CdSe/CdS QDs by additional CdS in the thin film surrounding it. TDDFT calculations predict that increasing the number of CdS layers around a CdSe QD will decrease the radiative lifetime while significantly increasing the non-radiative lifetime, as seen in figure 5.8c.

Upon the CdS shell addition, the bandgap for the QD has little change as shown in the density of states analysis of the core structure and the shelled structure, which agrees with the experimental photoluminescence spectrum in Figure 5.8a. However, the presence of the CdS shell leads to a significant contribution by S in the valence band, which shows that the wave function penestrates into the shell. It is supported by the leaving and arriving natural transition orbitals for the first bright transition for the core and shelled structures. Oscillator strength quantifies the rate of radiative decay between the excited states and the ground states. TDDFT calculations predict that increasing the number of CdS layers around a CdSe QD will decrease the radiative lifetime, supported by the increase of the oscillator strength ($\sim$ 2 times). Noted that for the CdSe core structure, the lowest excited state from the linear response TDDFT calculation is an optically "dark" state, which may result in an increased radiative lifetime due to the rapid equilibrantion of the population. [323] The computed non-adiabatic coupling term [324] decreases with the addition of the CdS shells.

Following the relationship between the nonadiabatic transition rate and the nonadiabatic coupling strength based on Fermi's golden rule in Ref. [325], the non-adiabatic decay rate decreases with the number of CdS shells. The observed decay time is related to the sum of radiative and non-radiative rates, $\tau_{obs} = (k_{rad}+k_{nonrad})^{-1}$. Considering that the radiative decay is more dominant [323] (Here needs more reference or experiments as evidence), the orserved lifetime is mainly affected by the radiative decay rate, which matches with the experimental observation. (Non-adiabatic decay is more complicated in actual experiment, I am not sure if we want to have the previous statements here.) In all, TDDFT calculations suggested that the quantum yield ($\Phi = \frac{k_{rad}}{k_{rad}+k_{nonrad}}$) of the CdSe/CdS core/shell structures increases with shell thickness.

It is unclear how the shortened radiative lifetime from increased evanescent wave contribution to a dielectric interface would couple with the TDDFT calculation predictions of shortened radiative lifetime with increased CdS layers. In the best case,

if they combine linearly, they would still likely not yet reach an order of magnitude effect shortening of the radiative lifetime. Since the drop in lifetime was slightly more than an order of magnitude, the non-radiative component of the lifetime must have shortened as well. The increase in CdS layers was not predicting a decrease in non-radiative lifetime from the TDDFT calculations. This leaves the most probable cause being the damage of the QDs during the PLD process from the plasma. If this is the case, then additional steps and precautions must be taken to preserve the luminescent properties of the dots if the goal of single photon cavities is to be reached.

Chapter 6

CONCLUSIONS

The large body of my work has been on the synthesis of NaYF for laser refrigeration applications. In chapter 2, I discussed a new method of hydrothermally synthesizing β-NaYF with precise control over the aspect ratio and demonstrated that β-NaYF made by this synthesis can be cooled by 1020 nm laser illumination to 12.5 °C below room temperature. By varying the ratio of fluoride ions to trivalent cations (Y^{3+}, Yb^{3+}) from stoichiometric values to double the fluoride concentration, we can reliably tune the β-NaYF crystals from microplatelets to microprisms to microrods. These crystals upconvert near-infrared light and emit blue-shifted light, which cools the crystal. We have measured this cooling via noncontact optical thermometry based on both ratiometric Boltzmann analysis of photoluminescence and eigenfrequency analysis of a device consisting of a β-NaYF microplatelet suspended on a CdS nanoribbon acting as a cantilever. Both methods of thermometry indicate a cooling of the β-NaYF device. β-NaYF materials made with this synthesis have particular applications in the observation of mesoscopic-scale quantum effects as a cavity resonator. We also observe that the β-NaYF from this synthesis is useful as a NIR-to-visible upconversion phosphor as demonstrated through experiments involving codoping with Er^{3+} and Tm^{3+} ions. Future work with β-NaYF using this synthesis will include the demonstration of cooling enhanced by morphologically dependent resonances, the manufacturing of optically cooled optomechanical mirrors and devices, and integration of β-NaYF with two-dimensional (2D) materials such as graphene and transition-metal dichalcogenides.

Chapter 2 also discusses the nucleation and formation of NaYF from its aqueous

precursors. Crystal nucleation and growth are often described based on the simple addition of monomer units from solution. The concept of nonclassical crystal growth adds further nuance to this view, allowing for the possibility of growth via different pathways and subsequent structural changes. We add to this view the observation of profound compositional changes that occur as an essential part of a nonclassical crystal growth process. We have shown that upon the mixture of NaF and YCl_3 in water, a gel separates from solution which then undergoes crystallization, similar to many other two- or three-step crystallization systems, and then undergoes a process of solid-state diffusion, where the product initially resembles amorphous YF_3 but then undergoes a gradual change of chemical stoichiometry inducing the crystallization of cubic NaYF over the course of several hours. It is rational to expect that this multi-step mechanism is not limited to NaYF in particular, and as such more research is needed into other chemical systems, and particularly those which exhibit nonstoichiometry, as to the inherent role of solid-state compositional changes in their crystal nucleation and growth pathways. This also motivates further research into the atomistic detail of these reactions, for example considering surface reconstructions[326] or studying the atomic-scale physics of the incorporation of sodium ions into the amorphous intermediate.

Next, we explore cooling of external loads through laser refrigeration in chapter 3. Specifically, we focus diamonds and nanodiamonds. The indirect laser refrigeration of nanodiamond quantum sensors via van der Waals attachment to ceramic laser-cooling microcrystals is possible both in vacuum and atmospheric pressure. We use complementary non-contact thermometry methods (both DWF and ODMR) to demonstrate solid state laser refrigeration as a rapid (ms) approach for controlling the temperature of nanoscale quantum materials near room temperature. A 27 K drop in the internal temperature of the NDs was measured in vacuum. This allows for the stabilization of thermal spectral wandering of the NV^- ZPL by tuning the 1020 nm intensity. Laser refrigeration of NDs will enable rapid feedback temperature control of quan-

tum materials for a wide range of quantum sensing and communication applications. These results may also enable new experimental possibilities in quantum information science including single-beam laser trapping[327, 328, 329], precision sensing of temperature,[103] magnetic fields,[330] dark matter,[109] and quantum gravity.[111]

Following the cooling of nanodiamond attached to YLF, we tested the viability of cooling bulk diamond through anti-Stokes luminescence from the H3 defect in diamond. This defect can be formed through rapid thermal annealing, which combines substitutional nitrogen centers and NV centers, both of which will induce heating. By removing these defects and generating H3 defects, we reduce the photothermal heating in bulk diamond, going from approximately 50 K of heating in an NV rich diamond to only 5 K of heating in the H3 rich diamond. This is despite the fact that significant NV defects still remain in the H3 enriched diamond, which will induce heating. Should further refinement develop, it may even be possible to undergo true laser refrigeration and cool diamond below room temperature in an all-optical process, both for bulk diamond materials and for nanodiamonds acting as quantum sensors.

In Chapter 4, we explore the use of optical tweezers to spatially isolate and study NaYF. We have demonstrated that α-Yb:NaYF nanocrystals can cool using anti-Stokes emission to 241 K when the Yb^{3+} ions are excited using 1020 nm light. The cooling achieved depends on the pressure of the surrounding gas; lower pressures lead to less cooling as the crystal heats due to absorption from the trapping laser by ligands on the surface of the crystals. The ability to cool the crystal lattice of trapped nanocrystals allows for trapping nanodiamonds with NV centers at lower pressures and adjusting the temperature of a nanocrystal in real time to stabilize temperature variations of a trapped crystal. Future work will include trapping crystals with no surface ligands to increase cooling capacity at lower pressures and using laser refrigeration and rare earth-doped crystals to cool trapped nanodiamonds with NV centers.

In addition to cooling of α-NaYF in NaYF, I also discuss the first optical trapping

of high aspect ratio Yb-doped β-NaYF hexagonal prisms, and compare the observed dynamics to a numerical model. For these prisms or other disc shaped sensors, the figure of merit η for sensitivity to gravitational waves significantly improves upon other spherical levitated systems both in the gas damping limited regime and the photon recoil heating limited regimes. NaYF has been shown in other experiments to exhibit anti-Stokes fluorescence cooling, when illuminated with light of a suitable wavelength. Quasispherical nanocrystals with irregular morphologies prepared through top-down milling have also been cooled while being optically levitated[222]. Laser refrigeration of optically levitated disclike objects could allow higher trapping intensities and frequencies, yielding higher sensitivity to gravitational waves well above 100 kHz. Transferring these prisms, or objects of a similar geometry, into a Michelson-type 1 meter cavity instrument represents a next step in the technical road map of the Levitated Sensor Detector[204]. The successful trapping of these high aspect ratio hexagonal prisms therefore represents a significant step forward in developing > 10 kHz gravitational wave astronomy.

Additionally in chapter 4, I discuss the optically-driven assembly of α-NaYF single crystals in water into a linear chains that persist for an indeterminately long period of time. This assembly is counter-intuitive, yet can be reliably induced through the use of optical tweezers for rough α-NAYF crystals. The assembly appears to be enabled by the surface roughness of the α-NAYF crystals, which directly reduces the hydrodynamic repulsive force experienced when two colloidal crystals come into close proximity. This is confirmed by simulations that demonstrate that the probability of particles coming into physical contact in an aqueous system in directly affected by the roughness of the particles.

The roughness of the surface causes an asymptotic limit to the hydrodynamic repulsion forces on the particles, which appears to be a primary limiting factor in direct contact between two objects in solution. This has major impacts on any system that involves the contact of two bodies in an aqueous system, and could potentially

have explanatory power in systems such as non-classical crystal growth dynamics or surface protein morphology in viruses and microorganisms. When used in conjunction with novel 3D tracking[331], the exact dynamics of complex systems could be mapped out in real time. The attachment method itself has direct applications in additive manufacturing at the micro and nano size scales and in the production of complex anti-counterfeiting structures. By using optical tweezers to trap particles, we are able isolate the varying forces acting upon colloidal particles. This allows us to probe the unique hydrodynamic repulsive force directly and demonstrates its critical influence over colloidal aggregation and assembly.

Finally, in chapter 5, I discuss solid state optical refrigeration for the first time at extreme (GPa) pressure conditions. Both single Yb:YLF microcrystals and polycrystalline Yb:YLF samples were placed inside a diamond anvil cell with LiF as a pressure medium. A martensitic second order phase transition of the Yb:YLF between scheelite and fergusonite phases was observed via photoluminescence spectra from Yb^{3+} ions. A decrease in the temperature of 20±5K below room temperature was observed for the scheelite phase for a single micro-crystal. Preliminary studies of temperature calibrated single Yb:YLF particles in water demonstrate cooling of approximately 16±5K below room temperature in the scheelite phase at elevated pressure. Raman measurements of the pressure transmitting medium, water, confirm its phase transformation to ice VII. This result illustrates the versatility of the particles cooling a variety of local environments and can potentially lead to achieving localized and fast (millisecond) cooling *in situ* in the DAC. Specifically, solid state laser cooling will enable researchers to explore new territories of both nucleation/crystallization and chemical fractionation kinetics at extreme conditions with various materials like high pressure ices that are important for understanding planetary interiors[332, 333].

We also discuss QD chalcogenide cavities in chapter 5. QDs can be successfully contained inside of a thin film cavity using PLD growth methods without destroying the quantum dots. Identifying exact locations of QDs for APT analysis is difficult,

but APT does reveal significant distributions of carbon and selenium that is likely due to resputtering of QDs, indication some damage may be done. However, minimal difference in the quantum dot photoluminescence is observed after the CdS deposition, demonstrating that the quantum dots survive the process. Shifts in the lifetime of the dots can be largely explained by evanescent wave contributions to radiative power and additional layer of CdS on the QDs, but some contribution of lifetime shortening is likely to the mild damage sustained by the dots. Further experiments will be performed with capping the films with distributed Bragg reflectors to isolate single photon sources from these cavities as well as modification of PLD parameters and additional pre- and post-deposition treatments of the films and QDs to prevent damage and resputtering of the dots.

BIBLIOGRAPHY

[1] P. Pringsheim, "Zwei bemerkungen uber den unterschied von lumineszenz- und temperaturstrahlung," *Zeitschrift fur Physik*, vol. 57, no. 11-12, pp. 739–746, 1929.

[2] R. I. Epstein, M. I. Buchwald, B. C. Edwards, T. R. Gosnell, and C. E. Mungan, "Observation of laser-induced fluorescent cooling of a solid," *Nature*, vol. 377, no. 6549, pp. 500–503, 1995. Rz336 Times Cited:579 Cited References Count:19.

[3] S. D. Melgaard, A. R. Albrecht, M. P. Hehlen, and M. Sheik-Bahae, "Solid-state optical refrigeration to sub-100 kelvin regime," *Sci Rep*, vol. 6, p. 20380, 2016. Melgaard, Seth D Albrecht, Alexander R Hehlen, Markus P Sheik-Bahae, Mansoor eng Research Support, U.S. Gov't, Non-P.H.S. England 2016/02/06 Sci Rep. 2016 Feb 5;6:20380. doi: 10.1038/srep20380.

[4] B. Topper, M. Peysokhan, A. R. Albrecht, A. S. Flores, S. Kuhn, D. Hässner, S. Hein, C. Hupel, J. Nold, N. Haarlammert, T. Schreiber, M. Sheik-Bahae, and A. Mafi, "Laser cooling of a yb doped silica fiber by 18 kelvin from room temperature," *Opt. Lett.*, vol. 46, pp. 5707–5710, Nov 2021.

[5] P. B. Roder, B. E. Smith, X. Zhou, M. J. Crane, and P. J. Pauzauskie, "Laser refrigeration of hydrothermal nanocrystals in physiological media," *Proceedings of the National Academy of Sciences*, vol. 112, no. 49, pp. 15024–15029, 2015.

[6] D. V. Seletskiy, M. P. Hehlen, R. I. Epstein, and M. Sheik-Bahae, "Cryogenic optical refrigeration," *Adv. Opt. Photon.*, vol. 4, pp. 78–107, Mar 2012.

[7] R. M. Pettit, W. Ge, P. Kumar, D. R. Luntz-Martin, J. T. Schultz, L. P. Neukirch, M. Bhattacharya, and A. N. Vamivakas, "An optical tweezer phonon laser," *Nature Photonics*, vol. 13, no. 6, pp. 402–405, 2019.

[8] G. Ranjit, D. P. Atherton, J. H. Stutz, M. Cunningham, and A. A. Geraci, "Attonewton force detection using microspheres in a dual-beam optical trap in high vacuum," *Phys. Rev. A*, vol. 91, p. 51805, 2015.

[9] L. W. Russell, E. C. Dossetor, A. A. Wood, D. A. Simpson, and P. J. Reece, "Optimizing optical tweezers experiments for magnetic resonance sensing with nanodiamonds," *ACS Photonics*, vol. 8, pp. 1214–1221, 4 2021.

[10] F. K. Fatemi and M. Bashkansky, "Spatially resolved magnetometry using cold atoms in dark optical tweezers," *Optics Express*, vol. 18, p. 2190, 2 2010.

[11] E. Eriksson, J. Enger, B. Nordlander, N. Erjavec, K. Ramser, M. Goksör, S. Hohmann, T. Nyström, and D. Hanstorp, "A microfluidic system in combination with optical tweezers for analyzing rapid and reversible cytological alterations in single cells upon environmental changes," *Lab Chip*, vol. 7, pp. 71–76, 2007.

[12] X. Wang, S. Chen, M. Kong, Z. Wang, K. D. Costa, R. A. Li, and D. Sun, "Enhanced cell sorting and manipulation with combined optical tweezer and microfluidic chip technologies," *Lab on a Chip*, vol. 11, p. 3656, 2011.

[13] J. Li, Z. Chen, Y. Liu, P. S. Kollipara, Y. Feng, Z. Zhang, and Y. Zheng, "Opto-refrigerative tweezers," *Science Advances*, vol. 7, 6 2021.

[14] J. Zhou, X. Dai, B. Jia, J. Qu, H.-P. Ho, B. Z. Gao, Y. Shao, and J. Chen, "Nanorefrigerative tweezers for optofluidic manipulation," *Applied Physics Letters*, vol. 120, p. 163701, 4 2022.

[15] L. Magrini, V. A. Camarena-Chávez, C. Bach, A. Johnson, and M. Aspelmeyer, "Squeezed light from a levitated nanoparticle at room temperature," *Physical Review Letters*, vol. 129, p. 053601, 7 2022.

[16] C. Weitenberg, S. Kuhr, K. Mølmer, and J. F. Sherson, "Quantum computation architecture using optical tweezers," *Physical Review A*, vol. 84, p. 032322, 9 2011.

[17] J. Beugnon, C. Tuchendler, H. Marion, A. Gaëtan, Y. Miroshnychenko, Y. R. P. Sortais, A. M. Lance, M. P. A. Jones, G. Messin, A. Browaeys, and P. Grangier, "Two-dimensional transport and transfer of a single atomic qubit in optical tweezers," *Nature Physics*, vol. 3, pp. 696–699, 10 2007.

[18] A. Ashkin, "Acceleration and trapping of particles by radiation pressure," *Physical Review Letters*, vol. 24, pp. 156–159, 1 1970.

[19] A. Ashkin, J. M. Dziedzic, J. Bjorkholm, and S. Chu, "Observation of a single-beam gradient force optical trap for dielectric particles," *Opt. Lett.*, vol. 11, no. 5, pp. 288–290, 1986.

[20] K. W. Krämer, D. Biner, G. Frei, H. U. Güdel, M. P. Hehlen, and S. R. Lüthi, "Hexagonal sodium yttrium fluoride based green and blue emitting upconversion phosphors," *Chemistry of Materials*, vol. 16, no. 7, pp. 1244–1251, 2004.

[21] J. P. van der Ziel, F. W. Ostermayer, and L. G. Van Uitert, "Infrared excitation of visible luminescence iny1-xerxf3via resonant energy transfer," *Physical Review B*, vol. 2, no. 11, pp. 4432–4441, 1970.

[22] H. Chou, P. Albers, A. Cassanho, and H. P. Jenssen, "Cw tunable laser emission of nd^{3+}:$na_{0.4}y_{0.6}f_{2.2}$," in *CW Tunable Laser Emission of Nd^{3+}:$Na_{0.4}Y_{0.6}F_{2.2}$*, p. FB6, OSA, 1986.

[23] X. J. Xia, A. Pant, E. J. Davis, and P. J. Pauzauskie, "Design of a radiation-balanced fiber laser via optically active composite cladding materials," *Journal of the Optical Society of America B-Optical Physics*, vol. 36, no. 12, pp. 3307–3314, 2019. Kb1da Times Cited:10 Cited References Count:38.

[24] T. Zhong, J. M. Kindem, J. G. Bartholomew, J. Rochman, I. Craiciu, E. Miyazono, M. Bettinelli, E. Cavalli, V. Verma, S. W. Nam, F. Marsili, M. D. Shaw, A. D. Beyer, and A. Faraon, "Nanophotonic rare-earth quantum memory with optically controlled retrieval," *Science*, vol. 357, pp. 1392–1395, 9 2017.

[25] A. Shalav, B. S. Richards, T. Trupke, K. W. Krämer, and H. U. Güdel, "Application of nayf4:er3+ up-converting phosphors for enhanced near-infrared silicon solar cell response," *Applied Physics Letters*, vol. 86, p. 013505, 1 2005.

[26] A. Pant, R. G. Felsted, A. B. Bard, X. Xia, S. Dadras, K. Shayan, D. R. Luntz-Martin, D. Mannikko, I. M. Pavlovetc, S. Stoll, M. Kuno, A. N. Vamivakas, and P. J. Pauzauskie, "Solid-state laser refrigeration of nanodiamond quantum sensors," *Nature Communications*, 2020.

[27] M. J. Dejneka, A. Streltsov, S. Pal, A. G. Frutos, C. L. Powell, K. Yost, P. K. Yuen, U. Müller, and J. Lahiri, "Rare earth-doped glass microbarcodes," *Proceedings of the National Academy of Sciences*, vol. 100, pp. 389–393, 1 2003.

[28] Y. Zhang, L. Zhang, R. Deng, J. Tian, Y. Zong, D. Jin, and X. Liu, "Multicolor barcoding in a single upconversion crystal," *Journal of the American Chemical Society*, vol. 136, pp. 4893–4896, 4 2014.

[29] H. Huang, J. Chen, Y. Liu, J. Lin, S. Wang, F. Huang, and D. Chen, "Lanthanide-doped core@multishell nanoarchitectures: Multimodal excitable upconverting/downshifting luminescence and high-level anti-counterfeiting," *Small*, vol. 16, no. 19, p. e2000708, 2020. Huang, Hai Chen, Jiangkun Liu, Yutong Lin, Jidong Wang, Shaoxiong Huang, Feng Chen, Daqin eng Research Support, Non-U.S. Gov't Germany 2020/04/21 Small. 2020 May;16(19):e2000708. doi: 10.1002/smll.202000708. Epub 2020 Apr 20.

[30] S. Wang, J. Feng, S. Song, and H. Zhang, "Rare earth fluorides upconversion nanophosphors: from synthesis to applications in bioimaging," *CrystEngComm*, vol. 15, p. 7142, 2013.

[31] Y. Ma, J. Bao, Y. Zhang, Z. Li, X. Zhou, C. Wan, L. Huang, Y. Zhao, G. Han, and T. Xue, "Mammalian near-infrared image vision through injectable and self-powered retinal nanoantennae," *Cell*, vol. 177, pp. 243–255.e15, 4 2019.

[32] X. Xia, A. Pant, A. S. Ganas, F. Jelezko, and P. J. Pauzauskie, "Quantum point defects for solid-state laser refrigeration," *Advanced Materials*, vol. 33, no. 23, p. 1905406, 2021.

[33] A. A. Rahman and P. Barker, "Laser refrigeration, alignment and rotation of levitated Yb^{3+}:YLF nanocrystals," *Nat. Photonics*, vol. 11, no. 10, p. 634, 2017.

[34] S. Rostami, A. R. Albrecht, A. Volpi, and M. Sheik-Bahae, "Observation of optical refrigeration in a holmium-doped crystal," *Photonics Research*, vol. 7, no. 4, pp. 445–451, 2019. Hr0qr Times Cited:16 Cited References Count:45.

[35] M. P. Hehlen, J. Meng, A. R. Albrecht, E. R. Lee, A. Gragossian, S. P. Love, C. E. Hamilton, R. I. Epstein, and M. Sheik-Bahae, "First demonstration of an all-solid-state optical cryocooler," *Light Sci Appl*, vol. 7, p. 15, 2018. Hehlen, Markus P Meng, Junwei Albrecht, Alexander R Lee, Eric R Gragossian, Aram Love, Steven P Hamilton, Christopher E Epstein, Richard I Sheik-Bahae, Mansoor eng England 2019/03/07 Light Sci Appl. 2018 Jun 6;7:15. doi: 10.1038/s41377-018-0028-7. eCollection 2018.

[36] S. D. Melgaard, A. R. Albrecht, M. P. Hehlen, and M. Sheik-Bahae, "Solid-state optical refrigeration to sub-100 kelvin regime," *Sci. Rep.*, vol. 6, p. 20380, 2016.

[37] M. P. Hehlen, "Crystal-field effects in fluoride crystals for optical refrigeration," *Laser Refrigeration of Solids Iii*, vol. 7614, p. 761404, 2010. Bsn20 Times Cited:14 Cited References Count:48 Proceedings of SPIE.

[38] D. Knowles, A. Cassanho, and H. Jenssen, "Optical properties of nd:nayf4 and ho:nayf4," *OSA Proc. Ser.*, p. CC7, 1989.

[39] A. Aebischer, M. Hostettler, J. Hauser, K. Kramer, T. Weber, H. U. Gudel, and H. B. Burgi, "Structural and spectroscopic characterization of active sites in a family of light-emitting sodium lanthanide tetrafluorides," *Angew Chem Int Ed Engl*, vol. 45, no. 17, pp. 2802–6, 2006. Aebischer, Annina Hostettler, Marc Hauser, Jurg Kramer, Karl Weber, Thomas Gudel, Hans Ulrich

Burgi, Hans-Beat eng Germany 2006/03/21 Angew Chem Int Ed Engl. 2006 Apr 21;45(17):2802-6. doi: 10.1002/anie.200503966.

[40] X. Li, D. Chen, F. Huang, G. Chang, J. Zhao, X. Qiao, X. Xu, J. Du, and M. Yin, "Phase-selective nanocrystallization of nalnf4 in aluminosilicate glass for random laser and 940 nm led-excitable upconverted luminescence," *Laser & Photonics Reviews*, vol. 12, no. 7, p. 1800030, 2018.

[41] X. Zhai, Y. Wang, X. Liu, S. Liu, P. Lei, S. Yao, S. Song, L. Zhou, J. Feng, and H. Zhang, "A simple strategy for the controlled synthesis of ultrasmall hexagonal-phase nayf4 :yb,er upconversion nanocrystals," *ChemPhotoChem*, vol. 1, no. 8, pp. 369–375, 2017.

[42] X. Ye, J. E. Collins, Y. Kang, J. Chen, D. T. Chen, A. G. Yodh, and C. B. Murray, "Morphologically controlled synthesis of colloidal upconversion nanophosphors and their shape-directed self-assembly," *Proc Natl Acad Sci U S A*, vol. 107, no. 52, pp. 22430–5, 2010. Ye, Xingchen Collins, Joshua E Kang, Yijin Chen, Jun Chen, Daniel T N Yodh, Arjun G Murray, Christopher B eng R41 EB008959/EB/NIBIB NIH HHS/ R41EB008959/EB/NIBIB NIH HHS/ Research Support, N.I.H., Extramural Research Support, Non-U.S. Gov't Research Support, U.S. Gov't, Non-P.H.S. 2010/12/15 Proc Natl Acad Sci U S A. 2010 Dec 28;107(52):22430-5. doi: 10.1073/pnas.1008958107. Epub 2010 Dec 10.

[43] C. Li, J. Yang, Z. Quan, P. Yang, D. Kong, and J. Lin, "Different microstructures of β-nayf4 fabricated by hydrothermal process: Effects of ph values and fluoride sources," *Chemistry of Materials*, vol. 19, no. 20, pp. 4933–4942, 2007.

[44] K. Zheng, W. Qin, G. Wang, G. Wei, D. Zhang, L. Wang, R. Kim, N. Liu, F. Ding, X. Xue, T. Jiang, and R. Yang, "Upconversion luminescence properties of yb3+, gd3+, and tm3+ co-doped nayf4 microcrystals synthesized by the hydrothermal method," *J Nanosci Nanotechnol*, vol. 10, no. 3, pp. 1920–3, 2010. Zheng, Kezhi Qin, Weiping Wang, Guofeng Wei, Guodong Zhang, Daisheng Wang, Lili Kim, Ryonginjin Liu, Ning Ding, Fuheng Xue, Xiaojie Jiang, Tao Yang, Renyuan eng 2010/04/02 J Nanosci Nanotechnol. 2010 Mar;10(3):1920-3. doi: 10.1166/jnn.2010.2077.

[45] J. Yang, L. Song, X. Wang, J. Dong, S. Gan, and L. Zou, "Facile synthesis and color-tunable properties of monodisperse beta-nayf4:ln(3+) (ln = eu, tb, tm, sm, ho) microtubes," *Dalton Trans*, vol. 47, no. 4, pp. 1294–1302, 2018. Yang, Junfeng Song, Lina Wang, Xiaoxue Dong, Jianchao Gan, Shucai Zou,

Lianchun eng England 2018/01/05 Dalton Trans. 2018 Jan 23;47(4):1294-1302. doi: 10.1039/c7dt04273f.

[46] M. Ding, C. Lu, L. Cao, Y. Ni, and Z. Xu, "Controllable synthesis, formation mechanism and upconversion luminescence of β-nayf4 : Yb3+/er3+ microcrystals by hydrothermal process," *CrystEngComm*, vol. 15, no. 41, pp. 8366–8373, 2013.

[47] A. B. Bard, X. Zhou, X. Xia, G. Zhu, M. B. Lim, S. M. Kim, M. C. Johnson, J. M. Kollman, M. A. Marcus, S. R. Spurgeon, D. E. Perea, A. Devaraj, J. Chun, J. J. D. Yoreo, and P. J. Pauzauskie, "A mechanistic understanding of nonclassical crystal growth in hydrothermally synthesized sodium yttrium fluoride nanowires," *Chemistry of Materials*, vol. 32, pp. 2753–2763, 4 2020.

[48] X. Zhou, B. E. Smith, P. B. Roder, and P. J. Pauzauskie, "Laser refrigeration of ytterbium-doped sodium–yttrium–fluoride nanowires," *Adv. Mater*, vol. 28, no. 39, pp. 8658–8662, 2016.

[49] G. Mie, "Beiträge zur optik trüber medien, speziell kolloidaler metallösungen," *Annalen der Physik*, vol. 330, pp. 377–445, 1908.

[50] H. Kudo, R. Suzuki, and T. Tanabe, "Whispering gallery modes in hexagonal microcavities," *Physical Review A*, vol. 88, no. 2, p. 023807, 2013. 196oe Times Cited:11 Cited References Count:32.

[51] A. Pant, B. E. Smith, M. J. Crane, X. Z. Zhou, M. B. Lim, S. A. Frazier, E. J. Davis, and P. J. Pauzauskie, "Optomechanical thermometry of nanoribbon cantilevers," *Journal of Physical Chemistry C*, vol. 122, no. 13, pp. 7525–7532, 2018. Gc2pr Times Cited:14 Cited References Count:40.

[52] P. P. Fedorov, V. B. Aleksandrov, O. S. Bondareva, I. I. Buchinskaya, M. D. Val'kovskii, and B. P. Sobolev, "Concentration dependences of the unit-cell parameters of nonstoichiometric fluorite-type na0.5 - x r 0.5 + x f2 + 2x phases (r = rare-earth elements)," *Crystallography Reports*, vol. 46, pp. 239–245, 3 2001.

[53] F. Zhang, Y. Wan, T. Yu, F. Zhang, Y. Shi, S. Xie, Y. Li, L. Xu, B. Tu, and D. Zhao, "Uniform nanostructured arrays of sodium rare-earth fluorides for highly efficient multicolor upconversion luminescence," *Angew Chem Int Ed Engl*, vol. 46, no. 42, pp. 7976–9, 2007. Zhang, Fan Wan, Ying Yu, Ting Zhang, Fuqiang Shi, Yifeng Xie, Songhai Li, Yigang Xu, Lei Tu, Bo Zhao, Dongyuan

eng Research Support, Non-U.S. Gov't Germany 2007/09/13 Angew Chem Int Ed Engl. 2007;46(42):7976-9. doi: 10.1002/anie.200702519.

[54] J. H. Burns, "Crystal structure of hexagonal sodium neodymium fluoride and related compounds," *Inorganic Chemistry*, vol. 4, no. 6, pp. 881–&, 1965. 65142 Times Cited:190 Cited References Count:24.

[55] P. P. Fedorov, "Systems of alkali and rare-earth metal fluorides," *Russian Journal of Inorganic Chemistry*, vol. 44, pp. 1703–1727, 1999.

[56] W. Patterson, D. Seletskiy, M. Sheik-Bahae, R. Epstein, and M. Hehlen, "Measurement of solid-state optical refrigeration by two-band differential luminescence thermometry," *J. Opt. Soc. Am. B*, vol. 27, no. 3, pp. 611–618, 2010.

[57] D. V. Seletskiy, S. D. Melgaard, R. I. Epstein, A. Di Lieto, M. Tonelli, and M. Sheik-Bahae, "Local laser cooling of Yb: YLF to 110 K," *Opt. Express*, vol. 19, no. 19, pp. 18229–18236, 2011.

[58] E. J. McLaurin, L. R. Bradshaw, and D. R. Gamelin, "Dual-emitting nanoscale temperature sensors," *Chemistry of Materials*, vol. 25, no. 8, pp. 1283–1292, 2013. 133nb Times Cited:326 Cited References Count:63.

[59] A. Pant, X. Xia, E. J. Davis, and P. J. Pauzauskie, "Solid-state laser refrigeration of a composite semiconductor Yb:YLiF4 optomechanical resonator," *Nature Communications*, vol. 11, no. 1, p. 3235, 2020.

[60] V. Pini, J. Tamayo, E. Gil-Santos, D. Ramos, P. Kosaka, H. D. Tong, C. van Rijn, and M. Calleja, "Shedding light on axial stress effect on resonance frequencies of nanocantilevers," *ACS Nano*, vol. 5, no. 6, pp. 4269–75, 2011. Pini, Valerio Tamayo, Javier Gil-Santos, Eduardo Ramos, Daniel Kosaka, Priscila Tong, Hien-Duy van Rijn, Cees Calleja, Montserrat eng Research Support, Non-U.S. Gov't 2011/05/11 ACS Nano. 2011 Jun 28;5(6):4269-75. doi: 10.1021/nn200623c. Epub 2011 May 16.

[61] J. W. Gibbs, "On the Equilibrium of Heterogeneous Substances," *American Journal of Science and Arts*, vol. 16, no. 96, p. 441, 1878.

[62] H. Cölfen and M. Antonietti, *Mesocrystals and Nonclassical Crystallization*. John Wiley & Sons, Ltd, 2008.

[63] J. J. D. Yoreo, P. U. P. A. Gilbert, N. A. J. M. Sommerdijk, R. L. Penn, S. Whitelam, D. Joester, H. Zhang, J. D. Rimer, A. Navrotsky, J. F. Banfield, A. F. Wallace, F. M. Michel, F. C. Meldrum, H. Cölfen, and P. M. Dove, "Crystallization by particle attachment in synthetic, biogenic, and geologic environments," *Science*, vol. 349, 7 2015.

[64] W. Ostwald, "Studien über die Bildung und Umwandlung fester Körper. 1. Abhandlung: Übersättigung und Überkaltung," *Zeitschrift für Physikalische Chemie*, vol. 22, pp. 289–330, 1897.

[65] S. Karthika, T. K. Radhakrishnan, and P. Kalaichelvi, "A Review of Classical and Nonclassical Nucleation Theories," *Crystal Growth and Design*, vol. 16, pp. 6663–6681, 11 2016.

[66] P. G. Vekilov, "The Two-Step Mechanism and the Solution-Crystal Spinodal for Nucleation of Crystals in Solution," in *Kinetics and Thermodynamics of Multistep Nucleation and Self-Assembly in Nanoscale Materials*, ch. 4, pp. 79–110, Hoboken, NJ: John Wiley & Sons, Ltd, 2012.

[67] J. W. Cahn, "On spinodal decomposition," *Acta Metallurgica*, vol. 9, pp. 795–801, 9 1961.

[68] N. D. Loh, S. Sen, M. Bosman, S. F. Tan, J. Zhong, C. A. Nijhuis, P. Král, P. Matsudaira, and U. Mirsaidov, "Multistep nucleation of nanocrystals in aqueous solution," *Nature Chemistry*, vol. 9, pp. 77–82, 1 2017.

[69] F. Wang, H.-C. Yu, M.-H. Chen, L. Wu, N. Pereira, K. Thornton, A. Van der Ven, Y. Zhu, G. G. Amatucci, and J. Graetz, "Tracking lithium transport and electrochemical reactions in nanoparticles," *Nature Communications*, vol. 3, p. 1201, 1 2012.

[70] A. F. Wallace, L. O. Hedges, A. Fernandez-Martinez, P. Raiteri, J. D. Gale, G. A. Waychunas, S. Whitelam, J. F. Banfield, and J. J. De Yoreo, "Microscopic Evidence for Liquid-Liquid Separation in Supersaturated CaCO3 Solutions," *Science*, vol. 341, pp. 885–889, 8 2013.

[71] Z. Zou, W. J. E. M. Habraken, L. Bertinetti, Y. Politi, A. Gal, S. Weiner, L. Addadi, and P. Fratzl, "On the Phase Diagram of Calcium Carbonate Solutions," *Advanced Materials Interfaces*, vol. 4, p. 1600076, 1 2017.

[72] J. Lee, K. Park, T. Chang, and J. C. Jung, "Polymer/probe interaction in probe diffusion through a polymer matrix: methyl red diffusion in poly(vinyl acetate)/toluene solutions," *Macromolecules*, vol. 25, pp. 6977–6979, 12 1992.

[73] H. Jiang, P. G. Debenedetti, and A. Z. Panagiotopoulos, "Nucleation in Aqueous NaCl Solutions Shifts from 1-step to 2-step Mechanism on Crossing the Spinodal," *The Journal of Chemical Physics*, vol. 150, p. 124502, 3 2019.

[74] X. Liu, S. W. Chee, S. Raj, M. Sawczyk, P. Král, and U. Mirsaidov, "Three-step nucleation of metal–organic framework nanocrystals," *Proceedings of the National Academy of Sciences*, vol. 118, 3 2021.

[75] M. Bohenek, A. Myerson, and W. Sun, "Thermodynamics, cluster formation and crystal growth in highly supersaturated solutions of KDP, ADP and TGS," *Journal of Crystal Growth*, vol. 179, pp. 213–225, 8 1997.

[76] W. J. E. M. Habraken, J. Tao, L. J. Brylka, H. Friedrich, L. Bertinetti, A. S. Schenk, A. Verch, V. Dmitrovic, P. H. H. Bomans, P. M. Frederik, J. Laven, P. van der Schoot, B. Aichmayer, G. de With, J. J. DeYoreo, and N. A. J. M. Sommerdijk, "Ion-association complexes unite classical and non-classical theories for the biomimetic nucleation of calcium phosphate," *Nature Communications*, vol. 4, p. 1507, 6 2013.

[77] P. Qiu, N. Zhou, Y. Wang, C. Zhang, Q. Wang, R. Sun, G. Gao, and D. Cui, "Tuning lanthanide ion-doped upconversion nanocrystals with different shapes via a one-pot cationic surfactant-assisted hydrothermal strategy," *CrystEngComm*, vol. 16, p. 1859, 3 2014.

[78] R. G. Felsted, A. Pant, A. B. Bard, X. Xia, D. R. Luntz-Martin, S. Dadras, S. Zhang, A. N. Vamivakas, and P. J. Pauzauskie, "Chemically tunable aspect ratio control and laser refrigeration of hexagonal sodium yttrium fluoride upconverting materials," *Crystal Growth & Design*, vol. 22, pp. 3605–3612, 6 2022.

[79] E. Matijevic, "Preparation and properties of uniform size colloids," *Chemistry of Materials*, vol. 5, pp. 412–426, 4 1993.

[80] J. Zhou, B. Del Rosal, D. Jaque, S. Uchiyama, and D. Jin, "Advances and challenges for fluorescence nanothermometry," *Nature methods*, vol. 17, no. 10, pp. 967–980, 2020.

[81] A. Fernandez-Bravo, D. Wang, E. S. Barnard, A. Teitelboim, C. Tajon, J. Guan, G. C. Schatz, B. E. Cohen, E. M. Chan, P. J. Schuck, and T. W. Odom, "Ultralow-threshold, continuous-wave upconverting lasing from subwavelength plasmons," *Nature Materials*, vol. 18, pp. 1172–1176, 11 2019.

[82] Y. Ma, J. Bao, Y. Zhang, Z. Li, X. Zhou, C. Wan, L. Huang, Y. Zhao, G. Han, and T. Xue, "Mammalian Near-Infrared Image Vision through Injectable and Self-Powered Retinal Nanoantennae," *Cell*, vol. 177, pp. 243–255.e15, 4 2019.

[83] X. Hua, A. S. Eggeman, E. Castillo-Martínez, R. Robert, H. S. Geddes, Z. Lu, C. J. Pickard, W. Meng, K. M. Wiaderek, N. Pereira, G. G. Amatucci, P. A. Midgley, K. W. Chapman, U. Steiner, A. L. Goodwin, and C. P. Grey, "Revisiting metal fluorides as lithium-ion battery cathodes," *Nature Materials*, 1 2021.

[84] J. Morral and J. Cahn, "Spinodal decomposition in ternary systems," *Acta Metallurgica*, vol. 19, pp. 1037–1045, 10 1971.

[85] R. Tavakoli, "Unconditionally energy stable time stepping scheme for Cahn-Morral equation: Application to multi-component spinodal decomposition and optimal space tiling," *Journal of Computational Physics*, vol. 304, pp. 441–464, 1 2016.

[86] R. E. Thoma, G. M. Hebert, H. Insley, and C. F. Weaver, "Phase equilibria in the system sodium fluoride-yttrium fluoride," *Inorganic Chemistry*, vol. 2, pp. 1005–1012, 10 1963.

[87] X. Xia, A. Pant, X. Zhou, E. A. Dobretsova, A. B. Bard, M. B. Lim, J. Y. D. Roh, D. R. Gamelin, and P. J. Pauzauskie, "Hydrothermal synthesis and solid-state laser refrigeration of ytterbium-doped potassium-lutetium-fluoride (klf) microcrystals," *Chemistry of Materials*, vol. 33, pp. 4417–4424, 6 2021.

[88] H.-X. Zhong, J.-M. Hong, X.-F. Cao, X.-T. Chen, and Z.-L. Xue, "Ionic-liquid-assisted synthesis of YF3 with different crystalline phases and morphologies," *Materials Research Bulletin*, vol. 44, pp. 623–628, 3 2009.

[89] A. Zalkin and D. H. Templeton, "The Crystal Structures of YF3 and Related Compounds," *Journal of the American Chemical Society*, vol. 75, pp. 2453–2458, 5 1953.

[90] M. Zhao, L. Li, and G. Li, "Advances of solution chemistry in stabilizing different crystal phases of inorganic nano-compounds," *CrystEngComm*, vol. 18, no. 48, pp. 9209–9222, 2016.

[91] C. Bessada, A. Rakhmatullin, A.-L. Rollet, and D. Zanghi, "High temperature NMR approach of mixtures of rare earth and alkali fluorides: An insight into the local structure," *Journal of Fluorine Chemistry*, vol. 130, pp. 45–52, 1 2009.

[92] A. A. Arnold, V. Terskikh, Q. Y. Li, R. Naccache, I. Marcotte, and J. A. Capobianco, "Structure of $NaYF_4$ Upconverting Nanoparticles: A Multinuclear Solid-State NMR and DFT Computational Study," *The Journal of Physical Chemistry C*, vol. 117, pp. 25733–25741, 12 2013.

[93] T. B. de Queiroz, M. Cabrera-Baez, P. Menegasso, E. D. Martinez, A. F. García Flores, C. Rettori, and R. R. Urbano, "Probing Surface Effects on α-$NaYF_4$ Nanoparticles by Nuclear Magnetic Resonance," *The Journal of Physical Chemistry C*, vol. 124, pp. 9523–9535, 4 2020.

[94] W. Nowacki, "Zur kristallstruktur von yf3," *Die Naturwissenschaften*, vol. 26, pp. 463–463, 7 1938.

[95] M. A. Ghebouli, B. Ghebouli, T. Chihi, M. Fatmi, R. Khenata, H. R. Jappor, and S. H. Naqib, "Electronic band structure, elastic, optical and thermodynamic characteristic of cubic yf3: An ab initio study," *Optik*, vol. 239, p. 166680, 8 2021.

[96] S. Sarkar and V. Mahalingam, "Tuning the crystalline phase and morphology of the yf3:eu^{3+} microcrystals through fluoride source," *CrystEngComm*, vol. 15, p. 5750, 2013.

[97] A. W. Xiao, G. Galatolo, and M. Pasta, "The case for fluoride-ion batteries," *Joule*, vol. 5, pp. 2823–2844, 11 2021.

[98] F. Chi, L. Yan, H. Lv, H. Yan, X. Yuan, and B. Jiang, "Sol–Gel Preparation of Ultralow Refractive Index Magnesium Fluoride Optical Films for Broadband Antireflective Coatings," *Nanoscience and Nanotechnology Letters*, vol. 4, pp. 441–444, 4 2012.

[99] D. R. Luntz-Martin, R. G. Felsted, S. Dadras, P. J. Pauzauskie, and A. N. Vamivakas, "Laser refrigeration of optically levitated sodium yttrium fluoride nanocrystals," *Optics Letters*, vol. 46, p. 3797, 8 2021.

[100] P. L. Stanwix, L. M. Pham, J. R. Maze, D. Le Sage, T. K. Yeung, P. Cappellaro, P. R. Hemmer, A. Yacoby, M. D. Lukin, and R. L. Walsworth, "Coherence of nitrogen-vacancy electronic spin ensembles in diamond," *Phys. Rev. B*, vol. 82, no. 20, p. 201201, 2010.

[101] L. Childress and R. Hanson, "Diamond NV centers for quantum computing and quantum networks," *MRS Bull.*, vol. 38, no. 2, pp. 134–138, 2013.

[102] I. Aharonovich, D. Englund, and M. Toth, "Solid-state single-photon emitters," *Nature Photonics*, vol. 10, no. 10, pp. 631–641, 2016.

[103] V. M. Acosta, E. Bauch, M. P. Ledbetter, A. Waxman, L.-S. Bouchard, and D. Budker, "Temperature dependence of the nitrogen-vacancy magnetic resonance in diamond," *Phys. Rev. Lett.*, vol. 104, no. 7, p. 070801, 2010.

[104] M. W. Doherty, V. V. Struzhkin, D. A. Simpson, L. P. McGuinness, Y. Meng, A. Stacey, T. J. Karle, R. J. Hemley, N. B. Manson, L. C. L. Hollenberg, and S. Prawer, "Electronic properties and metrology applications of the diamond nv$^-$ center under pressure," *Phys. Rev. Lett.*, vol. 112, p. 047601, Jan 2014.

[105] S. Hsieh, P. Bhattacharyya, C. Zu, T. Mittiga, T. J. Smart, F. Machado, B. Kobrin, T. O. Höhn, N. Z. Rui, M. Kamrani, S. Chatterjee, S. Choi, M. Zaletel, V. V. Struzhkin, J. E. Moore, V. I. Levitas, R. Jeanloz, and N. Y. Yao, "Imaging stress and magnetism at high pressures using a nanoscale quantum sensor," *Science*, vol. 366, no. 6471, pp. 1349–1354, 2019.

[106] K. Y. Yip, K. O. Ho, K. Y. Yu, Y. Chen, W. Zhang, S. Kasahara, Y. Mizukami, T. Shibauchi, Y. Matsuda, S. K. Goh, and S. Yang, "Measuring magnetic field texture in correlated electron systems under extreme conditions," *Science*, vol. 366, no. 6471, pp. 1355–1359, 2019.

[107] M. Lesik, T. Plisson, L. Toraille, J. Renaud, F. Occelli, M. Schmidt, O. Salord, A. Delobbe, T. Debuisschert, L. Rondin, P. Loubeyre, and J.-F. Roch, "Magnetic measurements on micrometer-sized samples under high pressure using designed nv centers," *Science*, vol. 366, no. 6471, pp. 1359–1362, 2019.

[108] S. Schmitt, T. Gefen, F. M. Stürner, T. Unden, G. Wolff, C. Müller, J. Scheuer, B. Naydenov, M. Markham, S. Pezzagna, *et al.*, "Submillihertz magnetic spectroscopy performed with a nanoscale quantum sensor," *Science*, vol. 356, no. 6340, pp. 832–837, 2017.

[109] C. J. Riedel, "Direct detection of classically undetectable dark matter through quantum decoherence," *Phys. Rev. D*, vol. 88, no. 11, p. 116005, 2013.

[110] A. Albrecht, A. Retzker, and M. B. Plenio, "Testing quantum gravity by nanodiamond interferometry with nitrogen-vacancy centers," *Phys. Rev. A*, vol. 90, no. 3, p. 033834, 2014.

[111] A. Arvanitaki and A. A. Geraci, "Detecting high-frequency gravitational waves with optically levitated sensors," *Phys. Rev. Lett.*, vol. 110, no. 7, p. 071105, 2013.

[112] A. Rahman, A. Frangeskou, M. Kim, S. Bose, G. Morley, and P. Barker, "Burning and graphitization of optically levitated nanodiamonds in vacuum," *Sci. Rep.*, vol. 6, p. 21633, 2016.

[113] J. Knall, P.-B. Vigneron, M. Engholm, P. D. Dragic, N. Yu, J. Ballato, M. Bernier, and M. J. F. Digonnet, "Laser cooling in a silica optical fiber at atmospheric pressure," *Opt. Lett.*, vol. 45, pp. 1092–1095, 2020.

[114] D. R. Luntz-Martin, R. G. Felsted, S. Dadras, P. J. Pauzauskie, and A. N. Vamivakas, "Laser refrigeration of optically levitated sodium yttrium fluoride nanocrystals," *Opt. Lett.*, vol. 46, pp. 3797–3800, 2021.

[115] F. Waldermann, P. Olivero, J. Nunn, K. Surmacz, Z. Wang, D. Jaksch, R. Taylor, I. Walmsley, M. Draganski, P. Reichart, *et al.*, "Creating diamond color centers for quantum optical applications," *Diamond Relat. Mater.*, vol. 16, no. 11, pp. 1887–1895, 2007.

[116] I. M. Pavlovetc, K. Aleshire, G. V. Hartland, and M. Kuno, "Approaches to mid-infrared, super-resolution imaging and spectroscopy," *Phys. Chem. Chem. Phys.*, vol. 22, pp. 4313–4325, 2020.

[117] Z. Li, K. Aleshire, M. Kuno, and G. V. Hartland, "Super-resolution far-field infrared imaging by photothermal heterodyne imaging," *J. Phys. Chem. B*, vol. 121, no. 37, pp. 8838–8846, 2017.

[118] V. Y. Osipov, F. Shakhov, N. Efimov, V. Minin, S. Kidalov, and A. Y. Vul, "Identification of paramagnetic nitrogen centers (P_1) in diamond crystallites synthesized via the sintering of detonation nanodiamonds at high pressure and temperature," *Phys. Solid State*, vol. 59, no. 6, pp. 1146–1153, 2017.

[119] A. Cox, M. Newton, and J. Baker, "13C, 14N and 15N ENDOR measurements on the single substitutional nitrogen centre (P_1) in diamond," *J. Phys. Condens. Matter*, vol. 6, no. 2, p. 551, 1994.

[120] I. M. Pavlovetc, E. A. Podshivaylov, R. Chatterjee, G. V. Hartland, P. A. Frantsuzov, and M. Kuno, "Infrared photothermal heterodyne imaging: Contrast mechanism and detection limits," *Journal of Applied Physics*, vol. 127, no. 16, p. 165101, 2020.

[121] E. Vasilyev, V. Ivanov-Omskii, and I. Bogush, "Interstitial carbon showing up in the absorption spectra of natural diamonds," *Tech. Phys.*, vol. 50, no. 6, pp. 711–714, 2005.

[122] D. V. Seletskiy, R. Epstein, and M. Sheik-Bahae, "Laser cooling in solids: advances and prospects," *Rep. Prog. Phys.*, vol. 79, no. 9, p. 096401, 2016.

[123] T. Plakhotnik, M. W. Doherty, J. H. Cole, R. Chapman, and N. B. Manson, "All-optical thermometry and thermal properties of the optically detected spin resonances of the NV^--center in nanodiamond," *Nano Lett.*, vol. 14, no. 9, pp. 4989–4996, 2014.

[124] M. Fukami, C. Yale, P. Andrich, X. Liu, F. Heremans, P. Nealey, and D. Awschalom, "All-optical cryogenic thermometry based on nitrogen-vacancy centers in nanodiamonds," *Phys. Rev. Appl.*, vol. 12, no. 1, p. 014042, 2019.

[125] C. Laube, J. Hellweg, C. Sturm, J. Griebel, M. Grundmann, A. Kahnt, and B. Abel, "Photoinduced heating of graphitized nanodiamonds monitored by the raman diamond peak," *The Journal of Physical Chemistry C*, vol. 122, no. 44, pp. 25685–25691, 2018.

[126] P. Neumann, I. Jakobi, F. Dolde, C. Burk, R. Reuter, G. Waldherr, J. Honert, T. Wolf, A. Brunner, J. H. Shim, D. Suter, H. Sumiya, J. Isoya, and J. Wrachtrup, "High-precision nanoscale temperature sensing using single defects in diamond," *Nano Letters*, vol. 13, pp. 2738–2742, jun 2013.

[127] G. Kucsko, P. C. Maurer, N. Y. Yao, M. Kubo, H. J. Noh, P. K. Lo, H. Park, and M. D. Lukin, "Nanometre-scale thermometry in a living cell," *Nature*, vol. 500, no. 7460, pp. 54–58, 2013.

[128] T. Delord, L. Nicolas, M. Bodini, and G. Hétet, "Diamonds levitating in a paul trap under vacuum: Measurements of laser-induced heating via nv center thermometry," *Applied Physics Letters*, vol. 111, no. 1, p. 013101, 2017.

[129] A. C. Frangeskou, A. T. M. A. Rahman, L. Gines, S. Mandal, O. A. Williams, P. F. Barker, and G. W. Morley, "Pure nanodiamonds for levitated optomechanics in vacuum," *New Journal of Physics*, vol. 20, p. 043016, apr 2018.

[130] D. V. Seletskiy, S. D. Melgaard, S. Bigotta, A. Di Lieto, M. Tonelli, and M. Sheik-Bahae, "Laser cooling of solids to cryogenic temperatures," *Nature Photonics*, vol. 4, no. 3, pp. 161–164, 2010.

[131] D. R. Luntz-Martin, R. G. Felsted, S. Dadras, P. J. Pauzauskie, and A. N. Vamivakas, "Laser refrigeration of optically levitated sodium yttrium fluoride nanocrystals," *Optics Letters*, vol. 46, no. 15, pp. 3797–3800, 2021.

[132] M. Kern, J. Jeske, D. W. M. Lau, A. D. Greentree, F. Jelezko, and J. Twamley, "Optical cryocooling of diamond," *Physical Review B*, vol. 95, no. 23, p. 235306, 2017.

[133] X. Xia, A. Pant, A. S. Ganas, F. Jelezko, and P. J. Pauzauskie, "Quantum point defects for solid-state laser refrigeration," *Advanced Materials*, vol. 33, p. 1905406, 6 2021.

[134] M. Sheik-Bahae and R. I. Epstein, "Can laser light cool semiconductors?," *Physical Review Letters*, vol. 92, p. 247403, Jun 2004.

[135] H. Gauck, M. Renn, E. Cornell, and K. Bertness, "Laser refrigeration in the solid state," in *Quantum Electronics and Laser Science Conference*, p. QPD16, Optical Society of America, 1995.

[136] Y. V. Morozov, S. Zhang, A. Pant, B. Jankó, S. D. Melgaard, D. A. Bender, P. J. Pauzauskie, and M. Kuno, "Can lasers really refrigerate cds nanobelts?," *Nature*, vol. 570, no. 7762, pp. E60–E61, 2019.

[137] C. K. Lin, H. C. Chang, M. Hayashi, and S. H. Lin, "Excitation properties of the H3 defect center in diamond: A theoretical study," *Chemical Physics Letters*, vol. 475, no. 1-3, pp. 68–72, 2009.

[138] R. Kolesov, S. Lasse, C. Rothfuchs, A. D. Wieck, K. Xia, T. Kornher, and J. Wrachtrup, "Superresolution microscopy of single rare-earth emitters in YAG and H3 centers in diamond," *Physical Review Letters*, vol. 120, no. 3, 2018.

[139] S. Rand and L. DeShazer, "Visible color-center laser in diamond," *Optics letters*, vol. 10, no. 10, pp. 481–483, 1985.

[140] T. T. Tran, B. Regan, E. A. Ekimov, Z. Mu, Y. Zhou, W.-b. Gao, P. Narang, A. S. Solntsev, M. Toth, I. Aharonovich, and C. Bradac, "Anti-stokes excitation of solid-state quantum emitters for nanoscale thermometry," *Science Advances*, vol. 5, no. 5, p. eaav9180, 2019.

[141] H. Pinto, R. Jones, D. Palmer, J. Goss, P. Briddon, and S. Öberg, "On the diffusion of NV defects in diamond," *Physica Status Solidi A*, vol. 209, no. 9, pp. 1765–1768, 2012.

[142] J. Mooney and P. Kambhampati, "Get the basics right: Jacobian conversion of wavelength and energy scales for quantitative analysis of emission spectra," *The Journal of Physical Chemistry Letters*, vol. 4, no. 19, pp. 3316–3318, 2013.

[143] M. Thomaz and G. Davies, "The decay time of N3 luminescence in natural diamond," *Proceedings of the Royal Society A*, vol. 362, no. 1710, pp. 405–419, 1978.

[144] G. Liaugaudas, A. T. Collins, K. Suhling, G. Davies, and R. Heintzmann, "Luminescence-lifetime mapping in diamond," *Journal of Physics: Condensed Matter.*, vol. 21, no. 36, p. 364210, 2009.

[145] H. Diab, C. Arnold, F. Lédée, G. Trippé-Allard, G. Delport, C. Vilar, F. Bretenaker, J. Barjon, J.-S. Lauret, E. Deleporte, *et al.*, "Impact of reabsorption on the emission spectra and recombination dynamics of hybrid perovskite single crystals," *Journal of Physical Chemical Letters*, vol. 8, no. 13, pp. 2977–2983, 2017.

[146] A. Collins, M. Thomaz, and M. I. B. Jorge, "Luminescence decay time of the 1.945 eV centre in type Ib diamond," *Journal of Physics C: Solid State Physics*, vol. 16, no. 11, p. 2177, 1983.

[147] A. Batalov, C. Zierl, T. Gaebel, P. Neumann, I.-Y. Chan, G. Balasubramanian, P. Hemmer, F. Jelezko, and J. Wrachtrup, "Temporal coherence of photons emitted by single nitrogen-vacancy defect centers in diamond using optical rabi-oscillations," *Physical Review Letters*, vol. 100, no. 7, p. 077401, 2008.

[148] N. Aslam, G. Waldherr, P. Neumann, F. Jelezko, and J. Wrachtrup, "Photo-induced ionization dynamics of the nitrogen vacancy defect in diamond investigated by single-shot charge state detection," *New Journal of Physics*, vol. 15, no. 1, p. 013064, 2013.

[149] S. D. Subedi, V. V. Fedorov, J. Peppers, D. V. Martyshkin, S. B. Mirov, L. Shao, and M. Loncar, "Laser spectroscopic characterization of negatively charged nitrogen-vacancy (NV^-) centers in diamond," *Optics Materials Express*, vol. 9, no. 5, pp. 2076–2087, 2019.

[150] T. Plakhotnik, M. W. Doherty, J. H. Cole, R. Chapman, and N. B. Manson, "All-optical thermometry and thermal properties of the optically detected spin resonances of the NV^--center in nanodiamond," *Nano Letters*, vol. 14, no. 9, pp. 4989–4996, 2014.

[151] D. M. Toyli, D. J. Christle, A. Alkauskas, B. B. Buckley, C. G. Van de Walle, and D. D. Awschalom, "Measurement and control of single nitrogen-vacancy center spins above 600 k," *Physical Review X*, vol. 2, p. 031001, Jul 2012.

[152] R. Jones, J. P. Goss, H. Pinto, and D. W. Palmer, "Diffusion of nitrogen in diamond and the formation of A-centres," *Diamond and Related Materials*, vol. 53, pp. 35–39, mar 2015.

[153] M. N. R. Ashfold, J. P. Goss, B. L. Green, P. W. May, M. E. Newton, and C. V. Peaker, "Nitrogen in diamond," *Chemical Reviews*, vol. 120, no. 12, pp. 5745–5794, 2020.

[154] S. Chakravarthi, C. Moore, A. Opsvig, C. Pederson, E. Hunt, A. Ivanov, I. Christen, S. Dunham, and K.-M. C. Fu, "Window into NV center kinetics via repeated annealing and spatial tracking of thousands of individual nv centers," *Physical Review Materials*, vol. 4, p. 023402, Feb 2020.

[155] P. Deák, B. Aradi, M. Kaviani, T. Frauenheim, and A. Gali, "Formation of nv centers in diamond: A theoretical study based on calculated transitions and migration of nitrogen and vacancy related defects," *Physical Review B*, vol. 89, p. 075203, Feb 2014.

[156] M. D. Crossfield, G. Davies, A. T. Collins, and E. C. Lightowlers, "The role of defect interactions in reducing the decay time of H3 luminescence in diamond," *Journal of Physics C: Solid State Physics*, vol. 7, pp. 1909–1917, may 1974.

[157] A. Ashkin and J. M. Dziedzic, "Optical levitation by radiation pressure," *Applied Physics Letters*, vol. 19, no. 8, pp. 283–285, 1971.

[158] M. Bhattacharya, A. N. Vamivakas, and P. Barker, "Levitated optomechanics: introduction," *Journal of the Optical Society of America B*, vol. 34, no. 6, pp. LO1–LO2, 2017.

[159] J. Gieseler, B. Deutsch, R. Quidant, and L. Novotny, "Subkelvin parametric feedback cooling of a laser-trapped nanoparticle," *Physical Review Letters*, vol. 109, no. 10, p. 103603, 2012. PRL.

[160] A. Setter, M. Toroš, J. F. Ralph, and H. Ulbricht, "Real-time kalman filter: Cooling of an optically levitated nanoparticle," *Physical Review A*, vol. 97, no. 3, p. 033822, 2018. PRA.

[161] F. Tebbenjohanns, M. Frimmer, A. Militaru, V. Jain, and L. Novotny, "Cold damping of an optically levitated nanoparticle to microkelvin temperatures," *Physical Review Letters*, vol. 122, no. 22, p. 223601, 2019. PRL.

[162] U. Delić, M. Reisenbauer, K. Dare, D. Grass, V. Vuletić, N. Kiesel, and M. Aspelmeyer, "Cooling of a levitated nanoparticle to the motional quantum ground state," *Science*, vol. 367, no. 6480, pp. 892–895, 2020.

[163] G. Ranjit, D. P. Atherton, J. H. Stutz, M. Cunningham, and A. A. Geraci, "Attonewton force detection using microspheres in a dual-beam optical trap in high vacuum," *Physical Review A*, vol. 91, no. 5, p. 051805, 2015. PRA.

[164] G. Ranjit, M. Cunningham, K. Casey, and A. A. Geraci, "Zeptonewton force sensing with nanospheres in an optical lattice," *Physical Review A*, vol. 93, no. 5, p. 053801, 2016. PRA.

[165] D. Hempston, J. Vovrosh, M. Toroš, G. Winstone, M. Rashid, and H. Ulbricht, "Force sensing with an optically levitated charged nanoparticle," *Applied Physics Letters*, vol. 111, no. 13, p. 133111, 2017.

[166] A. A. Geraci, S. B. Papp, and J. Kitching, "Short-range force detection using optically cooled levitated microspheres," *Physical Review Letters*, vol. 105, no. 10, p. 101101, 2010. PRL.

[167] B. Rodenburg, L. P. Neukirch, A. N. Vamivakas, and M. Bhattacharya, "Quantum model of cooling and force sensing with an optically trapped nanoparticle," *Optica*, vol. 3, no. 3, p. 318, 2016.

[168] T. A. Nieminen, N. R. Heckenberg, and H. Rubinsztein-dunlop, "Optical measurement of microscopic torques," *Journal of Modern Optics*, vol. 48, no. 3, pp. 405–413, 2001. doi: 10.1080/09500340108230922.

[169] A. La Porta and M. D. Wang, "Optical torque wrench: Angular trapping, rotation, and torque detection of quartz microparticles," *Physical Review Letters*, vol. 92, no. 19, p. 190801, 2004. PRL.

[170] Z. Xu and T. Li, "Detecting casimir torque with an optically levitated nanorod," *Physical Review A*, vol. 96, no. 3, p. 033843, 2017. PRA.

[171] S. Kuhn, A. Kosloff, B. A. Stickler, F. Patolsky, K. Hornberger, M. Arndt, and J. Millen, "Full rotational control of levitated silicon nanorods," *Optica*, vol. 4, no. 3, pp. 356–360, 2017.

[172] J. Ahn, Z. Xu, J. Bang, P. Ju, X. Gao, and T. Li, "Ultrasensitive torque detection with an optically levitated nanorotor," *Nature Nanotechnology*, vol. 15, no. 2, pp. 89–93, 2020.

[173] A. A. Geraci, S. J. Smullin, D. M. Weld, J. Chiaverini, and A. Kapitulnik, "Improved constraints on non-newtonian forces at 10 microns," *Physical Review D*, vol. 78, no. 2, p. 022002, 2008. PRD.

[174] C. Kurtsiefer, S. Mayer, P. Zarda, and H. Weinfurter, "Stable solid-state source of single photons," *Physical Review Letters*, vol. 85, no. 2, pp. 290–293, 2000. PRL.

[175] A. Beveratos, S. Kühn, R. Brouri, T. Gacoin, J. P. Poizat, and P. Grangier, "Room temperature stable single-photon source," *The European Physical Journal D - Atomic, Molecular, Optical and Plasma Physics*, vol. 18, no. 2, pp. 191–196, 2002.

[176] P. L. Stanwix, L. M. Pham, J. R. Maze, D. Le Sage, T. K. Yeung, P. Cappellaro, P. R. Hemmer, A. Yacoby, M. D. Lukin, and R. L. Walsworth, "Coherence of nitrogen-vacancy electronic spin ensembles in diamond," *Physical Review B*, vol. 82, no. 20, p. 201201, 2010. PRB.

[177] R. M. Pettit, L. P. Neukirch, Y. Zhang, and A. Nick Vamivakas, "Coherent control of a single nitrogen-vacancy center spin in optically levitated nanodiamond," *Journal of the Optical Society of America B*, vol. 34, no. 6, pp. C31–C35, 2017.

[178] V. M. Acosta, E. Bauch, M. P. Ledbetter, A. Waxman, L. S. Bouchard, and D. Budker, "Temperature dependence of the nitrogen-vacancy magnetic resonance in diamond," *Physical Review Letters*, vol. 104, no. 7, p. 070801, 2010. PRL.

[179] E. Togan, Y. Chu, A. S. Trifonov, L. Jiang, J. Maze, L. Childress, M. V. G. Dutt, A. S. Sørensen, P. R. Hemmer, A. S. Zibrov, and M. D. Lukin, "Quantum entanglement between an optical photon and a solid-state spin qubit," *Nature*, vol. 466, no. 7307, pp. 730–734, 2010.

[180] L. Childress and R. Hanson, "Diamond nv centers for quantum computing and quantum networks," *MRS Bulletin*, vol. 38, no. 2, pp. 134–138, 2013.

[181] K. Nemoto, M. Trupke, S. J. Devitt, B. Scharfenberger, K. Buczak, J. Schmiedmayer, and W. J. Munro, "Photonic quantum networks formed from nv- centers," *Scientific Reports*, vol. 6, no. 1, p. 26284, 2016.

[182] L. P. Neukirch, J. Gieseler, R. Quidant, L. Novotny, and A. Nick Vamivakas, "Observation of nitrogen vacancy photoluminescence from an optically levitated nanodiamond," *Optics Letters*, vol. 38, no. 16, pp. 2976–2979, 2013.

[183] Z.-q. Yin, T. Li, X. Zhang, and L. M. Duan, "Large quantum superpositions of a levitated nanodiamond through spin-optomechanical coupling," *Physical Review A*, vol. 88, no. 3, p. 033614, 2013. PRA.

[184] L. P. Neukirch, E. von Haartman, J. M. Rosenholm, and A. Nick Vamivakas, "Multi-dimensional single-spin nano-optomechanics with a levitated nanodiamond," *Nature Photonics*, vol. 9, no. 10, pp. 653–657, 2015.

[185] T. M. Hoang, J. Ahn, J. Bang, and T. Li, "Electron spin control of optically levitated nanodiamonds in vacuum," *Nature Communications*, vol. 7, no. 1, p. 12250, 2016.

[186] D. M. Toyli, D. J. Christle, A. Alkauskas, B. B. Buckley, C. G. Van de Walle, and D. D. Awschalom, "Measurement and control of single nitrogen-vacancy center spins above 600 k," *Physical Review X*, vol. 2, no. 3, p. 031001, 2012. PRX.

[187] A. T. M. A. Rahman, A. C. Frangeskou, M. S. Kim, S. Bose, G. W. Morley, and P. F. Barker, "Burning and graphitization of optically levitated nanodiamonds in vacuum," *Scientific Reports*, vol. 6, no. 1, p. 21633, 2016.

[188] L.-M. Zhou, K.-W. Xiao, J. Chen, and N. Zhao, "Optical levitation of nanodiamonds by doughnut beams in vacuum," *Laser & Photonics Reviews*, vol. 11, no. 2, p. 1600284, 2017.

[189] A. C. Frangeskou, A. T. M. A. Rahman, L. Gines, S. Mandal, O. A. Williams, P. F. Barker, and G. W. Morley, "Pure nanodiamonds for levitated optomechanics in vacuum," *New Journal of Physics*, vol. 20, no. 4, p. 043016, 2018.

[190] D. V. Seletskiy, R. Epstein, and M. Sheik-Bahae, "Laser cooling in solids: advances and prospects," *Reports on Progress in Physics*, vol. 79, no. 9, p. 096401, 2016.

[191] X. Xia, A. Pant, A. S. Ganas, F. Jelezko, and P. J. Pauzauskie, "Quantum point defects for solid-state laser refrigeration," *Adv Mater*, vol. 33, no. 23, p. e1905406, 2021. Xia, Xiaojing Pant, Anupum Ganas, Abbie S Jelezko, Fedor Pauzauskie, Peter J eng FA9550-16-1-0362/AFOSR 1555007/National Science Foundation Review Germany 2020/07/16 Adv Mater. 2021 Jun;33(23):e1905406. doi: 10.1002/adma.201905406. Epub 2020 Jul 14.

[192] A. T. M. A. Rahman and P. F. Barker, "Laser refrigeration, alignment and rotation of levitated yb3+:ylf nanocrystals," *Nature Photonics*, vol. 11, no. 10, pp. 634–638, 2017.

[193] M. Kern, J. Jeske, D. W. M. Lau, A. D. Greentree, F. Jelezko, and J. Twamley, "Optical cryocooling of diamond," *Phys. Rev. B*, vol. 95, no. 23, p. 235306, 2017. PRB.

[194] U. Delić, M. Reisenbauer, K. Dare, D. Grass, V. Vuletić, N. Kiesel, and M. Aspelmeyer, "Cooling of a levitated nanoparticle to the motional quantum ground state," *Science*, vol. 367, no. 6480, pp. 892–895, 2020.

[195] F. Tebbenjohanns, M. L. Mattana, M. Rossi, M. Frimmer, and L. Novotny, "Quantum control of a nanoparticle optically levitated in cryogenic free space," *Nature*, vol. 595, no. 7867, pp. 378–382, 2021.

[196] C. P. Blakemore, A. D. Rider, S. Roy, Q. Wang, A. Kawasaki, and G. Gratta, "Three-dimensional force-field microscopy with optically levitated microspheres," *Physical Review A*, vol. 99, no. 2, p. 023816, 2019. PRA.

[197] C. Montoya, E. Alejandro, W. Eom, D. Grass, N. Clarisse, A. Witherspoon, and A. A. Geraci, "Scanning force sensing at micrometer distances from a conductive surface with nanospheres in an optical lattice," *Applied Optics*, vol. 61, no. 12, pp. 3486–3493, 2022.

[198] G. Winstone, R. Bennett, M. Rademacher, M. Rashid, S. Buhmann, and H. Ulbricht, "Direct measurement of the electrostatic image force of a levitated charged nanoparticle close to a surface," *Physical Review A*, vol. 98, no. 5, p. 053831, 2018. PRA.

[199] R. Reimann, M. Doderer, E. Hebestreit, R. Diehl, M. Frimmer, D. Windey, F. Tebbenjohanns, and L. Novotny, "Ghz rotation of an optically trapped nanoparticle in vacuum," *Physical Review Letters*, vol. 121, no. 3, p. 033602, 2018. PRL.

[200] F. Ricci, M. T. Cuairan, A. W. Schell, E. Hebestreit, R. A. Rica, N. Meyer, and R. Quidant, "A chemical nanoreactor based on a levitated nanoparticle in vacuum," *ACS Nano*, vol. 16, no. 6, pp. 8677–8683, 2022. doi: 10.1021/acsnano.2c01693.

[201] G. Ranjit, M. Cunningham, K. Casey, and A. A. Geraci, "Zeptonewton force sensing with nanospheres in an optical lattice," *Physical Review A*, vol. 93, no. 5, p. 053801, 2016. PRA.

[202] F. Monteiro, S. Ghosh, A. G. Fine, and D. C. Moore, "Optical levitation of 10-ng spheres with nano-g acceleration sensitivity," *Physical Review A*, vol. 96, no. 6, p. 063841, 2017. PRA.

[203] F. Monteiro, G. Afek, D. Carney, G. Krnjaic, J. Wang, and D. C. Moore, "Search for composite dark matter with optically levitated sensors," *Physical Review Letters*, vol. 125, no. 18, p. 181102, 2020. PRL.

[204] N. Aggarwal, G. P. Winstone, M. Teo, M. Baryakhtar, S. L. Larson, V. Kalogera, and A. A. Geraci, "Searching for new physics with a levitated-sensor-based gravitational-wave detector," *Physical Review Letters*, vol. 128, no. 11, p. 111101, 2022. PRL.

[205] L. S. Collaboration, C. Virgo, B. P. Abbott, R. Abbott, T. D. Abbott, M. R. Abernathy, F. Acernese, K. Ackley, C. Adams, T. Adams, P. Addesso, R. X. Adhikari, V. B. Adya, C. Affeldt, M. Agathos, K. Agatsuma, N. Aggarwal, O. D. Aguiar, L. Aiello, A. Ain, P. Ajith, B. Allen, A. Allocca, P. A. Altin, S. B. Anderson, W. G. Anderson, K. Arai, M. A. Arain, M. C. Araya, C. C. Arceneaux, J. S. Areeda, N. Arnaud, K. G. Arun, S. Ascenzi, G. Ashton, M. Ast, S. M. Aston, P. Astone, P. Aufmuth, C. Aulbert, S. Babak, P. Bacon, M. K. M. Bader, P. T. Baker, F. Baldaccini, G. Ballardin, S. W. Ballmer, J. C. Barayoga, S. E. Barclay, B. C. Barish, D. Barker, F. Barone, B. Barr, L. Barsotti, M. Barsuglia, D. Barta, J. Bartlett, M. A. Barton, I. Bartos, R. Bassiri, A. Basti, J. C. Batch, C. Baune, V. Bavigadda, M. Bazzan, B. Behnke, M. Bejger, C. Belczynski, A. S. Bell, C. J. Bell, B. K. Berger, J. Bergman, G. Bergmann, C. P. L. Berry, D. Bersanetti, A. Bertolini, J. Betzwieser, S. Bhagwat, R. Bhandare, I. A. Bilenko, G. Billingsley, J. Birch, R. Birney, O. Birnholtz, S. Biscans, A. Bisht, M. Bitossi, C. Biwer, M. A. Bizouard, J. K. Blackburn, C. D. Blair, D. G. Blair, R. M. Blair, S. Bloemen, O. Bock, T. P. Bodiya, M. Boer, G. Bogaert, C. Bogan, A. Bohe, *et al.*, "Observation of gravitational waves from a binary black hole merger," *Physical Review Letters*, vol. 116, no. 6, p. 061102, 2016. PRL.

[206] T. e. Consortium, P. Seoane, S. Aoudia, H. Audley, G. Auger, S. Babak, J. Baker, E. Barausse, S. Barke, M. Bassan, V. Beckmann, M. Benacquista, P. L. Bender, E. Berti, P. Binétruy, J. Bogenstahl, C. Bonvin, D. Bortoluzzi, N. C. Brause, J. Brossard, S. Buchman, I. Bykov, J. Camp, C. Caprini, A. Cavalleri, M. Cerdonio, G. Ciani, M. Colpi, G. Congedo, J. Conklin, N. Cornish, K. Danzmann, G. de Vine, D. DeBra, M. D. Freitag, L. Di Fiore, M. D. Aguilo, I. Diepholz, R. Dolesi, M. Dotti, G. F. Barranco, L. Ferraioli, V. Ferroni, N. Finetti, E. Fitzsimons, J. Gair, F. Galeazzi, A. Garcia, O. Gerberding, L. Gesa, D. Giardini, F. Gibert, C. Grimani, P. Groot, F. G. Cervantes, Z. Haiman, H. Halloin, G. Heinzel, M. Hewitson, C. Hogan, D. Holz, A. Hornstrup, D. Hoyland, C. D. Hoyle, M. Hueller, S. Hughes, P. Jetzer, V. Kalogera, N. Karnesis, M. Kilic, C. Killow, W. Klipstein, E. Kochkina, N. Korsakova, A. Krolak, S. Larson, M. Lieser, T. Littenberg, J. Livas, I. Lloro, D. Mance,

P. Madau, P. Maghami, C. Mahrdt, T. Marsh, I. Mateos, L. Mayer, D. McClelland, K. McKenzie, S. McWilliams, S. Merkowitz, C. Miller, S. Mitryk, J. Moerschell, S. Mohanty, A. Monsky, G. Mueller, V. Müller, G. Nelemans, D. Nicolodi, *et al.*, "The gravitational universe," *arXiv*, 2013.

[207] P. Amaro-Seoane, H. Audley, S. Babak, J. Baker, E. Barausse, P. Bender, E. Berti, P. Binetruy, M. Born, D. Bortoluzzi, J. Camp, C. Caprini, V. Cardoso, M. Colpi, J. Conklin, N. Cornish, C. Cutler, K. Danzmann, R. Dolesi, L. Ferraioli, V. Ferroni, E. Fitzsimons, J. Gair, L. G. Bote, D. Giardini, F. Gibert, C. Grimani, H. Halloin, G. Heinzel, T. Hertog, M. Hewitson, K. Holley-Bockelmann, D. Hollington, M. Hueller, H. Inchauspe, P. Jetzer, N. Karnesis, C. Killow, A. Klein, B. Klipstein, N. Korsakova, S. L. Larson, J. Livas, I. Lloro, N. Man, D. Mance, J. Martino, I. Mateos, K. McKenzie, S. T. McWilliams, C. Miller, G. Mueller, G. Nardini, G. Nelemans, M. Nofrarias, A. Petiteau, P. Pivato, E. Plagnol, E. Porter, J. Reiche, D. Robertson, N. Robertson, E. Rossi, G. Russano, B. Schutz, A. Sesana, D. Shoemaker, J. Slutsky, C. F. Sopuerta, T. Sumner, N. Tamanini, I. Thorpe, M. Troebs, M. Vallisneri, A. Vecchio, D. Vetrugno, S. Vitale, M. Volonteri, G. Wanner, H. Ward, P. Wass, W. Weber, J. Ziemer, and P. Zweifel, "Laser interferometer space antenna," *arXiv*, 2017.

[208] S. Kolkowitz, I. Pikovski, N. Langellier, M. D. Lukin, R. L. Walsworth, and J. Ye, "Gravitational wave detection with optical lattice atomic clocks," *Physical Review D*, vol. 94, no. 12, p. 124043, 2016. PRD.

[209] J. Coleman, "Magis-100 at fermilab," in *Proc. Sci.*, Sissa Medialab, 2018.

[210] C. Holometer, A. S. Chou, R. Gustafson, C. Hogan, B. Kamai, O. Kwon, R. Lanza, S. L. Larson, L. McCuller, S. S. Meyer, J. Richardson, C. Stoughton, R. Tomlin, and R. Weiss, "Mhz gravitational wave constraints with decameter michelson interferometers," *Physical Review D*, vol. 95, no. 6, p. 063002, 2017. PRD.

[211] T. Akutsu, S. Kawamura, A. Nishizawa, K. Arai, K. Yamamoto, D. Tatsumi, S. Nagano, E. Nishida, T. Chiba, R. Takahashi, N. Sugiyama, M. Fukushima, T. Yamazaki, and M.-K. Fujimoto, "Search for a stochastic background of 100-mhz gravitational waves with laser interferometers," *Physical Review Letters*, vol. 101, no. 10, p. 101101, 2008. PRL.

[212] V. Domcke and C. Garcia-Cely, "Potential of radio telescopes as high-frequency gravitational wave detectors," *Physical Review Letters*, vol. 126, no. 2, p. 021104, 2021. PRL.

[213] S. Singh, L. A. D. Lorenzo, I. Pikovski, and K. C. Schwab, "Detecting continuous gravitational waves with superfluid 4he," *New Journal of Physics*, vol. 19, no. 7, 2017.

[214] A. M. Cruise, "The potential for very high-frequency gravitational wave detection," *Classical and Quantum Gravity*, vol. 29, no. 9, 2012.

[215] S. M. Vermeulen, L. Aiello, A. Ejlli, W. L. Griffiths, A. L. James, K. L. Dooley, and H. Grote, "An experiment for observing quantum gravity phenomena using twin table-top 3d interferometers," *Classical and Quantum Gravity*, vol. 38, no. 8, p. 085008, 2021.

[216] A. Nishizawa, S. Kawamura, T. Akutsu, K. Arai, K. Yamamoto, D. Tatsumi, E. Nishida, M.-a. Sakagami, T. Chiba, R. Takahashi, and N. Sugiyama, "Laser-interferometric detectors for gravitational wave backgrounds at 100 mhz: Detector design and sensitivity," *Physical Review D*, vol. 77, no. 2, p. 022002, 2008. PRD.

[217] A. Ito, T. Ikeda, K. Miuchi, and J. Soda, "Probing ghz gravitational waves with graviton–magnon resonance," *The European Physical Journal C*, vol. 80, no. 3, p. 179, 2020.

[218] A. Ejlli, D. Ejlli, A. M. Cruise, G. Pisano, and H. Grote, "Upper limits on the amplitude of ultra-high-frequency gravitational waves from graviton to photon conversion," *The European Physical Journal C*, vol. 79, no. 12, p. 1032, 2019.

[219] A. Arvanitaki and A. A. Geraci, "Detecting high-frequency gravitational waves with optically levitated sensors," *Physical Review Letters*, vol. 110, no. 7, p. 071105, 2013. PRL.

[220] B. Pierre, B. Alejandro, C. Chiara, and D. Jean-François, "Cosmological backgrounds of gravitational waves and elisa/ngo: phase transitions, cosmic strings and other sources," *Journal of Cosmology and Astroparticle Physics*, vol. 2012, no. 06, p. 027, 2012.

[221] A. D. Rider, D. C. Moore, C. P. Blakemore, M. Louis, M. Lu, and G. Gratta, "Search for screened interactions associated with dark energy below the $100\mu m$ length scale," *Physical Review Letters*, vol. 117, no. 10, p. 101101, 2016. PRL.

[222] A. T. M. A. Rahman and P. F. Barker, "Laser refrigeration, alignment and rotation of levitated yb3+:ylf nanocrystals," *Nature Photonics*, vol. 11, no. 10, pp. 634–+, 2017. Fi6ly Times Cited:70 Cited References Count:31.

[223] M. Beck, "Overcoming "stiction" forces: Launching silica microspheres into an optical trap," *arXiv*, 2012.

[224] P. R. Wiecha, "pygdm—a python toolkit for full-field electro-dynamical simulations and evolutionary optimization of nanostructures," *Computer Physics Communications*, vol. 233, pp. 167–192, 2018.

[225] M. Rashid, M. Toroš, A. Setter, and H. Ulbricht, "Precession motion in levitated optomechanics," *Physical Review Letters*, vol. 121, no. 25, p. 253601, 2018. PRL.

[226] T. Seberson and F. Robicheaux, "Stability and dynamics of optically levitated dielectric disks in a gaussian standing wave beyond the harmonic approximation," *Physical Review Research*, vol. 2, no. 3, p. 033437, 2020. PRRESEARCH.

[227] L. Novotny and B. Hecht, *Principles of Nano-Optics*. Cambridge: Cambridge University Press, 2006.

[228] D. E. Chang, K. K. Ni, O. Painter, and H. J. Kimble, "Ultrahigh-q mechanical oscillators through optical trapping," *New Journal of Physics*, vol. 14, no. 4, 2012.

[229] R. Boidin, T. Halenkovič, V. Nazabal, L. Beneš, and P. Němec, "Pulsed laser deposited alumina thin films," *Ceramics International*, vol. 42, no. 1, Part B, pp. 1177–1182, 2016.

[230] Z. Li, Q. Fan, and Y. Yin, "Colloidal self-assembly approaches to smart nanostructured materials," *Chemical Reviews*, vol. 122, no. 5, pp. 4976–5067, 2022. doi: 10.1021/acs.chemrev.1c00482.

[231] J. Zhang, Y. Li, X. Zhang, and B. Yang, "Colloidal self-assembly meets nanofabrication: From two-dimensional colloidal crystals to nanostructure arrays," *Advanced Materials*, vol. 22, no. 38, pp. 4249–4269, 2010.

[232] G. Mirabello, A. Ianiro, P. H. H. Bomans, T. Yoda, A. Arakaki, H. Friedrich, G. De With, and N. A. J. M. Sommerdijk, "Crystallization by particle attachment is a colloidal assembly process," *Nature Materials*, vol. 19, no. 4, pp. 391–396, 2020.

[233] L. Liu, E. Nakouzi, M. L. Sushko, G. K. Schenter, C. J. Mundy, J. Chun, and J. J. D. Yoreo, "Connecting energetics to dynamics in particle growth by oriented attachment using real-time observations," *Nature Communications*, vol. 11, p. 1045, 12 2020.

[234] D. Hahm, J. Lim, H. Kim, J.-W. Shin, S. Hwang, S. Rhee, J. H. Chang, J. Yang, C. H. Lim, H. Jo, B. Choi, N. S. Cho, Y.-S. Park, D. C. Lee, E. Hwang, S. Chung, C.-M. Kang, M. S. Kang, and W. K. Bae, "Direct patterning of colloidal quantum dots with adaptable dual-ligand surface," *Nature Nanotechnology*, vol. 17, no. 9, pp. 952–958, 2022.

[235] A. T. L. Tan, J. Beroz, M. Kolle, and A. J. Hart, "Direct-write freeform colloidal assembly," *Advanced Materials*, vol. 30, no. 44, p. 1803620, 2018.

[236] B. Derjaguin and L. Landau, "Theory of the stability of strongly charged lyophobic sols and of the adhesion of strongly charged particles in solutions of electrolytes," *Progress in Surface Science*, vol. 43, no. 1, pp. 30–59, 1993.

[237] E. J. W. Verwey, "Theory of the stability of lyophobic colloids," *The Journal of Physical and Colloid Chemistry*, vol. 51, no. 3, pp. 631–636, 1947. doi: 10.1021/j150453a001.

[238] F. Zhang, Y. Wan, T. Yu, F. Zhang, Y. Shi, S. Xie, Y. Li, L. Xu, B. Tu, and D. Zhao, "Uniform nanostructured arrays of sodium rare-earth fluorides for highly efficient multicolor upconversion luminescence," *Angewandte Chemie International Edition*, vol. 46, pp. 7976–7979, 10 2007.

[239] A. Fedotov, D. Pominova, E. O. Orlovskaya, Y. V. Orlovskii, T. Niemi, and R. Gumenyuk, "Analysis of upconversion nanoparticles as an active medium for upconversion light sources," in *Analysis of upconversion nanoparticles as an active medium for upconversion light sources* (M. J. Digonnet and S. Jiang, eds.), p. 26, SPIE, 3 2019.

[240] G. Winstone, Z. Wang, S. Klomp, G. R. Felsted, A. Laeuger, C. Gupta, D. Grass, N. Aggarwal, J. Sprague, P. J. Pauzauskie, S. L. Larson, V. Kalogera, and A. A. Geraci, "Optical trapping of high-aspect-ratio nayf hexagonal prisms for khz-mhz gravitational wave detectors," *Physical Review Letters*, vol. 129, p. 053604, 7 2022.

[241] X. Shan, F. Wang, D. Wang, S. Wen, C. Chen, X. Di, P. Nie, J. Liao, Y. Liu, L. Ding, P. J. Reece, and D. Jin, "Optical tweezers beyond refractive index mismatch using highly doped upconversion nanoparticles," *Nature Nanotechnology*, vol. 16, pp. 531–537, 5 2021.

[242] M. P. Hehlen, "Crystal-field effects in fluoride crystals for optical refrigeration," *Laser Refrigeration of Solids Iii*, vol. 7614, p. 761404, 2010. Bsn20 Times Cited:14 Cited References Count:48 Proceedings of SPIE.

[243] D. M. Roy and R. Roy, "Controlled massively defective crystalline solutions with the fluorite structure," *Journal of The Electrochemical Society*, vol. 111, p. 421, 4 1964.

[244] C. M. Jin, W. Lee, D. Kim, T. Kang, and I. Choi, "Photothermal convection lithography for rapid and direct assembly of colloidal plasmonic nanoparticles on generic substrates," *Small*, vol. 14, no. 45, p. 1803055, 2018.

[245] M. J. Crane, X. Zhou, E. J. Davis, and P. J. Pauzauskie, "Photothermal heating and cooling of nanostructures," *Chem. - Asian J.*, vol. 13, no. 18, pp. 2575–2586, 2018.

[246] E. P. Pandres, M. J. Crane, E. J. Davis, P. J. Pauzauskie, and V. C. Holmberg, "Laser-driven growth of semiconductor nanowires from colloidal nanocrystals," *ACS Nano*, vol. 15, no. 5, pp. 8653–8662, 2021.

[247] F. Borghese, P. Denti, R. Saija, M. A. Iatì, and O. M. Maragò, "Radiation torque and force on optically trapped linear nanostructures," *Physical Review Letters*, vol. 100, p. 163903, 4 2008.

[248] G. Pesce, P. H. Jones, O. M. Maragò, and G. Volpe, "Optical tweezers: theory and practice," *The European Physical Journal Plus*, vol. 135, no. 12, 2020.

[249] H. Ohshima, "Electrostatic interaction between two dissimilar spheres: An explicit analytic expression," *Journal of Colloid and Interface Science*, vol. 162, no. 2, pp. 487–495, 1994.

[250] J. E. Sader, S. L. Carnie, and D. Y. Chan, "Accurate analytic formulas for the double-layer interaction between spheres," *Journal of Colloid and Interface Science*, vol. 171, no. 1, pp. 46–54, 1995.

[251] B. A. Pailthorpe and W. B. Russel, "The retarded van der waals interaction between spheres," *Journal of Colloid and Interface Science*, vol. 89, no. 2, pp. 563–566, 1982.

[252] J. T. Jenkins and M. A. Koenders, "Hydrodynamic interaction of rough spheres," *Granular Matter*, vol. 7, pp. 13–18, 4 2005.

[253] S. Aragon, "A precise boundary element method for macromolecular transport properties," *Journal of Computational Chemistry*, vol. 25, pp. 1191–1205, 7 2004.

[254] S. R. Aragon and D. K. Hahn, "Preaveraged hydrodynamic interaction revisited via boundary element computations," *Journal of Chemical Theory and Computation*, vol. 2, pp. 12–17, 1 2006.

[255] D. J. Jeffrey and Y. Onishi, "Calculation of the resistance and mobility functions for two unequal rigid spheres in low-reynolds-number flow," *Journal of Fluid Mechanics*, vol. 139, pp. 261–290, 2 1984.

[256] T. A. Nieminen, V. L. Y. Loke, A. B. Stilgoe, G. Knöner, A. M. Brańczyk, N. R. Heckenberg, and H. Rubinsztein-Dunlop, "Optical tweezers computational toolbox," *Journal of Optics A: Pure and Applied Optics*, vol. 9, pp. S196–S203, 8 2007.

[257] W. B. Russel, D. A. Saville, and W. R. Schowalter, *Colloidal Dispersions*. Cambridge Monographs on Mechanics, Cambridge: Cambridge University Press, 1989.

[258] J. N. Israelachvili, *6 - Van der Waals Forces*, pp. 107–132. San Diego: Academic Press, 2011.

[259] J. N. Israelachvili, *Chapter 13 - Van der Waals Forces between Particles and Surfaces*, pp. 253–289. San Diego: Academic Press, 2011.

[260] M. M. Burns, J.-M. Fournier, and J. A. Golovchenko, "Optical binding," *Physical Review Letters*, vol. 63, pp. 1233–1236, 9 1989.

[261] K. A. Forbes, D. S. Bradshaw, and D. L. Andrews, "Optical binding of nanoparticles," *Nanophotonics*, vol. 9, pp. 1–17, 11 2019.

[262] J. Chun and D. L. Koch, "Coagulation of monodisperse aerosol particles by isotropic turbulence," *Physics of Fluids*, vol. 17, no. 2, p. 027102, 2005.

[263] H. G. Drickamer, "Forty years of pressure tuning spectroscopy," *Annu. Rev. Mater. Sci.*, vol. 20, pp. 1–18, 1990.

[264] P. J. Pauzauskie, J. C. Crowhurst, M. A. Worsley, T. A. Laurence, A. L. D. Kilcoyne, Y. Wang, T. M. Willey, K. S. Visbeck, S. C. Fakra, W. J. Evans, J. M. Zaug, and J. H. Satcher, "Synthesis and characterization of a nanocrystalline diamond aerogel," *Proceedings of the National Academy of Sciences*, vol. 108, no. 21, pp. 8550–8553, 2011.

[265] W. A. Bassett, "The birth and development of laser heating in diamond anvil cells," *Rev. Sci. Instrum.*, vol. 72, pp. 1270–1272, 2001.

[266] W. A. Bassett and M. L. C., "Disproportionation of fe_2sio_4 to $2feo^+sio_2$ at pressures up to 250 kbar and temperatures up to 3000 c," *Phys. Earth Planet. Inter.*, vol. 6, pp. 154 – 160, 1972.

[267] M. Millot, S. Hamel, J. R. Rygg, P. M. Celliers, G. W. Collins, F. Coppari, D. E. Fratanduono, R. Jeanloz, D. C. Swift, and J. H. Eggert, "Experimental evidence for superionic water ice using shock compression," *Nat. Phys.*, vol. 14, p. 297, 2018.

[268] J. P. S. Walsh and D. E. Freedman, "High-pressure synthesis: A new frontier in the search for next-generation intermetallic compounds," *Acc. Chem. Res.*, vol. 51, pp. 1315–1323, 2018.

[269] M. Guerette, M. D. Ward, K. A. Lokshin, A. T. Wong, H. Zhang, S. Stefanoski, O. Kurakevych, Y. Le Godec, S. J. Juhl, N. Alem, Y. Fei, and T. A. Strobel, "Synthesis and properties of single-crystalline na¡sub¿4¡/sub¿si¡sub¿24¡/sub¿," *Crystal Growth & Design*, vol. 18, no. 12, pp. 7410–7418, 2018.

[270] M. J. Crane, A. Petrone, R. A. Beck, M. B. Lim, X. Zhou, X. Li, R. M. Stroud, and P. J. Pauzauskie, "High-pressure, high-temperature molecular doping of nanodiamond," *Sci. Adv*, vol. 5, 2019.

[271] N. W. Ashcroft, "Hydrogen dominant metallic alloys: High temperature superconductors?," *Phys. Rev. Lett.*, vol. 92, p. 187002, 2004.

[272] A. P. Drozdov, P. P. Kong, V. S. Minkov, S. P. Besedin, M. A. Kuzovnikov, S. Mozaffari, L. Balicas, F. F. Balakirev, D. E. Graf, V. B. Prakapenka, E. Greenberg, D. A. Knyazev, M. Tkacz, and M. I. Eremets, "Superconductivity at 250 k in lanthanum hydride under high pressures," *Nature*, vol. 569, no. 7757, pp. 528–531, 2019.

[273] E. Snider, N. Dasenbrock-Gammon, R. McBride, M. Debessai, H. Vindana, K. Vencatasamy, K. V. Lawler, A. Salamat, and R. P. Dias, "Room-temperature superconductivity in a carbonaceous sulfur hydride," *Nature*, vol. 586, no. 7829, pp. 373–377, 2020.

[274] M. Somayazulu, M. Ahart, A. K. Mishra, Z. M. Geballe, M. Baldini, Y. Meng, V. V. Struzhkin, and R. J. Hemley, "Evidence for superconductivity above 260 k in lanthanum superhydride at megabar pressures," *Physical Review Letters*, vol. 122, no. 2, p. 027001, 2019. PRL.

[275] S. D. Melgaard, D. V. Seletskiy, A. Di Lieto, M. Tonelli, and M. Sheik-Bahae, "Optical refrigeration to 119 k, below national institute of standards and technology cryogenic temperature," *Optics Letters*, vol. 38, no. 9, pp. 1588–1590, 2013.

[276] A. Einstein, "On the electrodynamics of moving bodies," *Annalen der Physik*, vol. 322, pp. 891–921, 1905.

[277] L. Shenxin, C. Yuanbin, Z. Xuyi, and W. Lizhong, "High pressure luminescence and pressure induced phase transition for liyf4:eu," *Journal of Alloys and Compounds*, vol. 255, no. 1, pp. 1–4, 1997.

[278] A. Grzechnik, K. Syassen, I. Loa, M. Hanfland, and J. Y. Gesland, "Scheelite to fergusonite phase transition in ylif4 at high pressures," *Physical Review B*, vol. 65, no. 10, 2002.

[279] M. Chai and J. Michael Brown, "Effects of static non-hydrostatic stress on the r lines of ruby single crystals," *Geophysical Research Letters*, vol. 23, no. 24, pp. 3539–3542, 1996.

[280] S. A. Miller, H. E. Rast, and H. H. Caspers, "Lattice vibrations of liyf4," *The Journal of Chemical Physics*, vol. 52, no. 8, pp. 4172–4175, 1970.

[281] S. Salaün, M. T. Fornoni, A. Bulou, M. Rousseau, P. Simon, and J. Y. Gesland, "Lattice dynamics of fluoride scheelites: I. raman and infrared study of liyf4 and lilnf4 (ln = ho, er, tm, and yb)," *Journal of Physics: Condensed Matter*, vol. 9, no. 32, pp. 6941–6956, 1997.

[282] S. Salaün, A. Bulou, M. Rousseau, B. Hennion, and J. Y. Gesland, "Lattice dynamics of fluoride scheelites: Ii. inelastic neutron scattering in liyf4 and modelization," *Journal of Physics: Condensed Matter*, vol. 9, no. 32, p. 6957, 1997.

[283] A. Sen, S. L. Chaplot, and R. Mittal, "Rigid ion model of lattice dynamics in the laser host fluoroscheelites liyf4 and liybf4," *Physical Review B*, vol. 64, no. 2, 2001.

[284] A. Sen, S. L. Chaplot, and R. Mittal, "Molecular dynamics simulation of pressure-induced phase transitions in liyf4 and liybf4," *Physical Review B*, vol. 68, no. 13, 2003.

[285] A. Sen, S. L. Chaplot, and R. Mittal, "Lattice vibrations in high-pressure phases of liyf4," *Physica B: Condensed Matter*, vol. 363, no. 1, pp. 213–224, 2005.

[286] A. Sen, S. L. Chaplot, and R. Mittal, "Effects of pressure and temperature on the vibronic as well as the thermodynamic properties of liyf4 and liybf4," *Journal of Physics: Condensed Matter*, vol. 14, no. 5, pp. 975–986, 2002.

[287] D. Errandonea, F. J. Manjón, M. Somayazulu, and D. Häusermann, "Effects of pressure on the local atomic structure of cawo4 and ylif4: mechanism of the scheelite-to-wolframite and scheelite-to-fergusonite transitions," *Journal of Solid State Chemistry*, vol. 177, no. 4, pp. 1087–1097, 2004.

[288] A. Bensalah, Y. Guyot, A. Brenier, H. Sato, T. Fukuda, and G. Boulon, "Spectroscopic properties of yb3+: Lulif4 crystal grown by the czochralski method for laser applications and evaluation of quenching processes: a comparison with yb3+: Ylif4," *Journal of Alloys and Compounds*, vol. 380, no. 1, pp. 15–26, 2004.

[289] A. Sugiyama, M. Katsurayama, Y. Anzai, and T. Tsuboi, "Spectroscopic properties of yb doped ylf grown by a vertical bridgman method," *Journal of Alloys and Compounds*, vol. 408-412, pp. 780–783, 2006.

[290] B. G. Wybourne, *Spectroscopic Properties of Rare Earths*. New York: John Wiley, 1965.

[291] O. L. Malta, "The theory of vibronic transitions in rare earth compounds," *Journal of Physics and Chemistry of Solids*, vol. 56, no. 8, pp. 1053–1062, 1995.

[292] C. R. Kagan, L. C. Bassett, C. B. Murray, and S. M. Thompson, "Colloidal quantum dots as platforms for quantum information science," *Chemical Reviews*, vol. 121, no. 5, pp. 3186–3233, 2021. doi: 10.1021/acs.chemrev.0c00831.

[293] Y. Arakawa and M. J. Holmes, "Progress in quantum-dot single photon sources for quantum information technologies: A broad spectrum overview," *Applied Physics Reviews*, vol. 7, no. 2, p. 021309, 2020. doi: 10.1063/5.0010193.

[294] Y. Yamamoto, C. Santori, G. Solomon, J. Vuckovic, D. Fattal, E. Waks, and E. Diamanti, "Single photons for quantum information systems," *Progress in Informatics*, no. 1, pp. 5–37, 2005.

[295] M. Wang, T. U. Dissanayake, C. Park, K. Gaskell, and T. J. Woehl, "Nanoscale Mapping of Nonuniform Heterogeneous Nucleation Kinetics Mediated by Surface Chemistry," *Journal of the American Chemical Society*, vol. 141, pp. 13516–13524, 8 2019.

[296] G.-C. Shan, Z.-Q. Yin, C. H. Shek, and W. Huang, "Single photon sources with single semiconductor quantum dots," *Frontiers of Physics*, vol. 9, no. 2, pp. 170–193, 2014.

[297] J. Vuckovic, D. Fattal, C. Santori, and G. S. Solomon, "Enhanced single-photon emission from a quantum dot in a micropost microcavity," *Applied Physics Letters*, vol. 82, no. 21, pp. 3596–3598, 2003. 680tb Times Cited:121 Cited References Count:17.

[298] M. Pelton, C. Santori, J. Vuckovic, B. Zhang, G. S. Solomon, J. Plant, and Y. Yamamoto, "Efficient source of single photons: A single quantum dot in a micropost microcavity," *Physical Review Letters*, vol. 89, no. 23, p. 233602, 2002. PRL.

[299] E. Moreau, I. Robert, J. M. Gerard, I. Abram, L. Manin, and V. Thierry-Mieg, "Single-mode solid-state single photon source based on isolated quantum dots in pillar microcavities," *Applied Physics Letters*, vol. 79, no. 18, pp. 2865–2867, 2001. 484zm Times Cited:459 Cited References Count:11.

[300] M. Moczała-Dusanowska, L. Dusanowski, S. Gerhardt, Y. M. He, M. Reindl, A. Rastelli, R. Trotta, N. Gregersen, S. Höfling, and C. Schneider, "Strain-tunable single-photon source based on a quantum dot–micropillar system," *ACS Photonics*, vol. 6, no. 8, pp. 2025–2031, 2019. doi: 10.1021/acsphotonics.9b00481.

[301] T. Thomay, T. Hanke, M. Tomas, F. Sotier, K. Beha, V. Knittel, M. Kahl, K. M. Whitaker, D. R. Gamelin, A. Leitenstorfer, and R. Bratschitsch, "Colloidal zno quantum dots in ultraviolet pillar microcavities," *Optics Express*, vol. 16, no. 13, pp. 9791–9794, 2008.

[302] J. Baronnier, J. Houel, C. Dujardin, F. Kulzer, and B. Mahler, "Doping mapbbr3 hybrid perovskites with cdse/cdzns quantum dots: from emissive thin films to hybrid single-photon sources," *Nanoscale*, vol. 14, no. 15, pp. 5769–5781, 2022.

[303] M. Kahl, T. Thomay, V. Kohnle, K. Beha, J. Merlein, M. Hagner, A. Halm, J. Ziegler, T. Nann, Y. Fedutik, U. Woggon, M. Artemyev, F. Pérez-Willard, A. Leitenstorfer, and R. Bratschitsch, "Colloidal quantum dots in all-dielectric high-q pillar microcavities," *Nano Letters*, vol. 7, no. 9, pp. 2897–2900, 2007. doi: 10.1021/nl071812x.

[304] A. Aubret, J. Houel, A. Pereira, J. Baronnier, E. Lhuillier, B. Dubertret, C. Dujardin, F. Kulzer, and A. Pillonnet, "Nondestructive encapsulation of cdse/cds quantum dots in an inorganic matrix by pulsed laser deposition," *ACS Applied Materials & Interfaces*, vol. 8, no. 34, pp. 22361–22368, 2016. doi: 10.1021/acsami.6b07367.

[305] R. B. Comes, D. E. Perea, and S. R. Spurgeon, "Heterogeneous two-phase pillars in epitaxial nife2o4-lafeo3 nanocomposites," *Advanced Materials Interfaces*, vol. 4, no. 16, p. 1700396, 2017. https://doi.org/10.1002/admi.201700396.

[306] K. Thompson, D. Lawrence, D. Larson, J. Olson, T. Kelly, and B. Gorman, "In situ site-specific specimen preparation for atom probe tomography," *Ultramicroscopy*, vol. 107, pp. 131–139, feb 2007.

[307] M. J. Frisch, G. W. Trucks, H. B. Schlegel, G. E. Scuseria, M. A. Robb, J. R. Cheeseman, G. Scalmani, V. Barone, G. A. Petersson, H. Nakatsuji, X. Li, M. Caricato, A. V. Marenich, J. Bloino, B. G. Janesko, R. Gomperts, B. Mennucci, H. P. Hratchian, J. V. Ortiz, A. F. Izmaylov, J. L. Sonnenberg, D. Williams-Young, F. Ding, F. Lipparini, F. Egidi, J. Goings, B. Peng, A. Petrone, T. Henderson, D. Ranasinghe, V. G. Zakrzewski, N. R. J. Gao, G. Zheng, W. Liang, M. Hada, M. Ehara, K. Toyota, R. Fukuda, J. Hasegawa, M. Ishida, T. Nakajima, Y. Honda, O. Kitao, H. Nakai, T. Vreven, K. Throssell, J. J. A. Montgomery, J. E. Peralta, F. Ogliaro, M. J. Bearpark, J. J. Heyd, E. N. Brothers, K. N. Kudin, V. N. Staroverov, T. A. Keith, R. Kobayashi, J. Normand, K. Raghavachari, A. P. Rendell, J. C. Burant, S. S. Iyengar, J. Tomasi, M. Cossi, J. M. Millam, M. Klene, C. Adamo, R. Cammi, J. W. Ochterski, R. L. Martin, K. Morokuma, O. Farkas, J. B. Foresman, and D. J. Fox, "Gaussian 16 Revision B.01." Gaussian Inc. Wallingford CT 2016.

[308] C. Adamo and V. Barone, "Toward reliable density functional methods without adjustable parameters: The pbe0 model," *J. Chem. Phys.*, vol. 110, pp. 6158–6169, 1999.

[309] M. Ernzerhof and G. E. Scuseria, "Assessment of the perdew–burke–ernzerhof exchange-correlation functional," *J. Chem. Phys.*, vol. 110, pp. 5029–5036, 1999.

[310] W. R. Wadt and P. J. Hay, "*Ab initio* effective core potentials for molecular calculations - potentials for main group elements na to bi," *J. Chem. Phys.*, vol. 82, pp. 284–298, 1985.

[311] P. J. Hay and W. R. Wadt, "*Ab initio* effective core potentials for molecular calculations. potentials for the transition metal atoms sc to hg," *J. Chem. Phys.*, vol. 85, pp. 270–283, 1985.

[312] H. D. Nelson, S. O. M. Hinterding, R. Fainblat, S. E. Creutz, X. Li, and D. R. Gamelin, "Mid-gap states and normal vs inverted bonding in luminescent cu^{+}- and ag^{+}-doped cdse nanocrystals," *J. Am. Chem. Soc.*, vol. 139, no. 18, pp. 6411–6421, 2017.

[313] H. D. Nelson, X. Li, and D. R. Gamelin, "Computational studies of the electronic structures of copper-doped cdse nanocrystals: Oxidation states, jahn–teller distortions, vibronic bandshapes, and singlet–triplet splittings," *J. Phys. Chem. C*, vol. 120, no. 10, pp. 5714–5723, 2016.

[314] M. E. Casida, *Recent Advances in Density Functional Methods:(Part I)*, vol. 1. Singapore: World Scientific Publishing, 1995.

[315] A. Dreuw and M. Head-Gordon, "Single-reference *Ab initio* methods for the calculation of excited sates of large molecules," *Chem. Rev.*, vol. 105, pp. 4009–4037, 2005.

[316] R. E. Stratmann, G. E. Scuseria, and M. J. Frisch, "An efficient implementation of time-dependent density-functional theory for the calculation of excitation energies of large molecules," *J. Chem. Phys.*, vol. 109, pp. 8218–8224, 1998.

[317] S. Fähler, S. Kahl, M. Weisheit, K. Sturm, and H. Krebs, "The interface of laser deposited Cu/Ag multilayers: evidence of the 'subsurface growth mode' during pulsed laser deposition," *Applied Surface Science*, vol. 154-155, pp. 419–423, feb 2000.

[318] S. K. Hau, K. H. Wong, P. W. Chan, and C. L. Choy, "Intrinsic resputtering in pulsed-laser deposition of lead-zirconate-titanate thin films," *Applied Physics Letters*, vol. 66, pp. 245–247, jan 1995.

[319] K. Sturm and H.-U. Krebs, "Quantification of resputtering during pulsed laser deposition," *Journal of Applied Physics*, vol. 90, pp. 1061–1063, jul 2001.

[320] W. Lukosz and R. E. Kunz, "Light emission by magnetic and electric dipoles close to a plane interface. i. total radiated power," *Journal of the Optical Society of America*, vol. 67, no. 12, pp. 1607–1615, 1977.

[321] W. Lukosz and R. E. Kunz, "Light emission by magnetic and electric dipoles close to a plane dielectric interface. ii. radiation patterns of perpendicular oriented dipoles," *Journal of the Optical Society of America*, vol. 67, no. 12, pp. 1615–1619, 1977.

[322] W. Lukosz, "Light emission by magnetic and electric dipoles close to a plane dielectric interface. iii. radiation patterns of dipoles with arbitrary orientation," *Journal of the Optical Society of America*, vol. 69, no. 11, pp. 1495–1503, 1979.

[323] K. Gong, Y. Zeng, and D. F. Kelley, "Extinction coefficients, oscillator strengths, and radiative lifetimes of cdse, cdte, and cdte/cdse nanocrystals," *J. Phys. Chem. C*, vol. 117, no. 39, pp. 20268–20279, 2013.

[324] R. Send and F. Furche, "First-order nonadiabatic couplings from time-dependent hybrid density functional response theory: Consistent formalism, implementation, and performance," *J. Chem. Phys.*, vol. 132, no. 4, p. 044107, 2010.

[325] D. B. Lingerfelt, D. B. Williams-Young, A. Petrone, and X. Li, "Direct ab initio (meta-)surface-hopping dynamics," *J. Chem. Theory Comput.*, vol. 12, no. 3, pp. 935–945, 2016. PMID: 26855086.

[326] G. Fisicaro, M. Sicher, M. Amsler, S. Saha, L. Genovese, and S. Goedecker, "Surface reconstruction of fluorites in vacuum and aqueous environment," *Physical Review Materials*, vol. 1, p. 033609, 8 2017.

[327] U. Delić, M. Reisenbauer, K. Dare, D. Grass, V. Vuletić, N. Kiesel, and M. Aspelmeyer, "Cooling of a levitated nanoparticle to the motional quantum ground state," *Science*, vol. 367, no. 6480, pp. 892–895, 2020.

[328] A. Ashkin, J. M. Dziedzic, J. Bjorkholm, and S. Chu, "Observation of a single-beam gradient force optical trap for dielectric particles," *Opt. Lett.*, vol. 11, no. 5, pp. 288–290, 1986.

[329] R. M. Pettit, L. P. Neukirch, Y. Zhang, and A. N. Vamivakas, "Coherent control of a single nitrogen-vacancy center spin in optically levitated nanodiamond," *J. Opt. Soc. Am. B*, vol. 34, no. 6, pp. C31–C35, 2017.

[330] L. Rondin, J.-P. Tetienne, T. Hingant, J.-F. Roch, P. Maletinsky, and V. Jacques, "Magnetometry with nitrogen-vacancy defects in diamond," *Rep. Prog. Phys.*, vol. 77, no. 5, p. 056503, 2014.

[331] C. Johnson, J. Exell, Y. Lin, J. Aguilar, and K. D. Welsher, "Capturing the start point of the virus–cell interaction with high-speed 3d single-virus tracking," *Nature Methods*, vol. 19, no. 12, pp. 1642–1652, 2022.

[332] B. Journaux, I. Daniel, S. Petitgirard, H. Cardon, J.-P. Perrillat, R. Caracas, and M. Mezouar, "Salt partitioning between water and high-pressure ices. implication for the dynamics and habitability of icy moons and water-rich planetary bodies," *Earth and Planetary Science Letters*, vol. 463, pp. 36–47, 2017.

[333] B. Journaux, I. Daniel, R. Caracas, G. Montagnac, and H. Cardon, "Influence of nacl on ice vi and ice vii melting curves up to 6gpa, implications for large icy moons," *Icarus*, vol. 226, no. 1, pp. 355–363, 2013.

Appendix A

PUBLICATIONS

R. G. Felsted, A. Pant, A. B. Bard, X. Xia, D. R. Luntz-Martin, S. Dadras, S. Zhang, A. N. Vamivakas, P. J. Pauzauskie. "Chemically Tunable Aspect Ratio Control and Laser Refrigeration of Hexagonal Sodium Yttrium Fluoride Upconverting Materials." *Crystal Growth and Design* **2022**, *22* (6), 3605-3612.

R. G. Felsted*, A. B. Bard*, A. S. Ganas, A. Pant, C. Gupta, Y. Chen, E. Nakouzi, B. Jin, N. M. Washton, M. D. LaCount, C. J. Mundy, G. K. Schenter, J. Chun, S. R. Spurgeon, G. K. Lee, V. C. Holmberg, L. N. Brush, J. J. De Yoreo, P. J. Pauzauskie. "Multi-Step Crystallization and Chemical Evolution of Sodium Yttrium Fluoride." (In Preparation, 2023).

R. G. Felsted*, A. Pant*, A. B. Bard, X. Xia, S. Dadras, K. Shayan, D. R. Luntz-Martin, D. Mannikko, I. M. Pavlovetc, S. Stoll, M. Kuno, A. N. Vamivakas, P. J. Pauzauskie. "Solid-state laser refrigeration of nanodiamond quantum sensors." (In Preparation, 2023).

A. Pant, C. Gupta, K. Senkalla, **R. G. Felsted**, X. Xia, T. Spohn, S. T. Dunham, F. Jelezko, P. J. Pauzauskie. "Reduced photothermal heating in diamonds enriched with H3 point defects." *Journal of Applied Physics* **2022**, *131* (234401).

R. G. Felsted, J. Chun, G. K. Schenter, A. B. Bard, X. Xia, P. J. Pauzauskie. "The Role of Dynamics & Surface Roughness on Self-Assembly of Colloids by use of

Optical Tweezers." (In Preparation, 2023).

D. R. Luntz-Martin, **R. G. Felsted**, S. Dadras, P. J. Pauzauskie, A. N. Vamivakas. "Laser refrigeration of optically levitated sodium yttrium fluoride nanocrystals." *Optics Letters* **2021** *46* (15): 3797-3800.

R. G. Felsted*, G. Winstone*, Z. Wang*, S. Klomp*, A. Laeuger, C. Gupta, D. Grass, N. Aggarwal, J. Sprague, P. J. Pauzauskie, S. L. Larson, V. Kalogera, A. A. Geraci. "Optical Trapping of High-Aspect-Ratio NaYF Hexagonal Prisms for kHz-MHz Gravitational Wave Detectors." *Physical Review Letters* **2022**, *129* (053604).

A. S. Ganas, E. A. Dobretsova, A. Pant, B. Journaux, X. Xia, **R. G. Felsted**, P. J. Pauzauskie. "Solid-state laser refrigeration at GPa pressures." (In Preparation, 2023).

R. G. Felsted, A. Pant, A. B. Bard, C. Erickson, B. Bishop, L. Liu, R. Beck, D. Perea, S. R. Spurgeon, V. C. Holmberg, X. Li, D. R. Gamelin, P. J. Pauzauskie. "Colloidal Semiconductor Quantum Dots in Dichalcogenide Cavities Prepared through Pulsed Laser Deposition." (In Preparation, 2023).

M. B. Lim, **R. G. Felsted**, X. Zhou, B. E. Smith, P. J. Pauzauskie. "Patterning of Graphene Oxide with Optoelectronic Tweezers." *Appl. Phys. Lett.* **2018** *113*: 031106.

** indicates equal contribution*